Transparent Substrates for Plasmonic Sensing by Lithography-Free Fabrication

Thilsted, Anil Haraksingh

Publication date:
2016

Document Version
Publisher's PDF, also known as Version of record

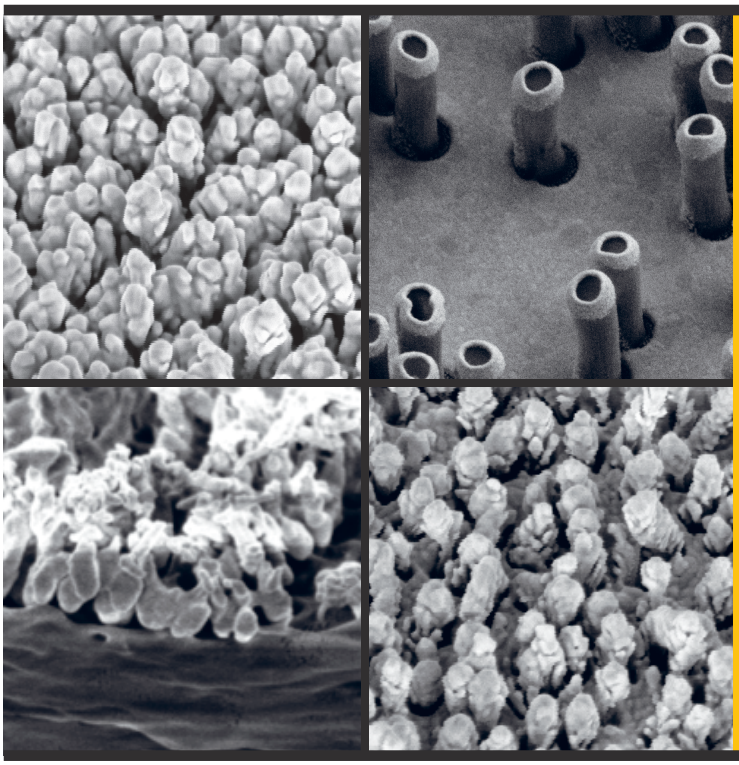

Transparent Substrates for Plasmonic Sensing by Lithography-Free Fabrication

Anil Haraksingh Thilsted
PhD Thesis November 2016

DTU Nanotech
Department of Micro- and Nanotechnology

DTU Technical University of Denmark

Transparent Substrates for Plasmonic Sensing by Lithography-Free Fabrication

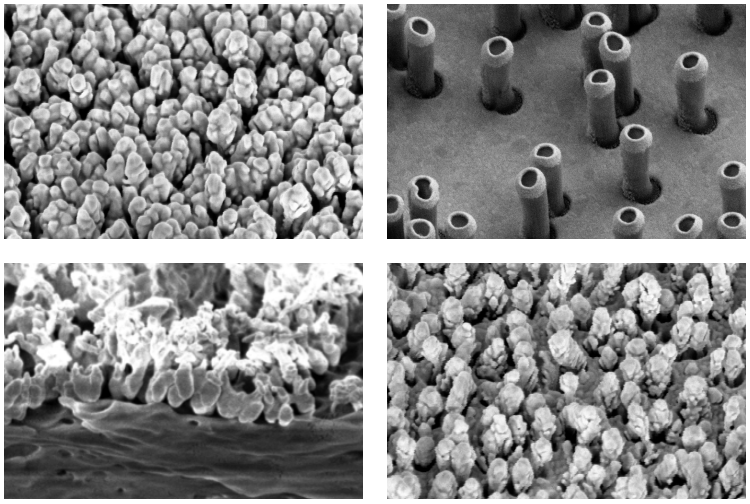

Ph.D. Thesis

Anil Haraksingh Thilsted

November 2016

DTU Nanotech
Department of Micro- and Nanotechnology

Cover image

The four plasmonic substrates achieved in this Ph.D. research project: (top left) gold-capped glass nanopillars; (top right) glass nanocylinders with gold rings; (bottom left) transferred gold nanocaps to polymer; (bottom right) gold-capped polymer injected nanopillars.

Transparent Substrates for Plasmonic Sensing by Lithography-Free Fabrication

by

Anil Haraksingh Thilsted

A Thesis
Submitted in Partial Fulfillment
of the Requirements for the Degree of

Doctor of Philosophy

Department of Micro- and Nanotechnology
Technical University of Denmark
Denmark

November 2016

Title of the Ph.D. Thesis
Transparent Substrates for Plasmonic Sensing by Lithography-Free Fabrication

Name of Author
Anil Haraksingh Thilsted

Research project duration
August 2013 - November 2016

Supervisors

Principal Supervisor
Professor Anja Boisen
Department of Micro- and Nanotechnology
Technical University of Denmark

Co-supervisor
Dr. Tomas Rindzevicius
Department of Micro- and Nanotechnology
Technical University of Denmark

Co-supervisor
Dr. Michael Stenbæk Schmidt
Department of Micro- and Nanotechnology
Technical University of Denmark

Preface

This Ph.D. research projecty was initiated in August 2013 at the Nanoprobes research group, the Department of Micro- and Nanotechnology, Technical University of Denmark.

The nanofabrication techniques developed were carried out at the facilities of DTU Danchip, Technical University of Denmark and made use of the available tools and expertise of the staff to pursue non-traditional cleanroom production and push the envelope for what was possible.

Within this research project, supervision of two B.Sc. and one M.Sc. thesis projects was undertaken. The students' thesis work constituted a large portion of the optimization required to achieve the different sensing platforms.

An application was filed for a patent on the design of both transparent nanopillars as well as nanocylinders for plasmonic sensing.

During the course of this research project, Ph.D. summer courses were attended, including the 'School of Entrepreneurship in Europe and China', at Fudan University, Shanghai, China and 'European School of Nanosciences and Nanotechnology' in Grenoble, France. Research results were given as oral presentations at the International Conference on Surface Plasmon Photonics in Jerusalem, Israel, in 2015 and the International Conference on Raman Spectroscopy in Fortaleza, Brazil, in 2016.

The knowledge attained during the development of the plasmonic platforms was transferred to researchers at the Nanoprobes research group for use in future applications, including food safety, cell studies and drug delivery.

The PhD. research project was partially funded by the NAPLAS project, The Danish Council for Independent Research as well as the European Research Council under the European Union's Seventh Framework Programme (FP7/2007-2013) / ERC grant agreement nº 320535.

Acknowledgements

I wish to thank my supervisors, Professor Anja Boisen, Dr. Tomas Rindzevicius and Dr. Michael Stenbæk Schmidt for the proposal and funding of this Ph.D. research project. I deeply appreciate their effort, time, ideas and feedback which has helped me overcome obstacles, see opportunities and follow through on my research.

Specifically, I express my gratitude to Professor Anja Boisen for always providing an overview and perspective of my research progress and her optimistic view of the opportunities and challenges ahead. Her leadership style and her focus in bringing people of different skills and work styles together to achieve a common goal has had a profound positive effect on me. It has laid the foundation for how I plan to carry out future projects, commercial or academic.

I thank Dr. Tomas Rindzevicius for sharing his deep technical knowledge of plasmonic systems and for his guidance in the different project areas. His ability to be critical on which direction to take has helped focused the project and produced results that were useful for other researchers. He has pushed me to increase the level of understanding, presentation of scientific results and development of a cohesive narrative.

I also thank Dr. Michael Stenbæk Schmidt for sharing with me his extensive technical knowledge of plasma etching, which was the major challenge in this research project. He provided sound advice on experimental measurements and often gave the solution to a challenge or showed me an oppurtunity which I had not seen.

It has been a great experience and fantastic oppurtunity to work in the Nanoprobes group, which has been a source of friendship and support, as well as provided extensive advice and collaboration opportunities. All members of the group offered their knowledge and help. This research project would not have been possible without the work effort and expertise from my fellow researchers. I especially thank Dr. Kaiyu Wu for his calculations and interpretation of plasmonic modes as well as sharing his knowledge on Raman measurements and presentation of scientific results. His work and knowledge were critical for this research project.

I also thank Onur Durucan and Kuldeep Sanger for their ideas and collaboration on electrochemistry and SERS. I thank Marco Matteucci, Darmin Caţak and Marlitt Viehrig for their crucial work and knowledge to achieve polymer injected nanopillars and Kinga Zór for her surface chemistry knowledge and experimental work. I thank Dr. Tommy Sonne Alstrøm, Dr. Anna Line Brøgger, Dr. Peter Emil Larsen, Dr. Kasper Bayer Frøhling, Dr. Michael Bache, Sune Zoëga Andreasen and Maksymilian Kurek for scientific discussions and camaraderie.

I thank Julia Cathrine Dyrnum for her B.Sc. thesis work on glass nanopillars

and Giuseppe Saccone for his M.Sc. thesis work on transferred metal nanocaps. I also thank Jesper Yue Pan for his B.Sc. thesis work on fused silica nanocylinders as well as his work as a research assistant.

I would like to express my appreciation to family and my friends for their kindness and support. I especially thank my mother, Shakuntala Haraksingh Thilsted, for her support and proofreading of all my work. Lastly, I thank my girlfriend Mette Slipsager for her love, support and encouragement in all of my endeavours.

Anil Haraksingh Thilsted
November 2016

Abstract

This Ph.D. thesis presents fabrication and optimization of transparent plasmonic substrates that can be used for biological and chemical sensing by surface enhanced Raman spectroscopy (SERS) sensing and localized surface plasmon resonance refractive index (LSPR RI) sensing. These substrates are: glass nanopillars with gold caps for SERS sensing; polymer nanopillars with gold caps for SERS sensing; transferred gold nanocaps to polymer foil for SERS sensing; and glass hollow-core nanocylinders with gold nanorings for LSPR RI sensing.

These substrates were achieved using lithography-free fabrication methods, and resulted in large-area, high throughput and low cost production techniques. The fabrication techniques consisted of using aluminum patterned areas and reactive ion etching (RIE) to achieve nanopillars or nanocylinders in glass; using RIE to achieve nanopillars in silicon as a mould for polymer injection; and using RIE and imprinting to transfer gold nanocaps to a polymer foil.

The SERS substrates showed a 91%, a 94% and 8% Raman signal intensity compared to gold-capped silicon nanopillars for the glass nanopillars, the polymer injected nanopillars and the transferred gold nanocaps, respectively. As the substrates were transparent, measurements from the backside were possible, showing a 44%, 1.7% and 71% Raman signal intensity in comparison to the measurements from the front, for the glass nanopillars, the polymer injected nanopillars and the transferred metal nanocaps, respectively.

For LSPR, the glass hollow-core nanocylinders with suspended gold nanorings showed a sensitivity of 658 nm RIU^{-1} with a figure-of-merit of 10. The LSPR wavelengths could be shifted by tuning the plasma etching parameters.

Due to the low electrical conductivity of glass substrates, electrodes could be incorporated onto the glass nanopillars, resulting in a device that could be used for both electrochemistry and SERS measurements. The polymer injected nanopillars used an industrial high throughput and robust fabrication technique. The substrate was integrated into high throughput fluidic devices for *in-situ* SERS measurements.

The fabrication methods presented in this Ph.D. thesis are scalable, high throughput and low cost, and result in high performance plasmonic surfaces for sensing.

Resumé

Denne Ph.D. afhandling præsenterer fabrikation og optimering af gennemsigtige plasmoniske substrater der kan bruges til biologiske og kemiske detektion ved brug af surface enhanced Raman spektroskopi (SERS) og surface plasmon resonance refraktiv indeks (LSPR RI) detektion. Disse substrater består af glas-nanosøjler med guldkroner til SERS, plastik-nanosøjler med guldkroner til SERS, guld-nanokroner overført til plastik folie til SERS og hule nanocylindre med guld nanoringe til LSPR RI detektion.

Disse substrater var produceret uden brug af litografi og resulterede i fabrikationsteknikker der gav både store arealer, stor produktionsmængde og lave omkostning. Disse teknikker omfattedebrug af mønstrede aluminiums arealer og reaktiv ion æts (RIE) til at producere nanosøjler eller nanocylindre i glas, brug af RIE for at producere nanosøjler i silicium som en form for brug af plastik indsprøjtning og brug af RIE og aftryk for at producere overførte guld kroner til polymer folie.

SERS-substraterne viste en 91%, en 94% og 8% Raman signal intensitet i forhold til guldkroner på silicium nanosøjler, for henholdsvis glas nanosøjler, plastik nanosøjler og guldkroner overført til plastik folie. Da substraterne var gennemsigtige, kunne man måle fra bagsiden. Hvor substraterne viste en 44%, 1.7% og 71% Raman signal intensitet i forhold til målinger taget fra forsiden.

Hule glas-nanocylindre med opløftet guld-nanoringe viste en følsomhed på 686 nm RIU^{-1} med en figure-of-merit på 10. LSPR bølgelængder kan forskydes ved at ændre på plasmaæts-parametrene.

På grund af den lave elektrisk konduktans af glas-substraterne, kunne elektroder inkorporeres i glas-nanosøjlerne. Dette resulterede i en overflade der kunne bruges til både elektrokemi- og SERS-målinger. De plastik-indsprøjtede nanosøjler benyttede en industriel, skalerbar, og robust fabrikationsteknik og substratet kunne integreres med mikrofluid-chips til *in-situ* SERS-målinger.

Fabrikationsmetoderne præsenterede i denne Ph.D. afhandling er skalerbare, kan producere store mængder og har lave produktionsomkostninger, hvilket resulterer i plasmoniske overflader til detektion med høj ydeevne.

Contents

List of Figures

Chapter 1

Introduction

At the metal-dielectric interface, noble metals have the capacity to support a collective, resonant oscillation of conduction electrons, known as surface plasmon resonance (SPR). Under certain experimental conditions, SPRs can be excited by external electromagnetic radiation [1]. If the metal is separated into structures at the nanoscale, the conduction electrons oscillate locally, with a resonance frequency that depends on the size, shape, composition and local environment of the nanostructures. This localized surface plasmon resonance (LSPR) results in intense absorption and scattering of light as well as enhancement of the EM field near the surface of the nanostructures. This unique light-matter interaction phenomenon has given rise to a significant research area of surface-enhanced spectroscopy as well as biological and chemical sensing and has led to a wide range of applications within clinical diagnosis[2], biomolecular engineering[3, 4], environmental monitoring[5] and food science[6].

The wavelength at which LSPR occurs, results in a high absorption and scattering of light, such that there is a extinction peak. The sensitivity of LSPR to changes in the local dielectric environment results in a shift of the LSPR peak position and thus a movement of the extinction peak. The LSPR shift can be observed when a molecule is within a few nanometers or is adsorbed onto the surface of the nanostructure. This effect allows for sensitive detection of adsorbed molecules and thus can be used for sensing of biological molecules such as proteins and antibodies. LSPR molecular detection is therefore especially suitable for immunoassays[7].

The enhanced EM field near the surface of the plasmonic nanostructures also allows for surface-enhanced Raman spectroscopy (SERS) sensing. Molecules are detected and identified, based on their unique vibrational energy levels and their corresponding optical response. These vibrational energy levels are revealed optically due to the inelastic photon-phonon scattering, in which either energy is gained

or lost, referred to as Stokes or anti-Stokes shift. Molecules that are adsorbed to the plasmonic nanostructures reside in a locally enhanced EM field and electromagnetically couple with the LSPR mode. This interaction between the molecule and the LSPR increases Raman scattering by as much as a factor of $10^6 - 10^{10}$ [8]. This dramatic increase in Raman signal due to surface plasmons mitigates the inherently weak Raman scattering effect such that the sensing method becomes viable as an ultrasensitive molecular probe. The EM field enhancement can be greatly increased if the metal nanostructures are in close proximity and therefore can couple their plasmonic modes, resulting in an EM hot-spot between the structures. For this reason, substrates for SERS sensing often feature a high density of these hot-spots in which localized metal nanostructures are in close proximity to each other. The detection of ultra-low concentrations of small molecules and especially those with relatively large Raman scattering cross-sections, make SERS sensing especially suitable for environmental monitoring. In addition to general chemical detection, functionalization of the plasmonic nanostructures introduces a specificity suitable for biomarker detection and identification via SERS [9].

Fabricating metal nanostructures has typically been carried out using chemical synthetic techniques, resulting in large quantities of metal colloids. While size, shape and composition can be partially controlled via this method, lithographic techniques allow for much greater control of periodicity and morphology of the plasmonic structures, thus leading to more finely tuned and higher performance LSPR and SERS substrates. These techniques include nanosphere, electron beam and co-block polymer lithography and can achieve a wide range of structures that support localized plasmons, including triangles, nanocavities, and structures suspended above the substrate [10]. While lithographic techniques allow control of the nanostructure morphology to a varying degree control, they are time-consuming, complicated or expensive to carry out [11]. For these reasons, top-down fabrication of plasmonic substrates are often low throughput and achieved on small areas, limiting large-scale studies for sensing applications that require repeated measurements. The low throughput also prevents scaling up to volume required for industrial applications.

In recent years, the lithography-free technique of reactive ion etching (RIE) has shown to be a useful tool in nanostructuring large areas in a single straightforward step [12]. RIE uses a plasma with volatile gases to carry out a physical and chemical etch of a substrate. Small spatial inhomogeneities in the etching rate result in initial nanostructures that are enlargened due to self-masking of sidewalls. In this way, high aspect ratio nanopillars can be achieved with a high density over large areas. A subsequent metal deposition using e-beam evaporation results in isolated metal caps

at the tips of these nanopillars. The high density results in closely packed LSPR "hot spots", resulting in a substrate that is highly suitable for SERS measurements [13]. While the process is much more stochastic than traditional top-down approaches, the etching parameters can be adjusted to allow partial tuning of the LSPR peak position. Lithography-free RIE thus allows for uniform LSPR and SERS behaviour, across large areas, using a high throughput and straightforward fabrication method.

1.1 Overall aim

This Ph.D. research project is a part of the NAPLAS - NAnoPLAsmonic Sensors project, funded by The Danish Council for Independent Research. The aim of NAPLAS is to expand the capabilities, understanding and applications of plasmonic substrates, based on nanopillar arrays achieved via lithography-free methods to develop novel and high performance sensing platforms. Additionally, the project aimed to achieve transparent plasmonic substrates using lithography-free fabrication techniques. Plasmonic transparent substrates such as glass and polymers allow for chemical resistivity, flexibility in optical measurements, integration into fluidic components, integrating electrode designs as well as utilization of novel fabrication methods with high throughput.

The overall aim of this Ph.D. research project was to achieve large area LSPR and SERS substrates in glass and polymer, using lithography-free techniques. These substrates must exhibit clear LSPR modes with high sensitivity to either refractive index changes, must be have a uniform LSPR and SERS behaviour and fabricated using high throughput methods. Furthermore, investigations must be carried out of the optical properties of the fabricated structures and the possibility of incorporating electrode or fluidic components into the same platform.

1.2 Specific objectives

The specific objectives of this Ph.D. project were to develop and optimize:

- A RIE fabrication method for glass wafers to achieve high density nanopillars as the underlying structure for metal caps for SERS sensing as well electrodes for electrochemistry measurements;

- A method for transferring metal caps from the tips of silicon nanopillars to a transparent polymer foil for obtaining a polymer-based SERS substrate;

- A polymer injection method for achieving polymer nanopillars as the underlying structure for metal caps for SERS sensing as well as fluidic integration;
- A RIE fabrication method for glass wafers to achieve hollow nanocylinders as the underlying structure for suspended plasmonic rings for LSPR refractive index sensing.

1.3 Ph.D. Thesis structure

- Introduction:
  The background and motivation for the Ph.D. project.
- LSPR Theory:
  A theoretical description of localized surface plasmons.
- Raman Theory and SERS:
  A theoretical description of Raman spectroscopy and SERS.
- Using Nanopillar arrays to achieve SERS and LSPR substrates:
  A description of how nanopillars can be used to achieve LSPR and SERS substrates
- Glass Nanopillars for SERS and Electrochemistry:
  Experimental methods to achieve nanopillars in glass for SERS as well as electrodes for concurrent electrochemistry measurements.
- Injection Moulded Nanopillar SERS substrates:
  The results and experimental methods to achieve a nickel mould from silicon nanopillars and polymer injected nanopillars for SERS measurements and fluidic integration.
- Gold nanocaps transferred to polymer foil:
  Experimental methods for transferring metal caps to polymer foils to achieve flexible and transparent SERS substrates.
- Glass Nanocylinders with suspended gold Nanorings for LSPR:
  The results and experimental methods to achive nanocylinders in glass for LSPR refractive index measurements.
- SERS substrate comparison:
  A comparison of the advantages and disadvantages of the different SERS substrates.

- Concluding Remarks and Outlook
  A summary of the achieved results and the perspectives.

- P1: Glass Nanopillars for SERS and Electrochemistry
  A manuscript for submission describing glass nanopillars for use for SERS and electrochemistry measurements.

- P2: Polymer Injected Nanopillars for SERS
  A manuscript for submission describing polymer injected nanopillars for SERS sensing and towards fluidic integration.

- P3: Flexible and Transparent SERS substrates
  A manuscript for submission describing the transfer of gold nanocaps to polymer foil for SERS detection.

- P4: LSPR Sensing with Glass Nanocylinders
  A published article describing the use of nanocylinders for achieving a tunable LSPR refrative index sensing substrate.

- Appendix: Patent
  A patent application covering the intellectual property of the plasmonic structures.

Chapter 2

Theory

A brief overview of the electromagnetic theory of localized surface plasmons, Raman scattering and surface-enhanced Raman spectroscopy is presented.

2.1 Localized Surface Plasmons

The concept of plasmon resonance in metals was first described by Gustav Mie in 1908 [14] in which Maxwell's electromagnetic theory was applied to optical absorption and scattering of nanospheres. Advancements in plasmon theory has since been carried out by Kretschmann et al.[15] and Otto et al.[16] to lay a foundation for the theoretical understanding and experimental observations of surface plasmons. The interaction of metal nanoparticles with an electromagnetic wave and how this gives rise to a resonance condition are presented below.

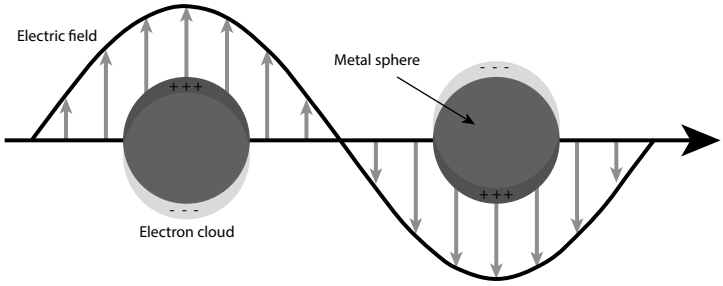

Figure 2.1: Illustration of the localized surface plasmon resonance effect. An incident oscillating electric field drives collective oscillations of free electrons near the surface of the nanospheres.

The Mie theory gives an exact solution to the optical response, however, a much simpler quasi-static approximation can be used, provided that the nanostructure is much smaller than the wavelength of the incident electromagnetic field. In this

case, the oscillating electromagnetic field is near constant over the volume of the nanosphere and, therefore, an electrostatic field can be assumed. This is described using the Laplace equation.

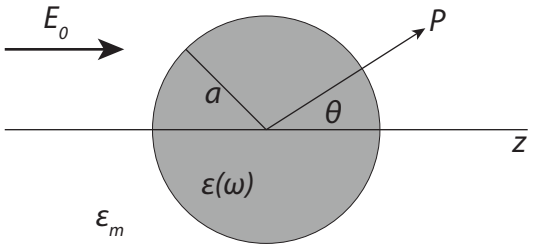

Figure 2.2: Illustration of the model used for the Mie quasi-static approximation: a homogeneous sphere placed in an electrostatic system. The variables are: the incoming electric field E_0, the dielectric function $\epsilon(\omega)$ of the nanosphere, the constant dielectric value ϵ_m of the medium, the radius of the sphere a, and θ, the angle between the position vector r at point P and the z axis.

The Laplace equation, describing the potential ϕ is written as $\nabla^2\phi = 0$ and can be used to calculate the electric field from $\mathbf{E} = -\nabla\phi$. Due to azimuthal symmetry of the model illustrated in Figure 2.2, the general solution for ϕ is of the form:

$$\phi(r,\theta) = \sum_{l=0}^{\infty}[A_l r^l + B_l r^{-(l+1)}]P_l(\cos\theta)$$

in which $P_l(\cos\theta)$ are Legendre polynomials on the order of l, and θ is the angle between the position vector $\mathbf{r}$ at point P and the z axis (see Figure 2.2). The potential can be split into outside ϕ_{in} and inside ϕ_{out} the sphere. The requirement for ϕ_{out} that $-E_0 z = -E_0 r\cos\theta$ finds the first Legendre polynomial values: $B_1 = E_0$ and $B_l = 0$ for $l \neq 1$. Additionally, boundary conditions for the potential include equality of the tangential and normal components of the electric field across the surface of the sphere:

$$\begin{aligned} -\frac{1}{a}\frac{\partial\phi_{in}}{\partial\theta}\bigg|_{r=a} &= -\frac{1}{a}\frac{\partial\phi_{out}}{\partial\theta}\bigg|_{r=a} \\ -\epsilon_0\epsilon\frac{\partial\phi_{in}}{\partial\theta}\bigg|_{r=a} &= -\epsilon_0\epsilon_m\frac{\partial\phi_{out}}{\partial\theta}\bigg|_{r=a} \end{aligned}$$

These boundary conditions, when inserted in the Legendre polynomial determine the remaining coefficients: $A_l = C_l = 0$ for $l \neq 1$ and thus the solution for ϕ_{in} and

ϕ_{out} is:

$$\begin{aligned}\phi_{in} &= -\frac{3\epsilon_m}{\epsilon + 2\epsilon_m} E_0 r\cos\theta \\ \phi_{out} &= \underbrace{-E_0 r\cos\theta}_{\text{applied field}} + \underbrace{\frac{\epsilon - \epsilon_m}{\epsilon + 2\epsilon_m} E_0 a^3 \frac{\cos\theta}{r^2}}_{\text{dipole field}}\end{aligned} \tag{2.1}$$

The description of the electric field potential outside the sphere consists of the superposition of the external applied field and the dipole field from the sphere. The electric field of the dipole is maximised at the condition in which $|\epsilon + 2\epsilon_m|$ is at its minimum. For small or slowly-varying $\mathrm{Im}[\epsilon]$, the real relative permittivity of the sphere $\epsilon(\omega)$ must thus fulfil the following condition to maximise the dipole field:

$$\mathrm{Re}[\epsilon(\omega)] = -2\epsilon_m$$

This relationship is known as the Fröhlich condition, for which the sphere experiences an electromagnetic resonance. This condition depends on both on the permittivity of the sphere as well as the surrounding medium. For a sphere consisting of a Drude metal situated in air, the dielectric function (in the case of larger frequencies with negligible electron damping) is expressed as:

$$\epsilon(\omega) = 1 - \frac{\omega_p^2}{\omega_0^2}$$

in which ω_0 is the frequency of the incident electromagnetic field and ω_p is the plasma frequency. The plasma frequency is derived from a model in which the electrons of a metal move freely against a background of positive ion cores, driven by an incident EM field. The frequency at which the plasma oscillation experiences resonance and thereby becomes a plasmon is called the plasma frequency. This is expressed as [1]:

$$\omega_p = \sqrt{\frac{ne^2}{\epsilon_0 m_e}}$$

in which n is the electron density, e is the elementary charge, m_e is the effective electron mass and ϵ_0 is the electric permittivity of vacuum. As the dielectric function of metals is wavelength dependent, the resonance condition occurs only for specific

wavelengths of incoming light. Additionally, changes in the dielectric value of the surrounding medium likewise also shifts the wavelength at which this condition is met.

The corresponding optical cross-section for scattering C_{sca} and absorption C_{abs} for a sphere are expressed [17]:

$$C_{\text{sca}} = \frac{8\pi}{3} k^4 a^6 \left| \frac{\epsilon(\omega) - \epsilon_m}{\epsilon(\omega) + 2\epsilon_m} \right|^2$$
$$C_{\text{abs}} = 4\pi k a^3 \text{Im} \left[\frac{\epsilon(\omega) - \epsilon_m}{\epsilon(\omega) + 2\epsilon_m} \right]$$

The extinction is given as the linear combination of these two values. The absorption and scattering of light are thus maximised at the Fröhlich condition. An extinction spectrum can therefore show the LSPR wavelength position and shifts thereof. This is the basis for refractive index sensing, using localized surface plasmon resonance.

2.2 Raman scattering

Raman scattering is the inelastic scattering of a photon upon interaction with matter. This type of light-matter interaction was first discovered in liquids by C. V. Raman and K. S. Krishnan in 1928 [18]. Raman scattering can be described using both the classical wave or quantum particle interpretation. The classical wave interpretation is described here, in which light is considered as electromagnetic radiation that contains an oscillating electric field that interacts with a molecule through its polarizability. A diatomic molecule is modeled as two masses on a spring, as illustrated in Figure 2.3.

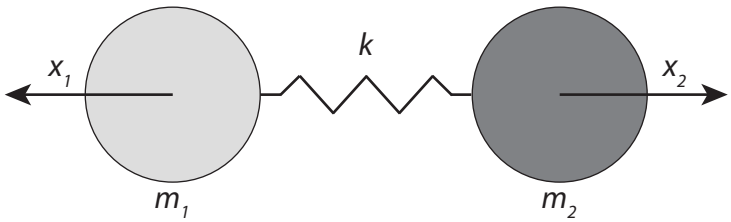

Figure 2.3: Illustration of a model diatomic molecule with two masses, connected on a spring.

Using this model, m_1 and m_2 are the two masses, x_1 and x_2 are their two displacements and k is the spring constant. Using these values, the displacement of the molecule, using Hooke's law is expressed as:

$$\frac{m_1 m_2}{m_1 + m_2}\left(\frac{d^2 x_1}{dt^2} + \frac{d^2 x_2}{dt^2}\right) = -k(x_1 + x_1)$$

Replacing the total displacement $x_1 + x_2$ with q, and the reduced mass to μ, the above equation is reduced to:

$$\mu \frac{d^2 q}{dt^2} = -kq$$

Solving for the total displacement q yields:

$$q = q_0 \cos(2\pi\nu_m t) \tag{2.2}$$

in which the molecular vibration ν_m is defined as:

$$\nu_m = \frac{1}{2\pi}\sqrt{\frac{k}{\mu}}$$

Molecules thus vibrate following a cosine function, with a frequency determined by the bond strength and reduced mass. Each configuration of atoms in a molecule structure thus results in a unique vibrational motion, as a result of the unique reduced mass and strengths of the chemical bonds. This vibrational motion is related to the polarizability of the molecule α. The resulting dipole moment P is the product of the polarizability of the molecule with an incident EM source E_0, with frequency ν_0, and is expressed as:

$$P = \alpha E_0 \cos(2\pi\nu_0 t) \tag{2.3}$$

Using the assumption of small electric field amplitude, the polarizability can be expanded as a Taylor series:

$$\alpha = \alpha_0 + q\left(\frac{\partial \alpha}{\partial t}\right)_{q=0}$$

Inserting equations (2.2) and (2.3) into the above expression yields:

$$P = \underbrace{\alpha_0 E_0 \cos(2\pi\nu_0 t)}_{\text{Rayleigh scattering}} + \underbrace{q_0 \cos(2\pi\nu_m t) E_0 \cos(2\pi\nu_0 t) \left(\frac{\partial\alpha}{\partial t}\right)_{q=0}}_{\text{Raman scattering}}$$

The first term is the dominating Rayleigh scattering and the second term is Raman scattering. The Raman scattering term P_{RS} can be expanded using a trigonometric identity:

$$P_{\text{RS}} = q_0 E_0 \left(\frac{\partial\alpha}{\partial t}\right)_{q=0} \left[\underbrace{\cos(2\pi(\nu_0 - \nu_m)t)}_{\text{Stokes scattering}} + \underbrace{\cos(2\pi(\nu_0 + \nu_m)t)}_{\text{Anti-Stokes scattering}}\right]$$

There are thus three different types of interactions between a photon and the vibrational modes of a molecule. The majority of photons that scatter do so by Rayleigh scattering. However, a small fraction are inelastically scattered, in which photons with an energy $h\nu_0$ (ν_0 is the frequency and h is Planck's constant) may be annihilated upon interaction with an atom or molecule, with the simultaneous creation of a new photon with energy $h(\nu_0 - \nu_m)$, in which ν_m is the vibrational energy of the molecule. This is accompanied by a transition of the molecules to a higher excited vibrational state level by $h\nu_m$. If the molecule is initially in its excited state, the newly created photon has an energy $h(v_0 + v_m)$ [19]. Stokes scattering describes when the material absorbs more energy, and thus emits a photon with a lower energy than the incident photon, and anti-Stokes scattering describes when the material loses energy and the emitted photon has a higher energy. These mechanisms are illustrated in Figure 2.4

The spectrum obtained from Stokes and anti-Stokes shift is called the Raman spectrum. As the vibrational levels are populated according to the Boltzmann distribution, most molecules are at their ground state at room temperature and therefore, significantly less molecules are available for anti-Stokes scattering. Stokes scattering is thus significantly stronger and therefore most commonly used for detection and identification of molecules.

Raman spectroscopy requires the use of a monochromatic light source. Earlier, this consisted of a mercury lamp and a filter, while nowadays lasers are almost always used [20]. A notch filter or bandpass filter is used to filter out the scattered laser light and Rayleigh scattering. A spectrometer is used to image the spectrum. Raman spectra are typically plotted using wavenumbers in units of cm^{-1}, as this

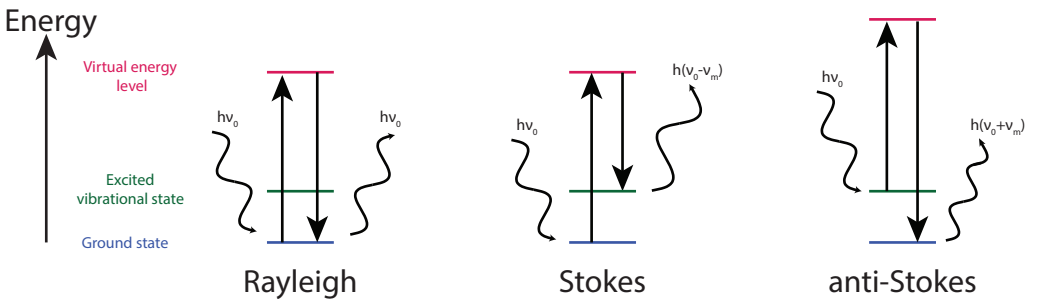

Figure 2.4: Illustration Raman scattering by Stokes shift. Most photons are scattered by Rayleigh scattering which is fully elastic. In the case in which the molecule falls to its excited vibrational state, the emitted photon has less energy than the incident photon. In the case the molecule was already in the the excited state and falls to its ground state, the emitted photon gains energy.

unit is directly related to energy. Wavenumbers are calculated as follows:

$$\Delta w = \left(\frac{1}{\lambda_0} - \frac{1}{\lambda_{\text{out}}} \right)$$

in which λ_0 is the wavelength of the incident light and λ_{out} is the wavelength of the measured emitted light.

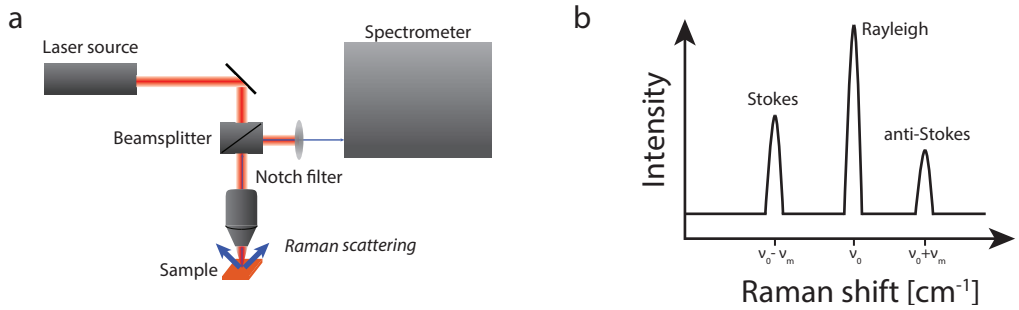

Figure 2.5: (a) A typical experimental setup used for Raman imaging. A laser source is focused onto a sample of interest. Raman scattered light is collected through the same focusing objective. Reflected as well as Rayleigh scattered light are filtered out through a bandpass or notch filter and the remaining Raman scattered light is imaged, using a spectrometer. (b) The three types of scattering, intensities not to scale. Raman spectra are usually plotted using wavenumber units (cm^{-1}).

Raman spectroscopy has seen massive increase in applications due in large part to the significant reduction in cost and improved performance of III-V semiconductor coherent laser sources, extremely sensitive CCDs for spectrometers and computational power for data treatment. Thus, Raman spectroscopy has become a common method to detect and identify molecules by revealing their unique vibrational fin-

gerprints, often with the use of hand-held instruments on-site [21].

Analysis of the quantum interpretation of the Raman effect reveals that the power of the Raman scattered light is proportional to the intensity of the incident photons I_0 as well as the Raman cross-section σ_R. While Raman scattering contains detailed spectral information of the vibrational modes of a molecule, the Raman effect is weak due to the low Raman cross-section of most molecules, typically $10^{-25} - 10^{-30}$ cm^2/molecule, compared to the fluorescence cross-section of effective fluorophores of around 10^{-16} cm^2/molecule [22]. For this reason, conventional Raman spectroscopy is limited to measurements with a large number of molecules and is unable to detect trace amounts of substances.

2.3 Surface Enhanced Raman Spectroscopy

Observations of a greatly increased Raman signal were made on pyridine adsorbed on electrochemically roughened silver by Fleischmann et al. in 1973 [23]. This gave rise to the field of surface enhanced Raman spectroscopy (SERS). These observations were followed by reports by Van Duyne et al. [24] and Albrecht et al. [25] that each proposed an enhancement mechanism: the electromagnetic and chemical effect. The electromagnetic enhancement effect is attributed to the LSPR modes of the metal nanostructures that focus the incident light energy at the surfaces. The chemical enhancement effect arises from changes in the molecular electronic state or due to resonant enhancements from existing molecular excitations or newly formed charge transfers. The electromagnetic enhancement explains enhancement factors up to $10^6 - 10^8$ for an ensemble of molecules and the chemical effect can provide an additional enhancement factor of $10^1 - 10^3$. This enormous increase in Raman signal greatly mitigates the inherently weak Raman scattering effect and allows for trace detection of chemicals, even single molecules [22].

In traditional Raman spectroscopy, the total Stokes Raman signal $I_{\mathrm{RS}}(\nu_{\mathrm{S}})$ is proportional to the Raman cross-section σ_{free}, the excitation laser intensity $I(\nu_0)$ and the number of molecules in the probed volume N [8]:

$$I_{\mathrm{RS}}(\nu_{\mathrm{S}}) = N\sigma^R I(\nu_0)$$

For SERS, the formula is modified, taking into account the EM enhancement as well as the chemical enhancement. The SERS Stokes signal is expressed as follows [11]:

$$I_{\mathrm{SERS}}(\nu_{\mathrm{S}}) = N' \underbrace{\sigma_{\mathrm{ads}}}_{\text{chemical}} \underbrace{|\eta(\nu_0)|^2 |\eta(\nu_S|^2 I(\nu_0)}_{\text{electromagnetic}} \tag{2.4}$$

in which $\eta(\nu_0)$ and $\eta(\nu_S)$ are the EM enhancement factors for the laser and for the Raman scattered field, σ_{ads} describes the increased Raman cross-section of a molecule adsorbed onto a metal surface, accounting for the chemical enhancement. N' denotes the number of molecules involved in the SERS process, usually those located in the enhanced EM field, and can be significantly lower than N.

The SERS enhancement is thus proportional to: $|\eta(\nu_0)|^2 |\eta(\nu_S|^2$. This term describes the physical process by which the dipole field of a LSPR-supporting structure induced by an external EM field, in turn, induces an oscillating dipole in the molecule. The Stokes radiation emanating from the molecule, although frequency shifted, couples to the LSPR mode of the nanostructure and is thus further enhanced.

The SERS signal I_{SERS} is thus proportional to the electric field enhancement and is greatest when the enhanced EM field is at its maximum. The increased intensity of the EM field around a LSPR-supporting structure can be inferred from the equations given in Section 2.1. Using the equation for the electrostatic potential outside the nanoparticle (2.1) and introducing the dipole moment of the sphere $\mathbf{p}$, the following equation is obtained for the electric field outside the sphere:

$$\mathbf{E}_{\mathrm{out}} = \mathbf{E}_0 + \frac{3\mathbf{n}(\mathbf{n}\cdot\mathbf{p} - \mathbf{p})}{4\pi\epsilon_0\epsilon_m} \frac{1}{r^3}$$

The field enhancement $\eta = |\mathbf{E}_{\mathrm{out}}/\mathbf{E}_0|$ can thus be expressed as [26]:

$$\eta = \left| 1 + 2\frac{a^3}{r^3} \frac{\epsilon_1 - \epsilon_m}{\epsilon_1 + 2\epsilon_m} \right|^2$$

From the above expression, the enhancement of the EM field is strongest at the Fröhlich condition ($\mathrm{Re}[\epsilon(\omega)] = -2\epsilon_m$) at the LSPR frequency. Additionally, the enhancement of the EM field is proportional to a^3/r^3, in which r is the distance from the center of the metal sphere and a is the radius. The EM enhancement is thus confined near the surface of the sphere. A calculation of the electric field distribution around such a silver nanosphere plotted as the enhancement is shown in Figure 2.6

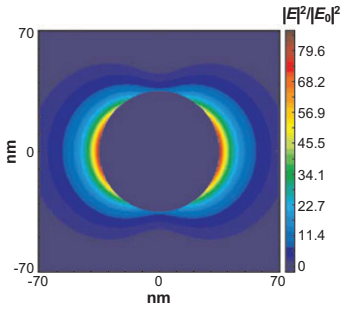

Figure 2.6: A calculation of the enhancement of the electric field around a spherical silver nanoparticle with a 35 nm radius in a vacuum. The field is enhanced to a maximum factor of 85, near the surface of the particle [11].

From equation (2.4), the SERS signal is expressed to be proportional to $|\eta(\nu_0)|^2|\eta(\nu_S|^2$. For small Stokes shifts ($\nu_0 \approx \nu_S$), $\eta(\nu_0)$ and $\eta(\nu_S)$ maximize at approximately the same wavelength. The SERS signal is thus proportional to the EM enhancement as follows:

$$I_{\text{SERS}} \propto |\eta(\nu_0)|^4$$

Inserting equation (2.3) into the above expression yields the following correlation:

$$I_{\text{SERS}} \propto \left(\frac{a}{r}\right)^{12} \left|\frac{\epsilon_1(\nu_0) - \epsilon_m(\nu_0)}{\epsilon_1(\nu_0) + 2\epsilon_m(\nu_0)}\right|^4$$

The SERS signal scales with the electric field to the fourth power (E^4) and decays from the surface with $1/r^{12}$, indicating that only molecules that are near the surface give a large SERS signal [27]. While chemical enhancement is a universal method to increase Raman signal, the electromagnetic enhancement using LSPR supporting nanostructures allows for optimization engineering to achieve high enhancement and make trace molecule detection viable by Raman spectroscopy. Typical SERS enhancements for single colloidal or gold spheroids are of the order of $10^6 - 10^7$ [28–30] but can be greatly increased with sharp features or large curvatures, resulting in a more focused EM field [8]. Additionally, closely spaced metal nanostructures can couple their dipole moments such that the field is further enhanced. For this type of coupling, enhancement factors up to 10^{11} have been reported [31].

Chapter 3

LSPR Refractive Index sensing and SERS Molecular Detection

Extensive research has been carried out to fabricate structures that exhibit plasmonic properties for sensing, either by refractive index (RI) sensing through wavelength shift of the LSPR modes or by SERS. Plasmonic substrates for sensing should have the following features:

- High sensitivity and figure-of-merit for RI sensing or enhancement factor (EF) for SERS
- High spatial unformity of LSPR wavelengths and EF for SERS
- Tunable LSPR wavelengths for RI sensing or broad LSPR lineshapes suitable for different laser excitation wavelengths and thus SERS
- Suitability for a broad range of sensing applications
- Robust, low-cost and commercially viable fabrication process

3.1 Refractive Index sensing

Sensitivity of the LSPR to RI changes is essential for detection of low concentrations of molecules. Changes in the RI of the local environment surrounding a metal nanoparticle, due to molecules adsorbed onto the surface are measured by the change in the maximum LSPR extinction wavelength $\lambda_{\max}$ and is expressed by the following equation [32, 33]:

$$\Delta\lambda_{\max} = m\Delta n\left(1 - e^{\left(\frac{-2d}{l_d}\right)}\right)$$

in which m is the bulk RI response of the nanoparticles (the sensitivity), Δn_{ads} is the change in RI surrounding the metal nanostructure due to the adsorbed molecules, d is the effective adsorbate layer thickness and l_d is the characteristic EM field decay length. The bulk RI response is calculated by measuring the shift of the LSPR extinction peak position as the bulk RI of the surrounding environment of the nanostructures changes:

$$m = \frac{\delta\lambda_{\max}}{\delta n}$$

in which δn is the change of the bulk RI. Analytical studies have shown that m is directly proportional to the LSPR wavelength position, and therefore have prompted fabrication of plasmonic metal nanostructures with near-infrared resonance wavelengths including nanorods, nanorings and core-shell nanoparticles [34]. A figure-of-merit (FoM) is used to directly compare the overall performance of a single nanoparticle as a chemical sensor. The FoM is defined as:

$$FoM = \frac{m}{P_{\text{FWHM}}}$$

in which P_{FWHM} is the full width at half maximum (FWHM) of the LSPR extinction peak. Determining FoM and FWHM from extinction spectrum measurements is illustrated in Figure 3.1.

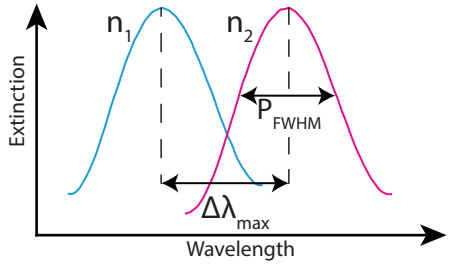

Figure 3.1: The figure-of-merit of a LSPR system is determined by dividing the shift of the LSPR extinction peak ($\Delta\lambda_{\max}$) with the change of refractive index from n_1 to n_2. This shift is compared to the full width at half maximum (P_{FWHM}) for the peaks.

When using macroscopic detection methods on a substrate with an ensemble

of metal nanostructures, the LSPR extinction peak FWHM broadens due to nanostructure polydispersity. For fabrication of large-area plasmonic substrates, this effect becomes highly relevant.

Detection of adsorbed molecules via LSPR extinction peak shift can be enhanced by reducing the characteristic EM field decay length l_d by using metal nanostructures with sharp corners to focus the EM field. RI sensing can also be improved by using chromophores that couple with the LSPR of the nanostructures as well as using metal nanostructures that have close proximity to each other and therefore exhibit plasmonic coupling with significant spectral shifts [35, 36]. While m and FoM give a strong indicator of LSPR RI sensing performance, actual sensor performance must be evaluated by measuring $\delta\lambda_{\max}$ and P_{FWHM} for application relevant biological and chemical molecules.

3.2 SERS enhancement factor

An ideal plasmonic substrate to carry out SERS should have a high and uniform EM enhancement in order to provide reliable Raman measurements. Spatial uniformity allows for quantification of molecules, as large-area Raman scattering scans can give an indication of the number of molecules in a sample. SERS performance is evaluated experimentally by determining the enhancement factor EF, expressed as [37]:

$$EF = \frac{(I_{\mathrm{SERS}}/N_{\mathrm{surf}})}{(I_{\mathrm{RS}}/N_{\mathrm{vol}})}$$

in which N_{surf} is the number of molecules probed by the SERS measurements and N_{RS} is the number of molecules probed by the Raman measurements. The calculation of EF thus requires a reference measurement carried out with traditional Raman spectroscopy. Additionally, the EF calculation necessitates knowledge of the number of molecules adsorbed onto the surface of the metal nanostructures and thus requires a calculation of the surface area of the metal nanostructures as well the footprint of the analyte molecule. For precise EF calculations, the EM field distribution for the LSPR mode must be calculated, in order to determine the fraction of the adsorbed molecules that are situated in regions with EM field enhancement. For large-area SERS substrates, an average EF is calculated using a monolayer of analyte molecules on the surface of the metal nanostructures. Uniformity of the SERS performance is calculated by determining the deviation of I_{SERS} scanned across a large area.

Chapter 4

Nanopillar substrates: SERS and Plasmonic Applications

Free standing nanopillars have shown to be an effective underlying structure for metal for plasmonic sensing. Nanopillars with vertical sidewalls provide areas that are elevated from the surrounding substrate, resulting in isolated metal nanostructures after an evaporation of a metal film, as illustrated in Figure 4.1. The shape and size of metal structures are determined by the morphology of the underlying nanopillars, the thickness of the evaporated layer as well as the adhesion between the metal and the material of the underlying nanopillars.

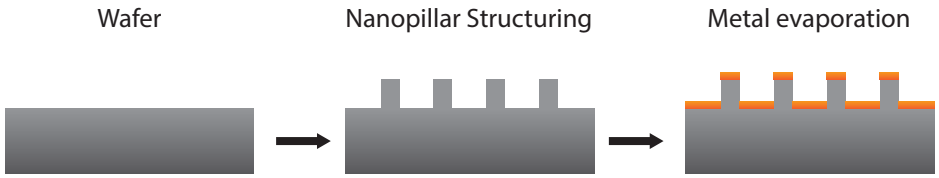

Figure 4.1: An illustration of the mechanism to achieve metal nanostructures using nanopillars. Nanostructuring of a wafer with height differences with vertical sidewalls cause a subsequently evaporated metal film to form isolated nanostructures at the tops of the pillars capable of supporting LSPRs.

In addition to being a straightforward method for fabricating LSPR supporting nanostructures, elevated metal structures address an intrinsic disadvantage of using surface-supported metal structures - the fixed RI of the supporting substrate reduces the overall RI sensitivity as well as the available area for molecules to adsorb onto the metal nanostructure surface [38]. Examples of the advantage to elevating the metal nanostructures for both LSPR RI sensing was demonstrated with gold 'mushroom' arrays by Shen et al. [39] and for SERS sensing by free-standing gold bowtie nanoantennas by Hatab et al. [40], as shown in Figure 4.2.

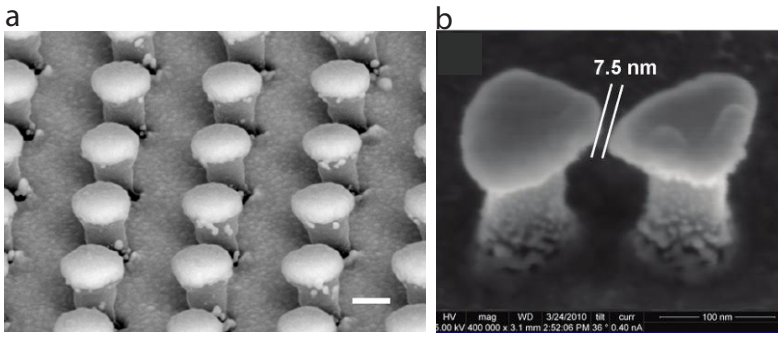

Figure 4.2: (a) Gold 'mushroom' arrays for LSPR RI sensing [39] (b) Free-standing gold bowtie nanoantennas for SERS [40].

Structures with dimensions at the nanoscale (< 1 μm) are fabricated either by top-down or bottom-up lithography approaches. For these structures, traditional UV-lithography methods do not have sufficient resolution and therefore, for plasmonic structures, the most common fabrication method has been bottom-up nanosphere lithography [41, 42] or top-down electron beam lithography [43, 44]. Nanosphere lithography (NSL) is an inexpensive fabrication method and has proven to be versatile in its ability to achieve raised metal nanostructures or metal nanocavities that support LSPR [45, 46]. However, NSL requires specialized knowledge and hands-on techniques for chemical synthesis of nanospheres, controlled spreading on a solid foundation as well as multiple steps of etching and metal depositions in order to achieve the desired structures. Robust large-area patterning on wafer scale has not been reliably demonstrated. For these reasons, NSL is not suitable for scaling up to high throughput production needed for industrial implementation. Electron beam lithography has the ability to produce nanostructures of arbitrary size, shape and spacing, however it is an extremely time-consuming and expensive process resulting in that only structuring of small areas is feasible. For these reasons, electron beam lithography is to a greater degree low throughput and unsuitable for scaling up [7].

Lithography-free reactive ion etching (RIE) has demonstrated the ability to nanostructure large areas using a single straightforward fabrication step. This process was developed predominantly on silicon, resulting in high aspect ratio nanopillars. This fabrication method typically utilizes a mixture of SF_6 and O_2 gases that are ionized to form a plasma and thereafter accelerated downwards towards the substrate. The ions etch away the surface by reacting chemically with the silicon material as well as physically knocking away material by kinetic energy. Initial inhomogeneity in the etching process is amplified by sidewall passivation and thus,

with the correct balance of etching parameters leads to densely packed high aspect ratio nanostructures [12].

By tuning the RIE process parameters and evaporating metal onto the tips of the silicon nanopillars, a substrate with densely packed isolated metal nanocaps was achieved by Schmidt et al. in the Nanoprobes research group at The Technical University of Denmark [13]. These structures are shown in a scanning electron microscope (SEM) image in Figure 4.3. These high density metal caps make up a state-of-the-art, high throughput SERS sensor. The substrate exhibits spatially uniform high EF over large areas [47].

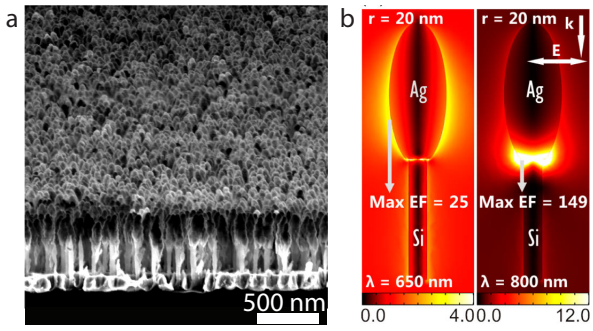

Figure 4.3: (a) A SEM image of dense silicon nanopillars with metal caps that support LSPRs and can be used for SERS. (b) A calculation of the EM field enhancement ($|E|/|E_0|$), showing a particle mode (left) and a cavity mode (right) at the base of the metal cap [48].

Wu et al.[47, 48] calculated the distribution of the EM enhancement around such metal nanocaps, showing significant field enhancement around the outside of the metal caps, and even stronger enhancement at the base. Measurements of the far field optical scattering showed a broad LSPR line shape in the near-infrared spectral region. The broadness of the measured absorption scattering peak is mainly due to the polydispersity of the metal caps. The EM field enhancement is significantly increased if the nanopillars lean towards each other, reducing the distance between gold surfaces and allowing LSPR modes to couple [47]. This leaning is typically induced by capillary forces of evaporating solvents on the surface after deposition of a dissolved analyte. For silver capped nanopillars, an enhancement factor of 10^8 is reported, with a relative standard deviation of 14% measured over a 5×5 mm surface area [48].

This technique of achieving LSPR supporting surfaces served as the starting point for fabricating transparent plasmonic substrates, using lithography-free fabrication methods developed in this Ph.D. research project. The SERS performance of glass and polymer substrates was evaluated against the high performance of silicon

nanopillars with gold caps after evaporation of a 225 nm gold layer. These processes involved adapting RIE to glass substrates, transferring the metal caps from the silicon nanopillars to a polymer foil, and using the nanopillars to create a mould for replication by polymer injection.

Chapter 5

Fabrication of Glass Nanopillar Structures

Glass nanopillar-based SERS substrates glass allow for Raman scattering measurements through the backside of the substrate. This facilitates working with opaque solutions on SERS substrates that would otherwise block the weak Raman optical signal when measured from the front. Additionally, the transparency allows the substrate to be used as a sensing window for measuring the contents of a chamber as well as for transmission Raman spectroscopy. Glass substrates made from fused silica feature exceptional optical transmission, low auto-fluorescence, biocompatibility, chemical and mechanical durability as well as low thermal conductance [49]. Anodic bonding can be carried out to incorporate fluidic designs in glass. Glass is also an insulator in contrast to n- or p- doped wafers used for silicon nanopillar SERS [50]. Electrodes can thus be incorporated by evaporating only metal in some areas, resulting in a substrate that can be used for both electrochemistry and SERS. In this Ph.D. research project, the RIE process was adapted from the silicon nanopillar fabrication technique in order to produce glass nanopillars.

5.1 Reactive ion etching process

SF_6 gas was used in plasma etching of glass, based on fluorine chemistry. The gas was ionized and accelerated towards the surface of the substrate. RIE was carried out using a plasma etching tool, consisting of a load lock mechanism to load wafers into a vacuum chamber. The vacuum chamber contained electrodes for electrostatic clamping of the wafer and an inlet for helium gas for cooling the backside of the wafer and an inlet system for several volatile or inert gases. Additionally, the chamber

contained two electrical systems: a coil that circled the chamber and oscillated an electric field at radio frequency in order to ionize the gas, and a static field which accelerated the ions towards the substrate. A turbo pump valve controlled the rate of pumping gas out of the chamber. By regulating the flow of gas into the chamber and the turbo pump valve, a constant pre-defined pressure was maintained in the chamber during plasma etching. The plasma etching tool with the load lock as well as the configuration of the chamber are illustrated in Figure 5.1.

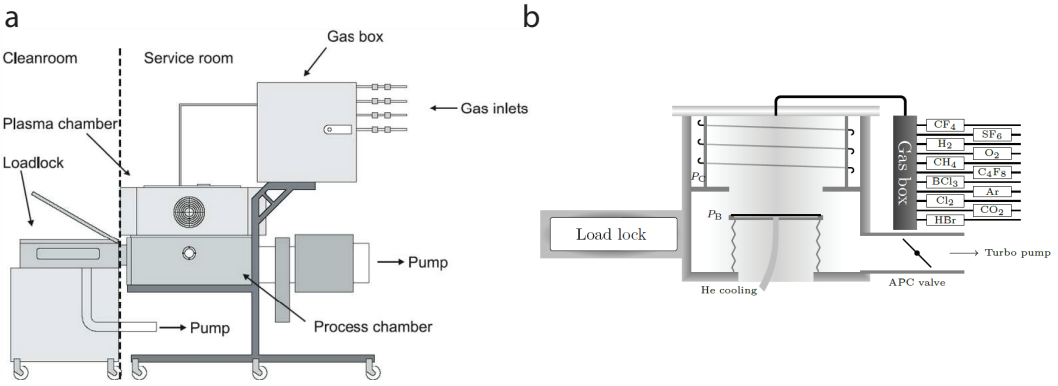

Figure 5.1: (a) An illustration of the plasma etching tool, including the load lock, the process chamber and the gas box with the gas inlets. (b) An illustration of the process chamber, showing the connection to the load lock, the position of the wafer when clamped and the coil used to generate the plasma.

The initial stochastic formation of nanostructures with RIE is usually attributed to redeposition of less-volatile products onto the surface during the etching process resulting in a local change of etch rate [12]. Further development of these initial nanostructures into nanopillars is usually explained as being due to the combination of ion deflection from sidewalls and redeposition of etching products. While this sufficiently explains nanostructuring of silicon, it does not explain structuring of fused silica due to the pureness of the silicon dioxide composition and therefore the lack of production of less-volatile products.

Lilienthal et al. [49] reported RIE nanostructuring of homogeneous glass without the use of any mask material and attributed nanostructuring to re-deposition of non-volatile sulfur fluorine reaction products with silicon oxide as the self-masking process. However, Hein et al. [51] reported that nanostructuring of glass was due to residual masking material from preceding etch runs and is therefore not reproducible as it depends on the conditions of the chamber based on the nature of the preceding runs. For this reason, research groups utilize either a polymer [52] or metal [53] as sacrificial thin film layers or as statically patterned areas in order to produce local nanoscale etching masks on the glass. Using this method, high concentrations of

less-volatile compounds are produced and spread over the surface in the first few seconds of plasma etching, producing local areas with lower etch rates [54, 55].

Using polymer as a sacrificial mask is advantageous as RIE tools are capable of creating polymer layers using CF_4 or other fluorocarbon gases under certain etching conditions. With this method, only a single tool is needed to achieve nanostructures in glass. However, metal is the preferred source for producing local nanomasks, due to the difficulty in controlling the polymer thickness [51]. Decrease of the glass etch rate due to the presence of Al, Ca and Na impurities has been shown by Metwalli et al. [54] and nanostructuring of glass has been demonstrated by Hein et al. [55] using Cu, Ag, In, Au as well as Ni and Al layers. With Ni and Al, it was reported that homogeneous glass nanostructuring could not be achieved, resulting in large unstructured areas. Despite this, Al was selected as the source of nanomasks for nanostructuring glass in this Ph.D. research project as the RIE tool used[1] prohibited the presence of other metals or impurities.

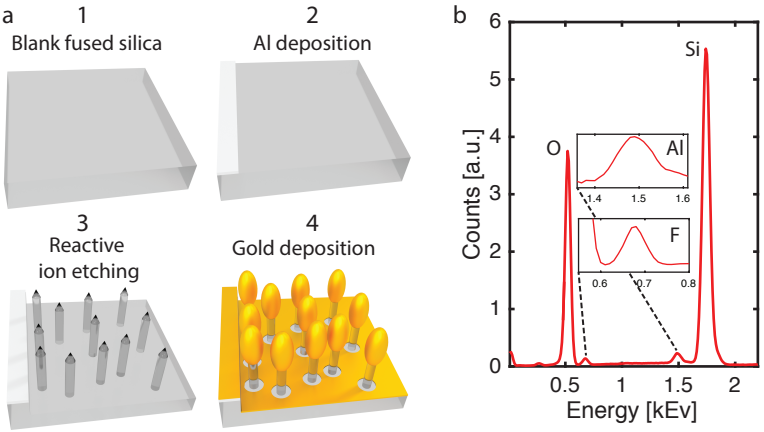

Figure 5.2: (a) An illustration of the fabrication method starting with a blank fused silica wafer, depositing Al through a shadowmask, followed by RIE nanostructuring and a gold evaporation step. (b) Energy-dispersive X-ray spectroscopy measurements of fused silica after RIE. Peaks for Al and F were detected, indicating the presence of local masks that decrease etch rate, leading to nanostructures.

Fabricating nanostructures was achieved by utilizing an Al layer that was deposited on certain areas of a fused silica wafer and balancing the RIE etching parameters. The Al areas had a thickness of 500 nm, and were thus not used as a sacrificial layer. This method was chosen as the RIE tool utilized electrodes for electrostatic clamping of the wafer, and therefore the Al layer must always be present. LSPR-supporting metal caps at the tips of the glass nanopillars are achieved with an e-beam evaporation, identical to process used for silicon nanopillar SERS.

[1] Advanced Oxide Etcher (STS MESC Multiplex ICP)

In this Ph.D. research project, gold was used due to its excellent plasmonic properties and longevity of shelf life in contrast to silver which oxidises. The fabrication process is illustrated in Figure 5.2. Energy-dispersive X-ray spectroscopy measurements, shown in Figure 5.2b, revealed the presence of Al and F on the surface, indicating that the etching process produced AlF_3. This compound is less-volatile [54] and thus induced local nanoscale regions with a lower etch rate, leading to nanostructures. The etching parameters must be balanced in order to achieve nanopillar structures. Additionally, the morphology is extremely sensitive to the conditions of the chamber as well as the configuration of the plasma etching tool [12] and must thus be re-optimized if components are changed or the process is transferred to another tool. The etching parameters and a broad range of different glass nanostructure morphologies are shown in Figure 5.3.

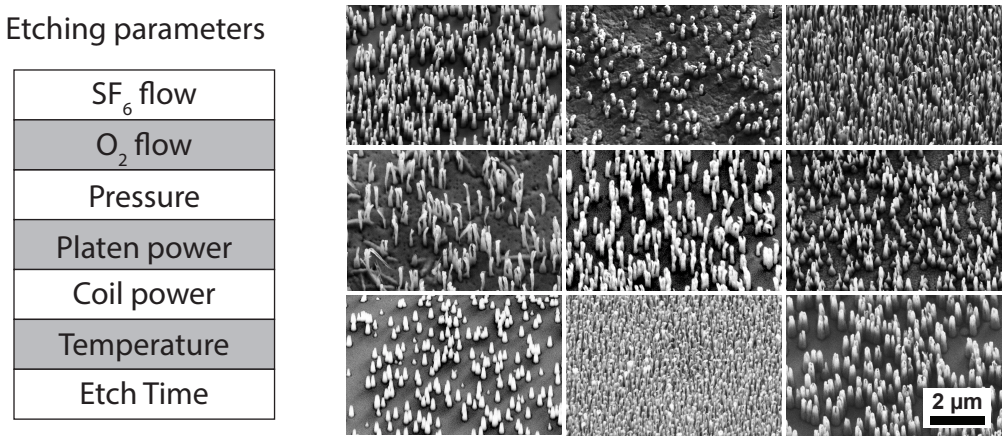

Figure 5.3: Eching parameters that can be varied and SEM images demonstrating the range of different morphologies that can be obtained using RIE of fused silica with Al patterned areas.

5.2 Wafer-scale homogeneity

The uniformity of the nanostructuring is dependent on the distance to the Al layer. This effect is mentioned in work by Hein et al. [51] and described in greater detail by Zeze et al. [53] in which non-sacrificial Al layers were used. The dependence of the distance to the Al layer was attributed to the electric field concentrations generated by the plasma electric field near the mask areas, affecting the ion flux and the angle of incidence during the plasma etch process. In addition to this effect, the redeposition of Al is also distance dependent. Thus, the combination of the electric-field distribution and the concentration of metallic impurities affects the morphology and especially the density of the nanopillars. In this Ph.D. research

project, initial shadow mask designs featured an outer ring and a significant density inhomogeneity was observed, with much lower density near the center of the wafer, and a much higher density near the Al ring. This density inhomogeneiety affects the SERS signal. This effect is shown in Figure 5.4.

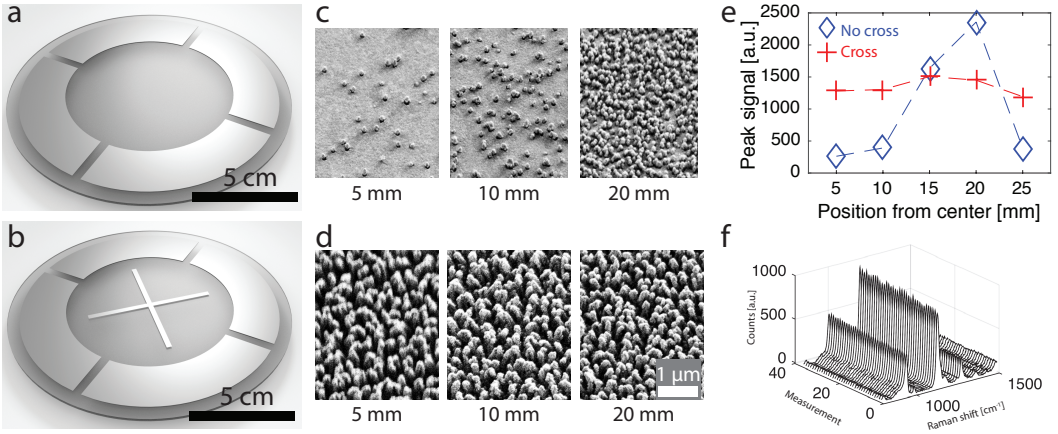

Figure 5.4: (a) Illustrations of the 4in fused silica wafers with the Al pattern without and (b) with the center cross. (c) SEM images of gold covered nanopillars taken at 5, 10 and 20 mm from the center of the wafer, showing increasing density and (d) constant density for the wafer with the Al cross. (e) A plot of the SERS signal at 1604 cm^{-1} for 100 μM trans-1,2-bis (4-pyridyl) ethylene, at different distances from the center, showing a varying signal for the wafer with no cross and a more homogeneous signal for the wafer with the cross. (f) A waterfall plot of different measurements showing a uniform Raman signal in a 10×10 μm area at position 10 mm from the center of the wafer with the cross.

The solution for this inhomogeneity was adding an Al cross at the center of the wafer, thus reducing the distance to Al patterned areas. SEM imaging and Raman measurements confirmed a homogeneous morphology and Raman signal across wafer scale areas.

5.3 SERS performance

In this Ph.D. research project, SERS performance was evaluated using trans-1,2-bis (4-pyridyl) ethylene (BPE) which is a suitable molecule as it features a intense and characteristic Raman bands located at about 1200 cm^{-1}, 1340 cm^{-1}, 1610 cm^{-1}, and 1640 cm^{-1} due to in-plane ring modes. Furthermore, it adsorbs well onto gold, has a well-known molecular footprint for EF calculation and has been used for many other studies of SERS performance [13, 56, 57]. Additionally, the well-documented molecular footprint of 30 $Å^2$ was used to calculate the number of molecules adsorbed onto the gold surface. Etching parameters used for optimized glass nanopillar SERS

performance are shown in Table 5.1.

SF_6 flow	170 sccm
O_2 flow	70 sccm
Pressure	75 mTorr
Platen power	110 W
Coil power	450 W
Chuck temperature	5°C
Etch time	4 min

Table 5.1: Etching parameters used

A 170 nm gold layer was deposited onto the glass nanopillars, resulting in the structures shown in Figure 5.5. Raman measurements were compared to the performance of the established silicon nanopillars SERS substrates. A similar SERS signal intensity was obtained for 100 μM concentration on a Raman microscope tool[2]. The relative standard deviation was found to be low at 4.9 %, evaluated for the 1611 cm^{-1} peak. A series of 900 spectra was made over a 3×3 mm area, positioned at the center of a 1 μL drop of BPE in ethanol. For these measurements, a 780 nm laser at a power of 5 mW, and an exposure time of 0.025 s was used with EM gain activated in the EMCCD of the spectrometer.

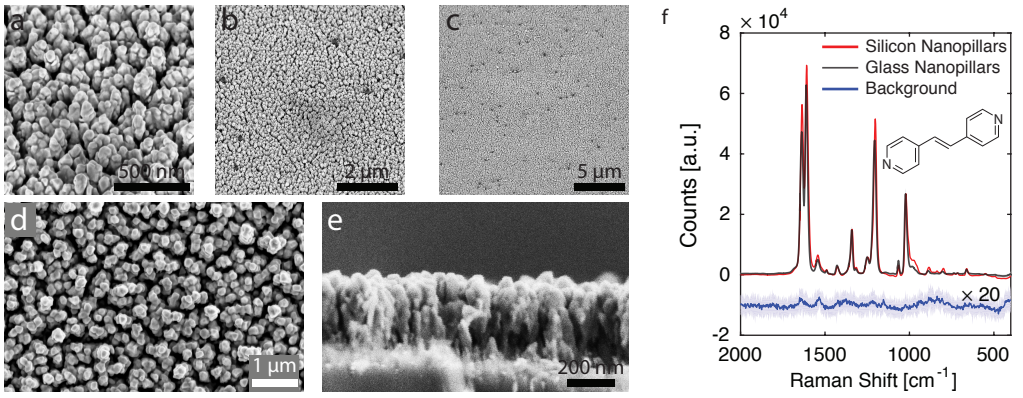

Figure 5.5: (a-c) SEM images taken at 30° tilt showing fused silica nanopillars after 170 nm gold evaporation, at different magnifications. (d) A top-down view showing the spacing of the metal caps. (e) A cross-sectional view. (f) Raman measurements for 100 μM BPE for silicon and fused silica nanopillars, showing a similar signal intensity. Background measurements, increased by a factor 20 in the plot, show a low background signal with few impurity peaks.

In addition to the good SERS performance, the glass substrate gives the possibility for Raman measurements from the backside. Comparing the performance to

[2]DXRxi Raman Imaging Microscope, Thermo Fisher Scientific

commercially available transparent or translucent substrates showed that the performance is significantly higher. The SERS measurements, using different commercially available substrates, are shown in Figure 5.6.

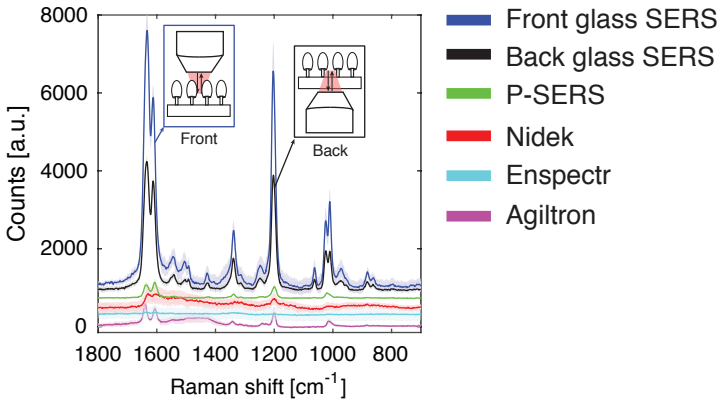

Figure 5.6: Raman spectra showing a 56 % in signal of the backside measurements compared to the those from the front. The other plotted spectra are from commercially available transparent SERS active substrates. Spectra have been shifted for clarity.

The measurements shown in Figure 5.6 were carried out with 1 mW laser power with an average of 3×1 s exposures, with an older Raman microscope[3]. The measurements showed that, despite a 56 % decrease in the Raman signal, the backside signal was significantly higher than commercially available transparent substrates, P-SERS, Nidek, Enspectr and Agiltron. Fused silica nanopillar SERS substrates are thus suitable for transmission measurements or backside measurements in cases that require a different optical setup or when working with opaque solutions.

5.4 Electrochemistry and SERS

The high resistivity of fused silica ($> 10^{18}$ Ωm) in comparison to n- or p-doped silicon (0.1 Ωm) allows the substrate to function as the underlying structure for electrodes. In this Ph.D. research project, electrodes on glass nanopillars were used both for electrochemistry and for SERS. This work is reported in the manuscript "Lithography-free Gold Capped Fused Silica Nanopillars for Electrochemistry and Surface Enhanced Raman Spectroscopy", in Chapter 11.

[3]DXR Raman Imaging Microscope, Thermo Fisher Scientific

Chapter 6

Polymer Injection Moulding of Nanopillars for SERS Applications

Injection moulding using thermoplastics is a well-established commercial production technique and can reliably replicate structures at the nanoscale [58]. In this Ph.D. research project, polymer injection replication of high aspectio ratio nanopillars was developed and utilized for creating SERS active surfaces with a high throughput fabrication technique.

6.1 Polymer injection

Traditional fabrication methods for producing SERS substrates have suffered from low throughput and not been a straightforward process, using traditional nanolithographic techniques such as electron beam or nanosphere lithography. While lithography-free RIE nanostructuring mitigates these shortcomings to a great degree, this process requires the use of advanced cleanroom facilities and is dependent on the stability of a plasma etching tool, as this process is extremely sensitive to chamber conditions. The nanostructuring production cycle time using lithography-free RIE is approximately 13 cm^2 of nanostructured area every 15 min with user-supervised tool operation, using silicon wafers at a unit cost of approximately €17 or €67 for fused silica wafers (in 2016).

Polymer injection is advantageous in that it is a widely deployed industrial fabrication tool and does not require specialized users or cleanroom facilities. Additionally, the morphology of the replicated structures is dependent on chamber conditions

to a much lesser degree than plasma etching. It is therefore a much more robust production platform resulting in reproducible morphology between batches. The cycle time to produce 13 cm^2 is under 4 min of unsupervised operation, meaning that the tool can be set to produce overnight, producing for example 180 large-area nanostructured samples over a 12 hour period. A mould can be used for production of thousands of samples and thus allows for true mass production of SERS substrates, facilitating more complex SERS studies, including cell studies, detection in complex solutions and quantification studies. The unit cost of each polymer moulded part is approximately €0.11 (in 2016), thus dramatically reducing the price of this nanostructuring fabrication step by more than two orders of magnitude.

In this Ph.D. research project, the injection moulding tool utilized a funnel for loading polymer granules which were melted and injected into a mould with an inserted design while the chamber was heated. Cyclic olefin copolymer (COC)[1] was used due to its optical clarity. The injection moulding tool is illustrated in Figure 6.1a. The melted polymer filled the cavities and the moulding chamber was subsequently cooled to allow the form to set. The chamber was opened at a cooler demoulding temperature and the moulded part was removed. This process is illustrated in Figure 6.1b.

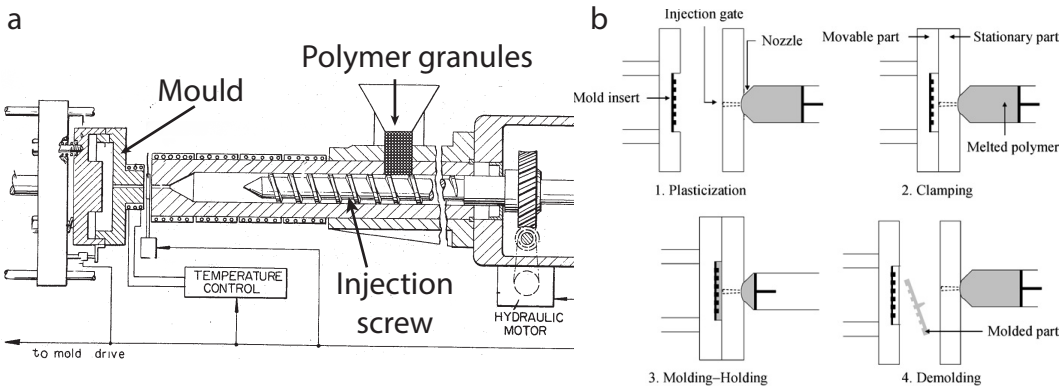

Figure 6.1: (a) An illustration of a screw polymer injection tool that uses a feeder for polymer granules and an injection screw to drive melted polymer into a mould. Adapted from [59]. (b) An illustration of the injection moulding process. Melted polymer is injected through an injection gate and into a chamber containing the mould insert with the design. After a mould-holding step, the chamber is opened and the moulded part is removed [60].

Polymer injection moulding has been traditionally used for macroscale structures. However, recent developments have advanced replication resolution to the microscale [60] and further to the nanoscale [61, 62]. One of the most challenging

[1]TOPAS 8007S-04 cyclic olefin copolymer, TOPAS Advanced Polymers, Germany

structures to replicate is high-aspect ratio pillars at the nanoscale. This was recently achieved at DTU Danchip facilities, Technical University of Denmark. Matschuk et al. [63] demonstrated the ability to produce nanopillars with a width of 40 nm and a height of 107 nm (aspect ratio of 2.7), with a regular 200 nm pitch.

6.2 Modification of the silicon RIE process

The structures replicated by Matschuk et al. [63] were fabricated using electron beam lithography which is unsuitable for patterning large areas for SERS. In this Ph.D. research project, the large-area silicon nanopillar substrates achieved by RIE were used to form the mould insert. This was a low-cost method for producing the mould, and resulted in large-area nanostructuring which would otherwise be infeasible to achieve via electron beam lithography. However, as the silicon nanopillars featured sidewalls with overhanging sections, they were found to be impossible to replicate accurately with polymer injection. For this reason, the process was modified by increasing the O_2 flow by 8.7%, thus decreasing chemical etch on the sidewalls of the nanopillars, causing sloped sidewalls with no overhanging segments. This change in morphology due to modification of the RIE parameters is shown in SEM images in Figure 6.2.

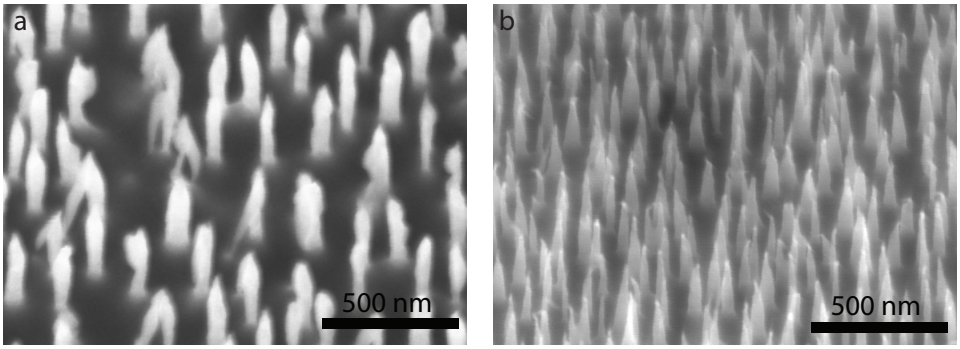

Figure 6.2: SEM images of silicon nanopillars using (a) the standard RIE parameters and (b) increasing the O_2 flow by 8.7%, causing increased chemical etch and thus sloped sidewalls.

6.3 Tuning polymer injection parameters

An optimization of the polymer injection process was carried out in order to accurately replicate the nanopillars. Polymer injection into the chamber containing the mould was controlled by seven parameters, listed in Figure 6.3. It was observed that

the injection process was especially dependent on moulding temperature T_{mould} and demoulding temperature T_{demould}.

It is crucial that the temperature at which moulding takes place is sufficiently high to decrease the viscosity of the polymer and thus fill the cavities of the inverted nanopillar geometry. The moulding temperature must therefore be higher than the glass transition temperature of the polymer ($T_{\text{g}} = 133°\text{C}$). The demoulding temperature is equally important, as it determines the viscosity of the polymer while the nanopillars are removed from the mould. If this temperature is too low, the nanopillars harden while still inside the cavity, adhere to the mould and tear off during demoulding. Conversely, if the temperature is too high, the polymer remains viscuous upon removal and the nanopillars bend.

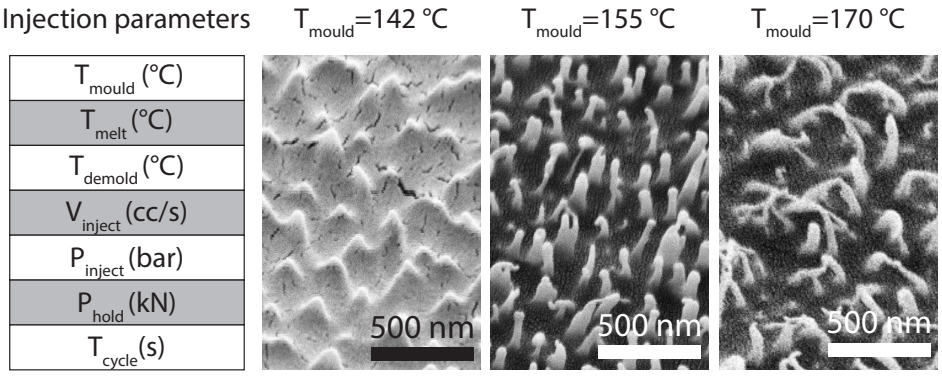

Figure 6.3: The parameters used to optimize the injection moulding process and SEM images of polymer injected nanopillars, using different moulding temperatures.

Figure 6.3 shows that the morphology of the polymer injected nanopillars changed with varying T_{mould}. For $T_{\text{mould}} = 142°\text{C}$, the polymer did not fill the nanocavities sufficiently. For $T_{\text{mould}} = 170°\text{C}$, the polymer injection tool did not have adequate time to cool sufficiently for demoulding, and therefore the nanopillars were unable to retain their shape.

6.4 SERS measurements

Large-area SERS active regions were achieved by nanopillar replication using polymer injection as a low-cost and high throughput fabrication process. Isolated gold metal caps were achieved with the same evaporation technique used for both silicon and glass nanopillars. A thickness of 190 nm of gold was chosen after an optimization series, resulting in gold capped polymer nanopillars, shown in Figure 6.4a-d.

SERS measurements were carried out using a 1 μL drop of BPE at a concentra-

tion of 100 μM. The laser power was 5 mW, the exposure time was 0.025 s and the EM gain was activated. The background was measured after exposure to pure water. Raman measurements of polymer injected nanopillars in comparison to gold-capped silicon nanopillars are shown in Figure 6.4f.

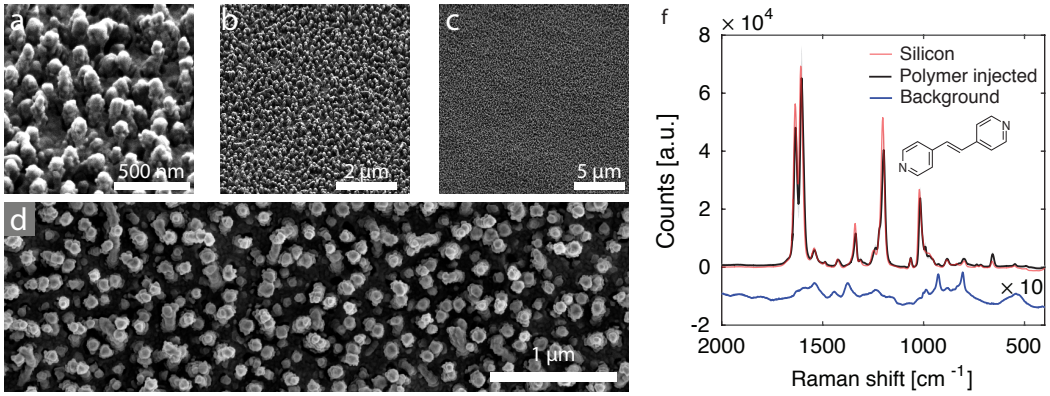

Figure 6.4: (a-c) SEM images taken at 35° tilt at different magnifications of the polymer injected nanopillars after deposition of a 190 nm gold layer, showing large areas achieved with isolated gold caps. (d) A top-down SEM image of the same structures. (f) Raman measurements showing the SERS performance in comparison to silicon as well as the background (shifted down and multiplied an order of magnitude).

Raman measurements showed that the Raman signal intensity was similar to that of the silicon nanopillars at this concentration. However, the background signal from the polymer substrate became significant, which can complicate low concentration measurements. Backside measurements were observed to have only 1.7% Raman signal intensity compared to the front. This low signal intensity is due to the thickness of the polymer substrate and gold planar areas that block optical access to the gold caps.

6.5 Towards achieving fluidic SERS

This fabrication process was used to achieve high-throughput fluidic devices for optical measurements due to the high precision of polymer injection moulding and optical clarity of COC. This allowed for mass production, which is suitable for commercial use as well rapid prototyping for microfluidic applications [64]. Ultrasonic welding facilitated the bonding of polymer pieces to achieve fluidic seals as well as macrofluidic interconnects. For these reasons, the polymer injected SERS substrates in this Ph.D. research project are ideal for integration into fluidic systems. This is reported in the manuscript "High-Throughput Gold Coated Polymer Injected Nanopillars for Surface Enhanced Raman Spectroscopy", in Chapter 12.

Chapter 7

Fabrication of Flexible and Transparent SERS Substrates

The existing optimized gold capped silicon nanopillars can be used to achieve a transparent and flexible SERS substrate by transfer of the gold caps to a polymer foil.

In this Ph.D. research project, transferring the gold caps from the silicon nanopillars to a polymer surface was achieved by applying heat and pressure in a controlled manner while the polymer foil and the gold caps at the tips of the nanopillars were in contact. This process was carried out using a compact nanoimprinting tool[1] that utilizes a ceramic plate with embedded electrical resistors for heating and a bladder that can be filled with compressed air to apply pressure. The tool and the imprinting stack are shown in Figure 7.1.

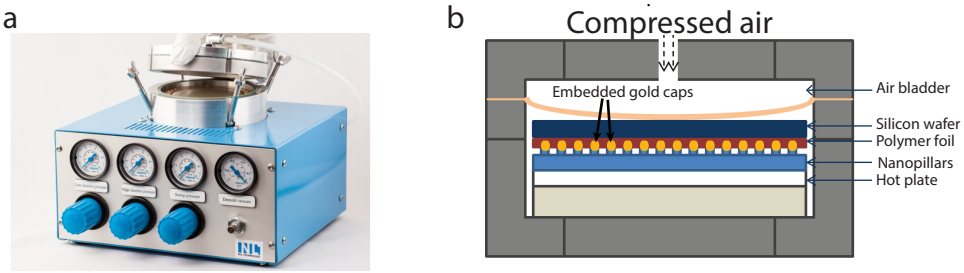

Figure 7.1: (a) A compact nanoimprint tool used for heating and applying pressure. (b) The stack built within the tool, consisting of the silicon nanopillars with gold caps, the polymer foil, encapsulated by a hot plate and a flat silicon substrate to keep the foil planar. The stack was heated by the hot plate and pressure was applied by filling an air bladder from above.

Using this process, transparent and flexible SERS active substrates were achieved

[1] CNI, NIL Technologies, Denmark

using only a single additional lithography-free and straightforward fabrication step.

7.1 Transfer optimization

To ensure a succesful transfer of metal nanocaps, the imprint parameters must be carefully balanced. These parameters are the imprinting temperature, the pressure, the demoulding temperature and the imprinting time. The imprint temperature must be greater than the glass transition temperature T_g, in order to melt the polymer and allow the metal caps to embed themselves. Sufficient pressure and time are needed to allow the caps to penetrate sufficiently in order to adhere. The demoulding temperature must be carefully controlled in order to make the polymer more viscuous and adhere to the gold nanocaps sufficiently to remove them from the silicon nanopillars. If the imprint temperature is too high and time too long, the nanocaps and silicon nanopillars will both be embedded in the polymer and the silicon nanopillars will detach from the silicon wafer. By carefully balancing these imprint parameters, a controlled transfer of only the gold caps is achieved. The imprinting parameters and examples of wafer-scale gold cap transfers to poly(methyl methacrylate) (PMMA) foil are shown in Figure 7.2, for two different imprint temperatures.

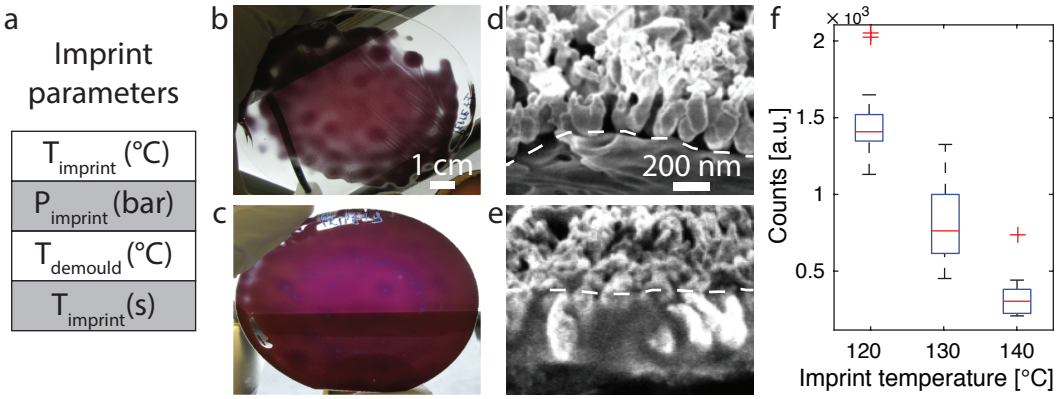

Figure 7.2: (a) Imprint parameters to achieve embedded nanocaps in polymer foils. (b) A photograph of wafer-scale PMMA foil with embedded nanocaps imprinted at 120°C and (c) at 140°C. (d) A cross-sectional SEM image of gold nanocaps embedded at the surface of the polymer after 120°C imprint and (e) nanocaps embedded deep in the polymer after 140°C imprint temperature. (f) Intensity of Raman measurements at the 1608 cm^{-1} peak for 100 μM BPE, as a function of imprint temperature, showing a dramatic decrease for higher imprint temperatures.

Figure 7.2b and c illustrate that higher imprint temperatures resulted in a more homogeneous wafer-scale transfer of gold caps. However, they were embedded much

deeper into the polymer layer (Figure 7.2e), causing a dramatic decrease in the intensity of the Raman signal, shown in Figure 7.2f. This showed a compromise between the homogeneity and size of the SERS-active region and the SERS performance.

7.2 SERS measurements

The initial motivation for transferring the gold nanocaps to the flexible and transparent polymer foil was to give access to the high enhancement cavity plasmonic mode at the base of the gold nanocaps [47], illustrated in Figure 4.3b. By removing the gold nanocaps from the silicon nanopillars and by embedding them upside-down in a polymer substrate, analyte molecules have much better access to adhere within the cavity in addition to allowing for easier optical measurements. However, Raman measurements showed a much lower SERS performance than expected. This could be due to damage to the nanocap morphology during imprint, shift of the LSPR wavelength due to removal of the silicon nanopillars, and polymer covering the caps, thus increasing the distance between the analyte molecules and the gold surface. An imprint temperature of 120°C, pressure of 4 bar, a demoulding temperature of 100°C and an imprint time of 8 min were used for optimized gold nanocap transfer for SERS. The wafer-scale metal nanocaps in PMMA foil are shown in the photograph in Figure 7.3 and in SEM images in Figure 7.3b.

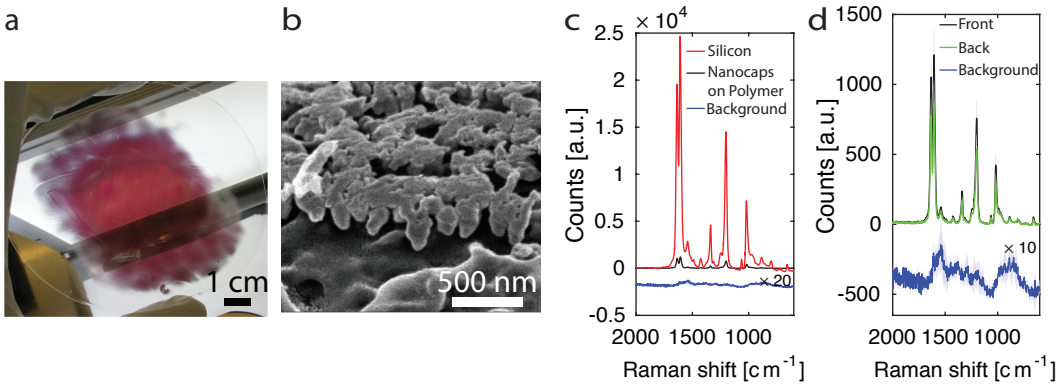

Figure 7.3: (a) A photograph of metal nanocaps after transferring of gold nanocaps, showing only partial wafer-scale transfer. (b) A cross-sectional SEM image of the transferred gold nanocaps on the polymer surface. (c) Raman measurements in comparison to gold-capped silicon nanopillars, showing a much lower SERS signal. (d) Raman measurements made both from the front and backside and background measurements.

The Raman measurements in Figure 7.3c show that SERS intensity is a factor of 20 lower in comparison to the gold-capped silicon nanopillars. These measurements

were taken on an older Raman microscope[2] with 1 μL BPE in ethanol deposited at a concentration of 100 μM. A 780 nm wavelength laser was used, at a power of 1 mW with a 1 s exposure time. There was no gain used with the spectrometer CCD. In addition to the low Raman signal, the polymer substrate for the transferred gold nanocaps resulted in a relatively high background signal, as shown in Figure 7.3d. The one advantage of this system is that very thin polymer foils can be used, in this case 100 μm thick PMMA. This, as well as the lack of a planar gold layer between the nanostructures, facilitated backside measurements, resulting in only a 29% lower signal for backside measurements in comparison to measurements taken from the front.

7.3 Oxygen plasma ashing of PMMA

The low Raman signal was in part due to a polymer layer on the surface of the gold structures, increasing the distance between the analyte molecules and the gold surface. By removing the outer polymer layer using plasma ashing, the surfaces of the gold nanocaps were exposed, greatly increasing the SERS performance by a factor of 12 in comparison to the performance of deeply embedded nanocaps. This mitigated the compromise between wafer-scale transfer and homogeneiety and SERS performance, as the nanocaps were first embedded deeply and uniformly, and subsequently uncovered when etching away the outer polymer layer. The polymer ashing for increasing the SERS performance is reported in the manuscript "Large-area, lithography-free fabrication of transparent and flexible substrates for surface-enhanced Raman spectroscopy", in Chapter 13.

[2]Raman DXR, Thermo Scientific

Chapter 8

Glass Nanocylinders with Gold Nanorings for LSPR Sensing

For certain plasma etching conditions, nanocylinders in fused silica can be fabricated instead of high aspect ratio nanopillars. Etching parameters that resulted in hollow-core nanocylinders consisted of a high ion acceleration (platen power) and a low pressure. In contrast to glass nanopillars, the morphology of the nanocylinders were found to be linearly dependent on the RIE process parameters, such that the height and diameter could be controlled. Glass nanocylinders using lithography-free RIE were previously reported by Zeze et al.[53] and by Lilienthal et al.[49]. However, no explanation was given for the process behind the formation of nanocylinders due to local nanoscale masks. A mechanism for the formation of nanocylinders is proposed in Figure 8.1. The actual process is most likely a complex combination of charging effects and a reduced physical etch rate of sidewalls.

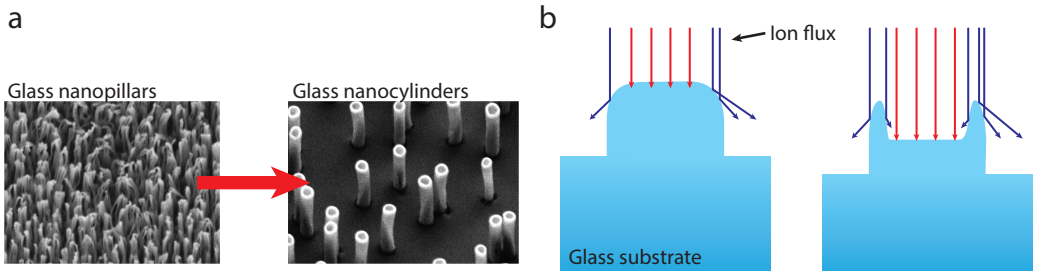

Figure 8.1: (a) SEM images showing the formation of glass hollow-core nanocylinders instead of densely packed nanopillars. (b) An illustration of a proposed mechanism for the formation of nanocylinders in which ions only at the center of the structure strike the substrate at an angle to etch away material.

Ions that strike the sidewalls at a glancing angle do not transfer sufficient kinetic

energy to cause physical etching. Ions that strike the center of the structures continue to etch material aways, resulting eventually in hollow-core nanocylinders.

Metal rings are of great theoretical and experimental interest as they support LSPRs in the near-infrared spectral region, with impressive refractive index sensitivity and FoM. Most notably, these nanoring metal structures are highly tunable, allowing the LSPR extinction peak to be shifted when the metal geometry is changed [65, 66]. Fused silica hollow-core nanocylinders served as the underlying structure for suspended metal nanorings. These metal rings, or rather tori, straddled the top edges of the nanocylinders and supported LSPR modes.

8.1 Improving nanocylinder uniformity

A significant challenge to suspended metal nanorings with tunable LSPR wavelength was to achieve wafer-scale homogeneous morphology. As with the nanopillars, the density of the nanostructures correlated to the distance to the Al layer. However, in contrast to the nanopillars, the density of the nanocylinders was found to vary randomly in macroscale regions across the entire wafer, as shown in the SEM images of Figure 8.2c.

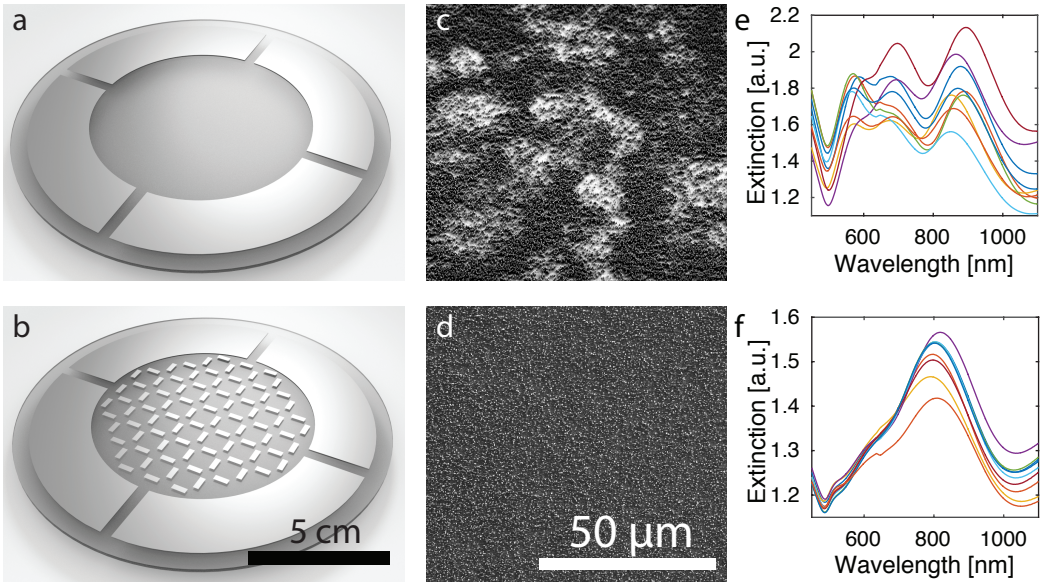

Figure 8.2: (a,b) Al layer patterns with and without a rectangular array, resulting in (c) inhomogeneous and (d) homogeneous density of nanocylinders, thereby resulting in a spread (e) or more collected (f) LSPR extinction peaks.

The observed inhomogeneity is in accordance with the effect of using Al as a mask, reported by Hein et al.[55]. As the LSPR peak is highly dependent on den-

sity, the LSPR peaks shifted when nanocylinder density is changed. The resulting variance of LSPR extinction peak wavelengths is shown in Figure 8.2e. This inhomogeneiety of nanocylinder density was mitigated with additional Al patterns and it was observed that the cross used previously was insufficient. For this reason, an array of Al rectangles were added to ensure an even distribution of Al nanomasks to achieve a uniform density of nanocylinders, thus significantly reducing the variance in the position of the LSPR extinction peak. The resulting extinction measurements are shown in Figure 8.2f.

8.2 LSPR tunability and sensing performance

The peer-reviewed article "Lithography-Free Fabrication of Silica Nanocylinders with Suspended Gold Nanorings for LSPR-Based Sensing" in Chapter 14 reports control of the geometry of the fused silica nanocylinders and the tuning of the LSPR extinction peak. Calculations of the sensitivity, as well as the FoM of the system were carried out. The article concludes with demonstrating surface sensing using biomolecules and proposes the system as a highly sensitive, high throughput and tunable substrate for chemical and biological sensing.

Chapter 9

Discussion

A comparison of the three SERS substrates that were fabricated during this Ph.D. project is made with respect to SERS performance, fabrication and usability in order to evaluate them as potential sensing platforms. The three substrates are: (i) gold capped glass nanopillars achieved via RIE; (ii) gold caps embedded in a polymer substrate achieved via imprinting and transfer from the silicon nanopillars; and (iii) gold capped polymer nanopillars achieved with injection moulding.

9.1 SERS comparison

Raman measurements, relative to the gold-capped silicon nanopillars used as a benchmark, were carried out for a 1 μL drop of 100 μM BPE from both the front and the backside of each SERS substrate, shown in Figure 9.1.

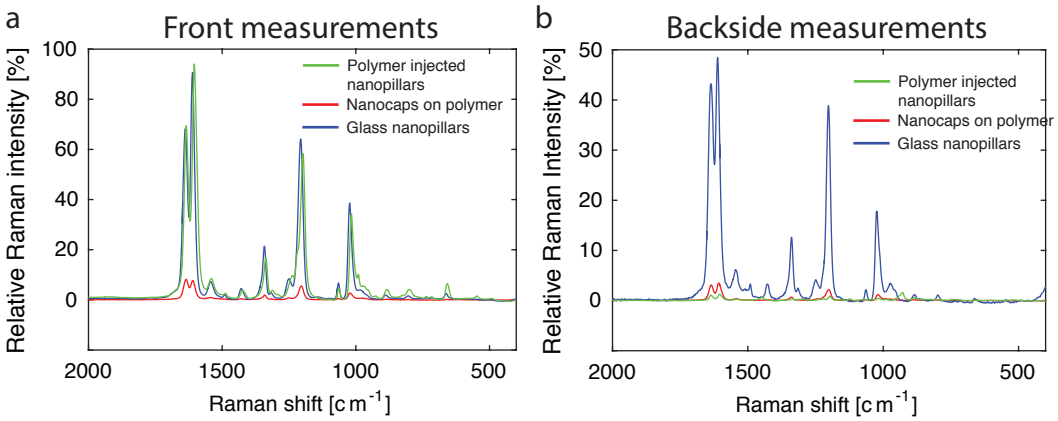

Figure 9.1: Raman measurements of 100 μM BPE relative to the SERS performance of the gold-capped silicon nanopillars. Measurements were carried out from the front (a) and (b) from the backside.

The gold-capped polymer injected nanopillars performed best, showing a 94% Raman signal intensity, relative to the gold-capped silicon nanopillars. The gold-capped glass nanopillars also performed well, at 91% Raman signal intensity. The gold nanocaps transferred to the polymer fared worst, at only 8% Raman signal intensity. However, measured from the backside, polymer injected nanopillars showed an extremely low Raman signal intensity due to the thick polymer layer and gold planar regions. In comparison to front measurements, backside measurements for polymer injected nanopillars have only 1.7% of the intensity. The backside measurements of the gold nanocaps transferred to the polymer had thus a higher Raman signal intensity than the gold-capped polymer injected nanopillars. This relatively high backside Raman signal intensity was due to the thinness of the polymer foil and the lack of planar gold areas. For the glass nanopillars, the optical clarity and thinness of the fused silica substrate, combined with the high density of nanopillars, which minimised the gold planar areas, resulted in the highest backside Raman signal intensity.

Background Raman measurement were performed on all three substrates after exposure to ethanol. The background signal is shown relative to the front Raman measurement for each substrate, in order to evaluate the signal to noise ratio. Low background signal is desirable for carrying out ultra-low concentration measurements as the background begins to interfere with detection if the Raman peaks from the analyte molecule have low intensity. The relative Raman intensity of the background signal for each substrate is shown in Figure 9.2.

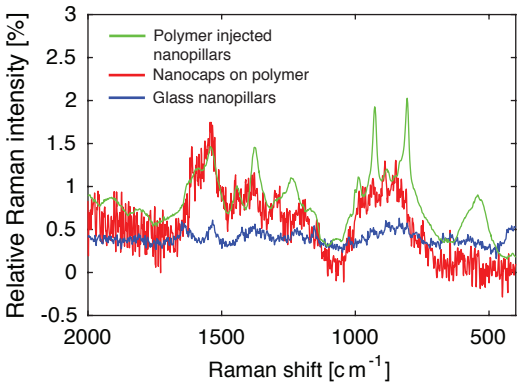

Figure 9.2: Background measurements of the three SERS-active substrates achieved in this Ph.D. research project. The Raman signal is relative to the front measurement for each substrate. The gold nanocaps transferred onto polymer as well as the gold-capped polymer injected nanopillars showed clear background peaks due to the polymer substrate. The glass nanopillar substrate showed the lowest background.

From the measurements shown in Figure 9.2, it is evident that the gold nanocaps

on polymer as well as the polymer injected nanopillars showed a relatively high background signal due to the polymer substrate. The glass nanopillar substrate was superior, showing the lowest background signal and thus, most suitable for ultra-low concentration detection of analytes.

SERS substrates are typically characterized by the enhancement factor (EF), expressed in the equation:

$$EF = \frac{(I_{\mathrm{SERS}}/N_{\mathrm{SERS}})}{(I_{\mathrm{RS}}/N_{\mathrm{vol}})}$$

The number of molecules N_{vol} involved in producing the intensity of a Raman measurement I_{RS} was estimated by measurement of 0.1 M BPE in ethanol in a petri dish with no SERS substrate. The number of molecules involved in Raman scattering was estimated to be 3.6×10^9, assuming an interaction volume between the laser used for Raman measurement and the liquid of 60 μm^3. A Raman signal intensity of $I_{\mathrm{RS}} = 1.4$ counts mW^{-1}s^{-1} for the 1200 cm^{-1} peak was measured.

In order to estimate a value for the number of molecules involved in the SERS process N_{SERS} and the SERS intensity I_{SERS}, 5 μL of 1 mM BPE in ethanol was deposited onto each substrate and the solvent was allowed to evaporate. Using the same Raman measurement parameters as for I_{RS}, values for I_{SERS} were 29330, 24500 and 2000 counts mW^{-1}s^{-1} for the 1200 cm^{-1} peak for the glass nanopillar SERS, the polymer injected nanopillar SERS and the nanocap on polymer foil substrates, respectively. The number of molecules involved in SERS N_{SERS} was estimated by assuming a monolayer of BPE on all gold nanostructure surfaces and a 30 Å^2 molecular footprint [56]. Taking the topography of the gold nanostructures into consideration, the number of molecules involved in SERS per gold nanostructure was estimated to 3.78×10^5, 4.32×10^5 and 3.67×10^5 for the glass nanopillars, the polymer injected nanopillars and the transferred metal nanocaps, respectively. With gold nanostructure densities of 100, 18 and 18 caps/μm^2 and a laser spot size of 0.8 μm in radius, N_{SERS} was estimated to be 3.78×10^7, 7.78×10^6, and 1.33×10^7 for the glass nanopillar SERS, polymer injection nanopillar SERS and transferred gold nanocaps, respectively. The calculated average EF is thus calculated to 2.0×10^6, 8.1×10^6 and 2.0×10^5 for glass nanopillar SERS, polymer injection nanopillar SERS and transferred gold nanocaps, respectively.

These calculated EFs for the substrates are averaged values, obtained by assuming that all the adsorbed molecules contributed equally to the SERS signal. As the SERS enhancement is highly related to the strength of the EM field, the largest contribution to the collected SERS signal is from molecules that are located in the

EM hot spots. Taking this into consideration yields a significantly higher value for EF. Calculating the number of molecules involved requires determining the shape of the EM enhancement field around the metal nanostructures. This calculation was only carried out for the transferred metal nanocaps (see Chapter 13), such that a more accurate N_{SERS} can be calculated. A conservative estimation was made, assuming that 5% of the adsorbed molecules were located in enhanced EM field regions. Thus, a more accurate EF of 8.0×10^6 was obtained for the transferred gold nanocaps. Similarly, calculating the percentage of molecules situated in EM enhanced regions for the glass nanopillars and polymer injected nanopillars would yield an approximately 10 times higher calculated EF value.

9.2 Fabrication comparison

The three SERS substrates produced in this Ph.D. project were achieved using significantly different fabrication pathways, each with advantages and disadvantages. The fabrication tools used, the robustness of the process, the cost and the applications for the substrate are discussed below.

As with the silicon nanopillars, glass nanopillars require a plasma etching chamber. The morphology of the nanopillars are highly sensitive to the conditions of the chamber. For this reason, achieving glass nanopillars with high SERS performance requires re-optimization of the etching parameters, as the plasma etching tool has often been re-configured or has drifted out of calibration. In addition, the aluminum deposition step, using e-beam evaporation and the high price of the fused silica wafers, make large-scale fabrication user-intensive, time-consuming and costly in relation to the two other fabrication pathways. These relative disadvantages are mitigated by the high SERS performance and unrivalled backside Raman signal intensity with a low background signal. This makes the glass nanopillars suitable for ultra-low concentration detection, even when measuring from the backside. In addition, it makes the glass nanopillar SERS substrate suitable for integration in microfluidic systems for *in situ* Raman probing of the fluid or as a window into a gas chamber for measuring the contents. While the process can be scaled up to mass production, the wafer price of €67, as well as the processing time must be considered.

Transfer of the metal nanocaps to a polymer foil utilizes plasma etching of a silicon wafer that must be carried out for each SERS substrate. Silicon nanopillars could be reused, such that an additional gold deposition would result in new metal nanocaps that could be transferred to another polymer foil. However, this was not

investigated. The imprint process to transfer the metal nanocaps is straightforward once the fabrication parameters have been optimized and is robust. This is also true for the subsequent oxygen plasma ash, used to remove residual polymer on the gold nanocaps and to increase the SERS performance. Unfortunately, gold nanocaps transferred to polymer foil exhibit a much lower SERS performance even after oxygen plasma etching. However, the backside Raman signal is higher than that of the polymer injected nanopillars. This backside performance, in combination with the polymer substrate, potentially makes it more suitable for integration in microfluidic systems that require backside Raman measurements. However, this fabrication process does not match the robustness and scalability of the polymer injected nanopillars.

Polymer injected nanopillars utilize a plasma etched silicon wafer cast as a nickel shim as a mould. Thus, the initial fabrication process is dependent on nanostructuring using RIE. However, it needs to be carried out only once, as a mould can endure hundreds and likely thousands of injection cycles. The mould fabrication process requires nickel vanadium deposition and nickel electrodeposition, followed by a potassium hydroxide etch to remove the silicon wafer and form the nickel shim as a mould for polymer injection. While this is a cumbersome process, none of these steps require optimization. Once the nickel mould is produced, fabrication of nanopillars requires no re-optimization, as the morphology is not highly sensitive to the machine configuration. Polymer injection is thus a much more robust process, suitable for reliable production of large quantities of high performance SERS samples with similar performance to that of the silicon nanopillars. However, the background Raman signal is relatively high due to the polymer substrate. This can interfere with ultra-low concentration detection. Also, the backside signal is extremely low due in part to the thickness of the polymer substrate, making the substrate largely unsuitable for backside detection of analyte. Polymer injected nanopillars have a extremely low cost of production, with low material cost and using a common industrial tool for fabrication and are thus suitable for mass production. Lastly, the polymer substrate allows for adhesion bonding or ultrasonic welding to other polymer parts, facilitating an easy integration into microfluidic systems.

Chapter 10

Conclusion and Perspectives

Four types of transparent substrates with metal nanostructures were achieved during the course of this Ph.D. research project and these were evaluated for SERS applications and LSPR-based molecular detection. These substrates were; (i) glass nanopillars achieved in fused silica with RIE with gold caps for SERS sensing; (ii) polymer nanopillars achieved by polymer injection with gold caps for SERS detection; (iii) transferred gold caps to a polymer foil as a SERS substrate; and (iv) fused silica hollow-core nanocylinders with gold nanorings for LSPR RI sensing and molecule binding events.

A RIE-based fabrication method was developed and optimized for glass wafers to obtain high density nanopillars as the underlying structure for isolated gold caps for SERS detection as well electrodes for electrochemistry measurements. An imprint method was developed for transferring metal caps from the tips of silicon nanopillars to a transparent polymer foil for SERS sensing. A mould form and polymer injection method for achieving polymer nanopillars as the underlying structure for metal caps for SERS as well as fluidic integration were developed. Additionally, a RIE fabrication method for glass wafers was developed to achieve hollow nanocylinders as the underlying structure for suspended plasmonic rings for LSPR RI sensing. The ability to tune the morphology and LSPR wavelengths using the etching parameters was determined.

The SERS active substrates offer a state-of-the-art Raman enhancement platform. While the glass nanopillars and transferred gold nanocaps exhibit the best backside SERS performance, the polymer injected nanopillars utilize the most robust and high throughput method and feature the highest SERS intensity. The hollow-core nanocylinders with suspended gold nanorings provide a state-of-the-art plasmonic substrate for LSPR RI sensing with high sensitivity and FoM and offers the ability to tune the LSPR wavelength by modifying the etching parameters.

Future research should investigate whether traditional surface plasmon resonance, using a prism and backside illumination of a laser, could be used to launch surface plasmon polaritons that couple to the LSPRs for simultaneous SPR, LSPR RI and perhaps also SERS.

Additionally, the EM field enhancement distribution of the LSPR modes for the gold-capped glass nanopillars and the gold-capped polymer nanopillars should be calculated. This would give a better understanding of the reason for the high SERS intensity as well as a more accurate calculation of EF. This knowledge would allow for further optimization for better SERS performance.

The transparency of the SERS active substrates should be applied for detection of relevant molecules. This should include research using different optical setups such as transmission Raman spectroscopy and detection of analyte in challenging opaque solutions such as blood or dairy products.

The possibility for ultrasonic welding to seal polymer injected microfluidic devices to a polymer nanopillar SERS substrate allows for true high throughput production of samples. This feature should be utilized for large-scale studies that require sample handling, functionalization and multiplexing, using *in situ* SERS as a sensitive molecular fingerprint detection and identification method.

Bibliography

[1] Stefan A. Maier. *Plasmonics: Fundamentals and Applications*. Number 1. sep 2007. Cited on pages 1, 9.

[2] Philip D Howes, Subinoy Rana, and Molly M Stevens. Plasmonic nanomaterials for biodiagnostics. *Chemical Society reviews*, 43(11):3835–53, 2014. Cited on page 1.

[3] Marc D Porter, Robert J Lipert, Lorraine M Siperko, Gufeng Wang, and Radha Narayanan. SERS as a bioassay platform: fundamentals, design, and applications. *Chemical Society reviews*, 37(5):1001–1011, 2008. Cited on page 1.

[4] Borja Sepúlveda, Paula C. Angelomé, Laura M. Lechuga, and Luis M. Liz-Marzán. LSPR-based nanobiosensors. *Nano Today*, 4(3):244–251, 2009. Cited on page 1.

[5] Rebecca A. Halvorson and Peter J. Vikesland. Surface-enhanced Raman spectroscopy (SERS) for environmental analyses. *Environmental Science and Technology*, 44(20):7749–7755, 2010. Cited on page 1.

[6] Ana Paula Craig, Adriana S Franca, and Joseph Irudayaraj. Surface-enhanced Raman spectroscopy applied to food safety. *Annual review of food science and technology*, 4:369–80, 2013. Cited on page 1.

[7] Katherine A Willets and Richard P Van Duyne. Localized surface plasmon resonance spectroscopy and sensing. *Annual review of physical chemistry*, 58:267–97, jan 2007. Cited on pages 1, 22.

[8] Katrin Kneipp, Harald Kneipp, Irving Itzkan, Ramachandra R Dasari, and Michael S Feld. Surface-enhanced Raman scattering and biophysics. *Journal of Physics: Condensed Matter*, 14(18):R597–R624, 2002. Cited on pages 2, 14, 16.

[9] Kyle C Bantz, Audrey F Meyer, Nathan J Wittenberg, Hyungsoon Im, Ozge Kurtuluş, Si Hoon Lee, Nathan C Lindquist, Sang-Hyun Oh, and Christy L

Haynes. Recent progress in SERS biosensing. *Physical chemistry chemical physics : PCCP*, 13(24):11551–67, 2011. Cited on page 2.

[10] Jeffrey N Anker, W Paige Hall, Olga Lyandres, Nilam C Shah, Jing Zhao, and Richard P Van Duyne. Biosensing with plasmonic nanosensors. *Nature materials*, 7(June):442–453, 2008. Cited on page 2.

[11] Paul L. Stiles, Jon A. Dieringer, Nilam C. Shah, and Richard P. Van Duyne. Surface-Enhanced Raman Spectroscopy. *Annual Review of Analytical Chemistry*, 1(1):601–626, jul 2008. Cited on pages 2, 14, 16.

[12] H Jansen, M Deboer, R Legtenberg, and M Elwenspoek. The Black Silicon Method - A Universal Method For Determining the Parameter Setting of A Fluorine-based Reactive Ion Etcher In Deep Silicon Trench Etching With Profile Control. *Journal of Micromechanics and Microengineering*, 5(2):115–120, 1995. Cited on pages 2, 23, 26, 28.

[13] Michael Stenbaek Schmidt, Jörg Hübner, and Anja Boisen. Large area fabrication of leaning silicon nanopillars for surface enhanced Raman spectroscopy. *Advanced materials (Deerfield Beach, Fla.)*, 24(10):OP11–8, mar 2012. Cited on pages 3, 23, 29.

[14] Gustav Mie. Beiträge zur Optik trüber Medien, speziell kolloidaler Metallösungen. *Annalen der Physik*, 330(3):377–445, 1908. Cited on page 7.

[15] E. Kretschmann and H. Raether. Notizen: Radiative Decay of Non Radiative Surface Plasmons Excited by Light. *Zeitschrift für Naturforschung A*, 23(12):2135–2136, jan 1968. Cited on page 7.

[16] A Otto. Theory of Plasmon Excitation in Thin Films by Electrons of Non-Normal Incidence. *physica status solidi (b)*, 22(2):401–406, 1967. Cited on page 7.

[17] Craig F. Bohren and Donald R. Huffman. *Absorption and Scattering of Light by Small Particles*. John Wiley & Sons, 2008. Cited on page 10.

[18] Chandrasekhara Venkata Raman and Kariamanikkam Srinivasa Krishnan. A new type of secondary radiation. *Nature*, 121:501–502, 1928. Cited on page 10.

[19] Andrzej Kudelski. Analytical applications of Raman spectroscopy. *Talanta*, 76(1):1–8, 2008. Cited on page 12.

[20] Richard L McCreery. Photometric Standards for Raman Spectroscopy. In *Handbook of Vibrational Spectroscopy*. John Wiley & Sons, Ltd, 2006. Cited on page 12.

[21] Aron Hakonen, Per Ola Andersson, Michael Stenbæk Schmidt, Tomas Rindzevicius, and Mikael Käll. Explosive and chemical threat detection by surface-enhanced Raman scattering: A review. *Analytica Chimica Acta*, 893:1–13, 2015. Cited on page 14.

[22] Katrin Kneipp, Yang Wang, Harald Kneipp, Lev T Perelman, Irving Itzkan, Ramachandra R. Dasari, and Michael S. Feld. Single Molecule Detection Using Surface-Enhanced Raman Scattering (SERS). *Physical Review Letters*, 78(9):1667–1670, mar 1997. Cited on page 14.

[23] M. Fleischmann, P.J. Hendra, and A.J. McQuillan. Raman spectra of pyridine adsorbed at a silver electrode. *Chemical Physics Letters*, 26(2):163–166, may 1974. Cited on page 14.

[24] David L. Jeanmaire and Richard P. Van Duyne. Surface raman spectroelectrochemistry. *Journal of Electroanalytical Chemistry and Interfacial Electrochemistry*, 84(1):1–20, nov 1977. Cited on page 14.

[25] M. Grant Albrecht and J. Alan Creighton. Anomalously intense Raman spectra of pyridine at a silver electrode. *Journal of the American Chemical Society*, 99(15):5215–5217, jun 1977. Cited on page 14.

[26] Jyoti Katyal and R K Soni. Field Enhancement Around Al Nanostructures in the DUV–Visible Region. *Plasmonics*, 10(6):1729–1740, dec 2015. Cited on page 15.

[27] George C. Schatz, Matthew A. Young, and Richard P. Van Duyne. Electromagnetic mechanism of SERS. *Topics in Applied Physics*, 103:19–46, 2006. Cited on page 16.

[28] Milton Kerker, O Siiman, L A Bumm, and D S Wang. Surface enhanced Raman scattering (SERS) of citrate ion adsorbed on colloidal silver. *Appl. Opt*, 19(19):3253–3255, 1980. Cited on page 16.

[29] D. S. Wang and M. Kerker. Enhanced Raman scattering by molecules adsorbed at the surface of colloidal spheroids. *Physical Review B*, 24(4):1777–1790, 1981. Not cited.

[30] Ellen J. Zeman and George C. Schatz. An accurate electromagnetic theory study of surface enhancement factors for silver, gold, copper, lithium, sodium, aluminum, gallium, indium, zinc, and cadmium. *The Journal of Physical Chemistry*, 91(3):634–643, jan 1987. Cited on page 16.

[31] Hongxing Xu, Javier Aizpurua, Mikael Käll, and Peter Apell. Electromagnetic contributions to single-molecule sensitivity in surface-enhanced Raman scattering. *Physical Review E - Statistical Physics, Plasmas, Fluids, and Related Interdisciplinary Topics*, 62(3 B):4318–4324, 2000. Cited on page 16.

[32] Linda S Jung, Charles T Campbell, Timothy M Chinowsky, Mimi N. Mar, and Sinclair S Yee. Quantitative Interpretation of the Response of Surface Plasmon Resonance Sensors to Adsorbed Films. *Langmuir*, 14(19):5636–5648, sep 1998. Cited on page 17.

[33] Amanda J Haes and Richard P Van Duyne. A Nanoscale Optical Biosensor: Sensitivity and Selectivity of an Approach Based on the Localized Surface Plasmon Resonance Spectroscopy of Triangular Silver Nanoparticles. *Journal of the American Chemical Society*, 124(35):10596–10604, sep 2002. Cited on page 17.

[34] Alexandre Dmitriev. *Nanoplasmonic Sensors*. Springer New York, New York, NY, 2012. Cited on page 18.

[35] Björn M Reinhard, Sassan Sheikholeslami, Alexander Mastroianni, a Paul Alivisatos, and Jan Liphardt. Use of plasmon coupling to reveal the dynamics of DNA bending and cleavage by single EcoRV restriction enzymes. *Proceedings of the National Academy of Sciences*, 104(8):2667–2672, feb 2007. Cited on page 19.

[36] Carsten Sönnichsen, Björn M. Reinhard, Jan Liphardt, and A. Paul Alivisatos. A molecular ruler based on plasmon coupling of single gold and silver nanoparticles. *Nature Biotechnology*, 23(6):741–745, jun 2005. Cited on page 19.

[37] Jing Zhao, Jon a Dieringer, Xiaoyu Zhang, George C Schatz, and Richard P Van Duyne. Wavelength-Scanned Surface-Enhanced Resonance Raman Excitation Spectroscopy. *The Journal of Physical Chemistry C*, 112(49):19302–19310, dec 2008. Cited on page 19.

[38] Alexandre Dmitriev, Carl Hägglund, Si Chen, Hans Fredriksson, Tavakol Pakizeh, Mikael Käll, and Duncan S. Sutherland. Enhanced nanoplasmonic optical sensors with reduced substrate effect. *Nano Letters*, 8(11):3893–3898, 2008. Cited on page 21.

[39] Yang Shen, Jianhua Zhou, Tianran Liu, Yuting Tao, Ruibin Jiang, Mingxuan Liu, Guohui Xiao, Jinhao Zhu, Zhang-Kai Zhou, Xuehua Wang, Chongjun Jin, and Jianfang Wang. Plasmonic gold mushroom arrays with refractive index sensing figures of merit approaching the theoretical limit. *Nature communications*, 4:2381, 2013. Cited on pages 21, 22.

[40] Nahla A. Hatab, Chun Hway Hsueh, Abigail L. Gaddis, Scott T. Retterer, Jia Han Li, Gyula Eres, Zhenyu Zhang, and Baohua Gu. Free-standing optical gold bowtie nanoantenna with variable gap size for enhanced Raman spectroscopy. *Nano Letters*, 10(12):4952–4955, 2010. Cited on pages 21, 22.

[41] Lisa A. Dick, Adam D. McFarland, Christy L. Haynes, and Richard P. Van Duyne. Metal film over nanosphere (MFON) electrodes for surface-enhanced Raman spectroscopy (SERS): Improvements in surface nanostructure stability and suppression of irreversible loss. *Journal of Physical Chemistry B*, 106(4):853–860, 2002. Cited on page 22.

[42] Traci R Jensen, Michelle Duval Malinsky, Christy L Haynes, and Richard P Van Duyne. Nanosphere lithography: tunable localized surface plasmon resonance spectra of silver nanoparticles. *Journal of Physical Chemistry B*, 104(45):10549–10556, 2000. Cited on page 22.

[43] M. Kahl, E. Voges, S. Kostrewa, C. Viets, and W. Hill. Periodically structured metallic substrates for SERS. *Sensors and Actuators B: Chemical*, 51(1-3):285–291, 1998. Cited on page 22.

[44] Catalina David, Nicolas Guillot, Hong Shen, Timothée Toury, and Marc Lamy De La Chapelle. A highly reproducible SERS detection of biomolecules using lithographied nanoparticles: Application to biosensor. *AIP Conference Proceedings*, 1267:938–939, 2010. Cited on page 22.

[45] Jake Fontana, John Livenere, Francisco J. Bezares, Joshua D. Caldwell, Ronald Rendell, and Banahalli R. Ratna. Large surface-enhanced Raman scattering from self-assembled gold nanosphere monolayers. *Applied Physics Letters*, 102(20), 2013. Cited on page 22.

[46] Hyungsoon Im, Kyle C. Bantz, Si Hoon Lee, Timothy W. Johnson, Christy L. Haynes, and Sang-Hyun Oh. Self-Assembled Plasmonic Nanoring Cavity Arrays for SERS and LSPR Biosensing. *Advanced Materials*, 25(19):2678–2685, may 2013. Cited on page 22.

[47] Kaiyu Wu, Tomas Rindzevicius, Michael Stenbæk Schmidt, Klaus Bo Mogensen, Sanshui Xiao, and Anja Boisen. Plasmon resonances of Ag capped Si nanopillars fabricated using mask-less lithography. *Optics Express*, 23(10):12965, 2015. Cited on pages 23, 41.

[48] Kaiyu Wu, Tomas Rindzevicius, Michael Stenbæk Schmidt, Klaus Bo Mogensen, Aron Hakonen, and Anja Boisen. Wafer-Scale Leaning Silver Nanopillars for Molecular Detection at Ultra-Low Concentrations. *The Journal of Physical Chemistry C*, 119:2053–2062, 2015. Cited on page 23.

[49] Katharina Lilienthal, Mike Stubenrauch, Michael Fischer, and Andreas Schober. Fused silica 'glass grass': fabrication and utilization. *Journal of Micromechanics and Microengineering*, 20(2):025017, feb 2010. Cited on pages 25, 26, 43.

[50] Yves Bellouard, Ali Said, Mark Dugan, and Philippe Bado. Monolithic Three-Dimensional Integration of Micro-Fluidic Channels and Optical Waveguides in Fused Silica. *MRS Proceedings*, 782:A3.2, jan 2003. Cited on page 25.

[51] Eric Hein. Lithography-free glass surface modification by self-masking during dry etching. *Journal of Nanophotonics*, 5(1):051703, 2011. Cited on pages 26, 27, 28.

[52] Xin Ye, Xiaodong Jiang, Jin Huang, Feng Geng, Laixi Sun, Xiaotao Zu, Weidong Wu, and Wanguo Zheng. Formation of broadband antireflective and superhydrophilic subwavelength structures on fused silica using one-step self-masking reactive ion etching. *Scientific Reports*, 5(April):13023, 2015. Cited on page 26.

[53] D. a. Zeze, D. C. Cox, B. L. Weiss, and S. R. P. Silva. Lithography-free high aspect ratio submicron quartz columns by reactive ion etching. *Applied Physics Letters*, 84(8):1362, 2004. Cited on pages 26, 28, 43.

[54] EzzEldin Metwalli and Carlo G. Pantano. Reactive ion etching of glasses: Composition dependence. *Nuclear Instruments and Methods in Physics Research Section B: Beam Interactions with Materials and Atoms*, 207(1):21–27, may 2003. Cited on pages 27, 28.

[55] Eric Hein, Dennis Fox, and Henning Fouckhardt. Glass surface modification by lithography-free reactive ion etching in an Ar/CF4-plasma for controlled diffuse optical scattering. *Surface and Coatings Technology*, 205:S419–S424, 2011. Cited on pages 27, 44.

[56] N. Félidj, J. Aubard, G. Lévi, J. Krenn, M. Salerno, G. Schider, B. Lamprecht, a. Leitner, and F. Aussenegg. Controlling the optical response of regular arrays of gold particles for surface-enhanced Raman scattering. *Physical Review B*, 65(7):1–9, 2002. Cited on pages 29, 49.

[57] Steven Yampolsky, Dmitry a. Fishman, Shirshendu Dey, Eero Hulkko, Mayukh Banik, Eric O. Potma, and Vartkess a. Apkarian. Seeing a single molecule vibrate through time-resolved coherent anti-Stokes Raman scattering. *Nature Photonics*, 8(8):650–656, 2014. Cited on page 29.

[58] Simone Tanzi, Peter Friis Østergaard, Marco Matteucci, Thomas Lehrmann Christiansen, Jiri Cech, Rodolphe Marie, and Rafael Taboryski. Fabrication of combined-scale nano- and microfluidic polymer systems using a multilevel dry etching, electroplating and molding process. *Journal of Micromechanics and Microengineering*, 22(11):115008, nov 2012. Cited on page 33.

[59] Bielfeldt Friedrich Bernd and Jurgen Neureuther. Screw-Type Injection-Molding Machine, 1973. Cited on page 34.

[60] Julien Giboz, Thierry Copponnex, and Patrice Mélé. Microinjection molding of thermoplastic polymers: a review. *J. Micromech. Microeng. J. Micromech. Microeng*, 17(17):96–109, 2007. Cited on page 34.

[61] Nan Zhang, Cormac J. Byrne, David J. Browne, and Michael D. Gilchrist. Towards nano-injection molding. *Materials Today*, 15(5):216–221, 2012. Cited on page 34.

[62] C K Huang. Polymeric nanofeatures of 100 nm using injection moulding for replication. *Journal of Micromechanics and Microengineering*, 17(8):1518–1526, aug 2007. Cited on page 34.

[63] Maria Matschuk and Niels B Larsen. Injection molding of high aspect ratio sub-100 nm nanostructures. *Journal of Micromechanics and Microengineering*, 23(2):025003, feb 2013. Cited on page 35.

[64] P Utko, F Persson, A Kristensen, and N B Larsen. Injection molded nanofluidic chips: fabrication method and functional tests using single-molecule DNA experiments. *Lab Chip*, 11(2):303–308, 2011. Cited on page 37.

[65] Chizuko M Dutta, Tamer a Ali, Daniel W Brandl, Tae-Ho Park, and Peter Nordlander. Plasmonic properties of a metallic torus. *The Journal of chemical physics*, 129(8):084706, 2008. Cited on page 44.

[66] Feng Hao, Peter Nordlander, Mathew T. Burnett, and Stefan A. Maier. Enhanced tunability and linewidth sharpening of plasmon resonances in hybridized metallic ring/disk nanocavities. *Physical Review B*, 76(24):245417, 2007. Cited on page 44.

Chapter 11

P1: Glass Nanopillars for SERS and Electrochemistry

Lithography-free Gold Capped Fused Silica Nanopillars for Electrochemistry and Surface Enhanced Raman Spectroscopy

Anil Haraksingh Thilsted, Kuldeep Sanger, Onur Durucan, Tomas Rindzevicius, Michael Stenbæk Schmidt, Kinga Zór, and Anja Boisen*
Department of Micro- and Nanotechnology
Technical University of Denmark
2800 Kgs Lyngby, Denmark
(Dated: November 11, 2016)

Electrochemistry (EC) and surface enhanced Raman spectroscopy (SERS) measurements, using a substrate of Au-capped fused silica nanopillars were used to achieve low concentration analyte detection and quantification. A lithography-free reactive ion etching (RIE) fabrication process resulted in a dense cluster of high aspect ratio fused silica nanopillars over wafer-scale areas. A subsequent gold e-beam deposition resulted in isolated caps that supported plasmon resonances for surface enhanced Raman spectroscopy (SERS). The gold layer also served as a conducting layer. A triple electrode design was achieved by depositing gold in selected areas only. The high surface area of the gold layer on the nanostructures as well as the high density of plasmon hot spots allowed for highly sensitive SERS detection with a relative standard deviation of 13.4% of the Raman signal and an EC sensitivity 31 times higher than commercially available electrodes. Detection of paracetemol at low concentrations was demonstrated as a proof-of-concept of the sensing device for both EC and SERS.

I. INTRODUCTION

Surface enhanced Raman scattering (SERS) and electrochemistry have been historically linked since the discovery of the Raman enhancement phenomenon. Spectro-electrochemists utilize vibrational spectroscopy such as Raman spectroscopy to record a 'fingerprint' of interactions occuring at the electrode-electrolyte interface [1]. It was discovered that a nanostructured electrode surface, typically achieved via electrochemical roughening, introduced plasmonic hot spots that enhanced the Raman signal many orders of magnitude[2, 3]. This combination of using SERS with electrochemical processes (EC-SERS) has led to extensive research on a large range of areas, including corrosion and surface science[4], fuel cells, electrocatalysis and surface redox reactions[5, 6], and adsorption and reaction of biomolecules[7–9].

There are a number of significant advantages when using the two techniques simultaneously. These include using SERS for monitoring electrochemical reactions at ultra-low concentrations and using an applied potential to promote adhesion of the target molecule to the gold layer to increase the likelihood of adsorption to plasmonic hot spots for detection[10, 11]. A more advanced technique involves using fluctuation of the applied electrode potential to adsorb and desorb different sets of molecules while monitoring the Raman signature and thereby avoid spectral congestion. This is especially relevant with coadsorption of molecules in complex solutions, as is typically the case with biological solutions[9].

While electrochemically roughened metal surfaces increase the Raman signal orders of magnitude, the substrates suffer from irreproducability with ill-defined nanoscale geometry[12]. Recent developments in nanofabrication techniques have allowed for the control of the size and shape of metal nanostructures that have advanced the understanding and control of localized surface plasmon resonance (LSPR), the enhancement and thus the applications for SERS sensing [13]. These advances have transitioned SERS from a supplemental technique for electrochemical studies to a robust analytical technique for use in biomedical diagnostics, environmental sensing, food safety and drug enforcement [14–16].

Several methods for achieving well-defined metal nanostructures for SERS have been developed, including chemical synthesis of large quantities of metal nanoparticles. However, a greater control of the plasmonic enhancement has been achieved, using lithographic techniques including electron beam [17], nanosphere [18] and nanoimprint lithography [19]. While these techniques have achieved impressive results, they require advanced, time consuming and costly processes. In contrast, lithography-free reactive ion etching (RIE) is a fast and straightforward technique to achieve a dense cluster of high aspect ratio nanopillars over large areas [20, 21]. Recent developments have shown that lithography-free nanostructuring of other materials such as glass is possible. Hein et al. and Zeze et al. have shown that a seed layer such as aluminum can form local nanomasks with lower etch rates during the etching process, thus leading to nanostructures in fused silica [22, 23]. Using fused silica substrate instead of doped silicon provides an insulating and chemically resistant material upon which SERS and electrochemistry can be carried out.

RIE, with a subsequent metal evaporation, achieves a dense cluster of suspended metal caps that serve as a high enhancement and homogeneous SERS platform that is reproducible, high throughput and low cost [24, 25].

* Email: anja.boisen@nanotech.dtu.dk

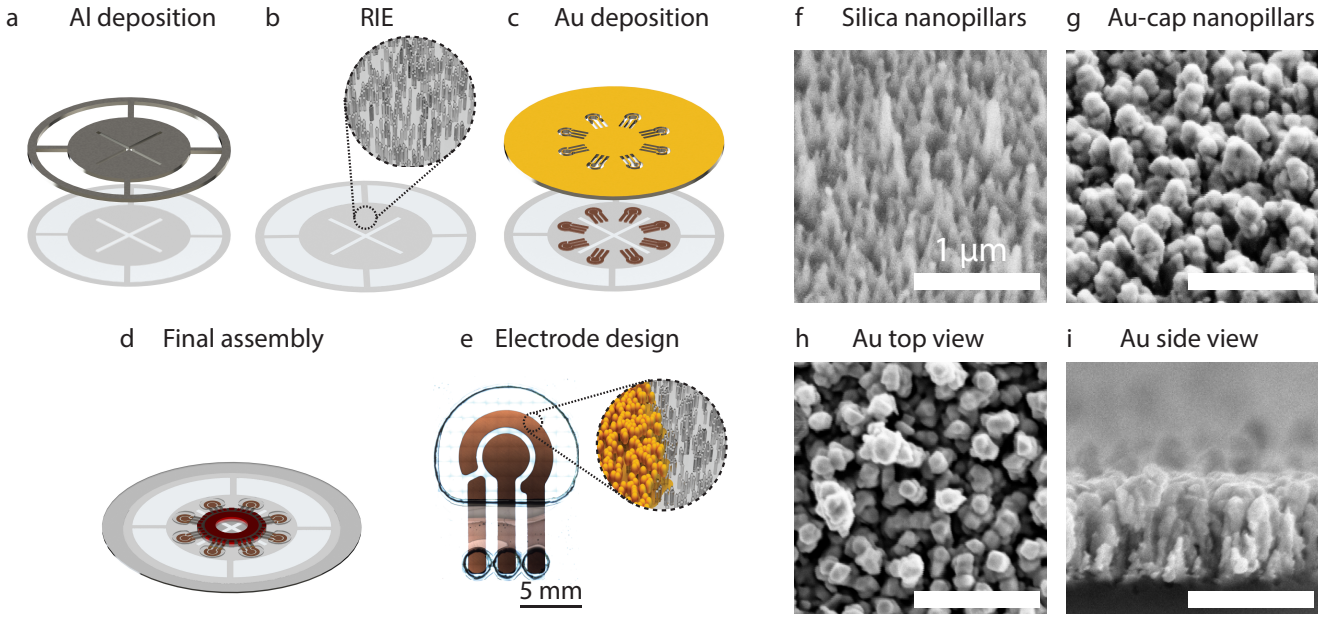

FIG. 1. Illustration of the fabrication process for gold capped glass nanopillars, using RIE and shadowmasks. (a) An aluminum layer and (b) RIE resulted in fused silica nanopillars. (c) Electrodes were achieved using gold deposition through a shadowmask. (d) Liquid containment wells were achieved using an attached polymer layer. (e) A photograph of a set of nanostructu red electrodes. (f) SEM images of fused silica nanopillars and (g) with an evaporated gold layer, shown from (h) the top view and (i) the side view. All SEM images have the same scale.

Extensive research has also been carrried out on using nanostructures for electrodes due to their unique electronic, chemical and catalytic properties because of their large specific surface area. This has greatly extended the electrochemical sensing performance [26] and have resulted in nanoporous metal structures, nanoparticles[27], and especially nanotubes[28] and nanowires[29] that have shown promise as ultra-sensitive electrochemical sensors. Fabrication techniques have typically involved chemical synthesis [30] and electrodeposition, sometimes in combination with microfabrication lithographic techniques [31]. Vertically aligned nanopillars, achieved by physical vapour or chemical vapour deposition, also show significantly enhanced electrochemical sensing performance [32, 33].

In this paper, we report on RIE on fused silica to achieve nanopillar arrays that were used as the underlying structure for a deposited gold layer that served both as a homogeneous SERS platform as well as a highly sensitive electrochemical sensor, thus allowing for both EC and SERS measurements. The process utilized a high throughput, low cost, lithography-free fabrication to achieve nanostructured electrodes. These electrodes featured a high specific surface area to increase the electrochemical sensing sensitivity as well as isolated gold caps on the tips of the nanopillars that resulted in a high density of plasmonic hotspots for SERS detection of analytes at low concentrations.

II. RESULTS AND DISCUSSION

Fused silica nanopillars with gold caps were achieved using RIE. A seed layer of aluminum was used to sputter nanoscale masks that resulted in nanostructures. An aluminum pattern was achieved by e-beam evaporation through a shadowmask with a design consisting of an outer ring to allow electrostatic clamping during etching, shown in Figure 1a. The design also featured a center cross that ensured reduction of the maximum distance of the exposed fused silica wafer to areas with aluminum so that sputtering occured evenly across the wafer. This ensured that the density of the nanopillars was homogeneous. The morphology of the nanopillars was dependent on the flow of the gases, the pressure in the chamber, the etching time, platen and coil power, the chuck temperature as well as the etching time. The parameters used to achieve dense, high-aspect ratio and homogeneous nanopillars, given in Table I.

SF_6 flow	170 sccm
O_2 flow	70 sccm
Pressure	75 mTorr
Platen power	110 W
Coil power	450 W
Chuck temperature	5°C
Etch time	4 min

TABLE I. Etching parameters

The gold layer was achieved using e-beam evaporation through an additional shadowmask, resulting in isolated metal caps and defined the working, counter and reference electrode. SEM images of the gold capped fused silica nanopillars are shown in Figure 1g. The design of the electrodes, shown in Figure 1b was modelled after commercially available screen-printed carbon electrodes[34]. A patterned poly(methyl methacrylate) (PMMA) layer was adhered to the fused silica wafer to define small wells over the sites of each electrode set. These wells were used to contain analyte liquid and prevent cross-contamination between the sensor areas. Simultaneous electrical connections to all eight sets of electrodes were achieved using spring-loaded pogo pins on a plastic mount. The final assembly is illustrated in Figure 1d.

SERS performance of the gold capped nanopillars was evaluated using trans-l,2-bis(4-pyridyl)ethylene (BPE) dissolved in ethanol. To map the SERS active regions, a 1 mM concentration was used and 5 μL was evenly deposited on the electrodes. The distribution of the Raman intensity is plotted in Figure 2. BPE at a concentration of 100 μM was used to demonstrate low concentration measurements. Raman measurements were carried out from both the front of the substrate and through the backside, as shown in Figure 2b. Backside measurements showed a 37% relative Raman signal compared to those from the front. Raman background measurements were carried out using pure ethanol. These measurements showed a strong enhancement with minimal background signal and the ability to measure from the backside. Furthermore, they showed a homogeneous signal enhancement with a relative standard deviation of 13.4%, as shown in Figure Ib.

EC performance was evaluated by cyclic voltammograms of ferrocyanide/ferricyanide 10 mM dissolved in a phosphate buffer solution (PBS) of pH 7.0. The data showed a reversible electrochemical response with a separation of the oxidation peak potential and reduction peak potential, ΔE_p, of 99 mV at 50 mV s^{-1}, as shown in Figure 3.

Paracetemol was chosen as a molecule to demonstrate detection using both EC and SERS. The current peak of the EC measurements were evaluated as a function of concentration and the Raman spectrum was used to confirm the molecule identity. The concentrations used ranged from 0.063 mM to 1 mM, dissolved in 10 mM PBS. An increased current signal was observed for for higher concentrations, as shown in Figure 4a. EC performance was evaluated by comparing to commercially available electrodes. The current peak for the nanostructed substrate showed a signal amplitude of 2.60×10^{-4} A in comparison to commercially available electrodes that showed a peak of 8.29×10^{-6} A, for 1 mM paracetemol. Thus, the nanopillar electrodes showed an EC sensitivity improvement by a factor of 30. This increase in EC signal is attributed to the high surface area of the sample. The gold nanoholes at the base of each glass nanopillar as well

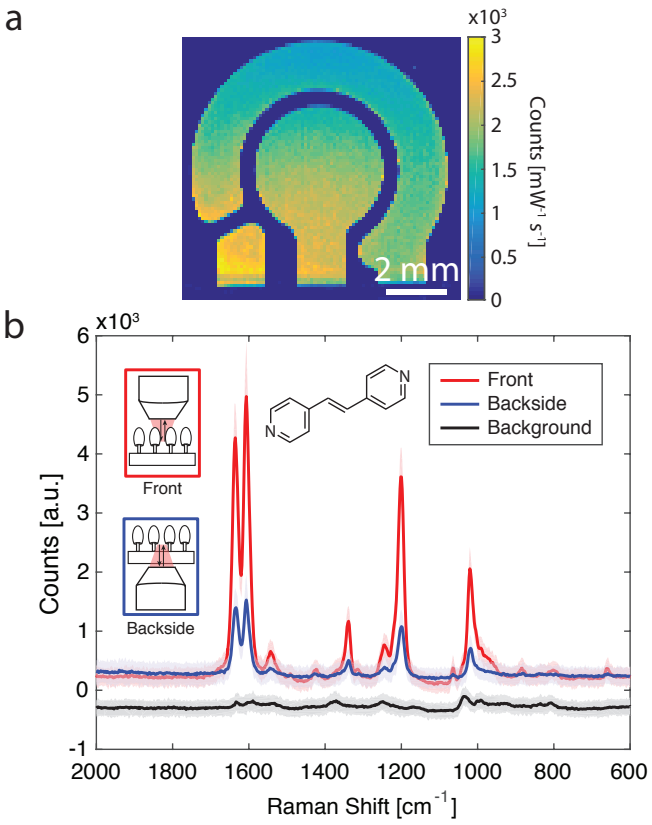

FIG. 2. Spatial distribution of the Raman signal at the 1198 cm^{-1} peak. (b) Raman spectra using a 1 μL drop of a 100 μM concentration of BPE, measured from the front and backside. Background measurements with pure ethanol are shifted down 500 counts. The relative standard deviation of the Raman signal was 13.4%. Shaded error bars show 90% confidence interval.

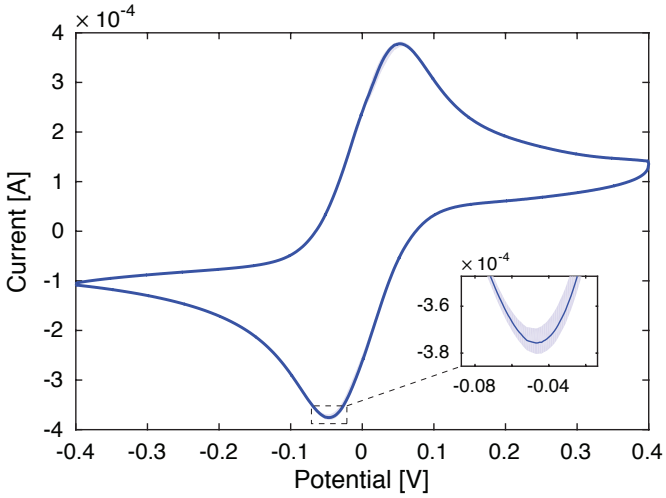

FIG. 3. Cyclic voltamogram of ferrocyanide/ferricyanide, showing a peak separation of 99 mV at 50 mVs^{-1}. The shaded error bar shows 90% confidence interval measured between the electrode sets on a wafer.

as the gold caps that are electrically connected to the planar gold areas, provide a significantly larger surface area in comparison to planar electrodes.

Raman measurements of paracetemol was carried out using a concentration of 1 mM dissolved in 1 mM PBS, as shown in Figure 4b. Despite crystallisation of the PBS salt, detecting a clear Raman fingerprint was still possible. SERS peaks showed good agreement with the Raman spectrum measured on paracetemol powder. Background measurements were also carried out on the PBS in order to ensure that the Raman peaks originated only from the paracetemol.

The EC and SERS measurements shown in Figure 4 demonstrated the use of the nanopillar electrodes for carrying out sensitive EC measurements with a much greater signal compared to commercially available microstructured electrodes. The EC measurements can be followed up with SERS in order to identify the molecule being measured.

III. CONCLUSION

A device for EC and SERS using gold capped nanopillar structures in an electrode pattern was achieved using only lithography-free etching and metal deposition through shadowmasks. This method of fabrication is straightforward, high throughput and low cost. Metallic nanostructures had a high specific surface area as well as a high density of plasmonic hot spots. These attributes resulted in a surface that featured a high SERS signal with a Raman intensity relative standard deviation of 13.4% for 100 μM BPE. Electrochemical performance showed 30 times higher signal than for commercially available electrodes. Measurements of paracetemol were carried out as a proof-of-concept for detection and identification of low concentrations.

IV. ACKNOWLEDGEMENT

This work was funded by the NAPLAS project, The Danish Council for Independent Research as well the European Research Council under the European Union's Seventh Framework Programme (FP7/2007-2013)/ERC grant agreement n^{o} 320535.

V. EXPERIMENTAL METHODS

A. Fabrication

The nanopillars were produced using 4 in double side polished fused silica wafers with a 500 μm thickness[35]. The aluminum mask was achieved using e-beam evaporation[36] through an aluminum shadowmask. The wafers were then placed in a RIE tool[37].

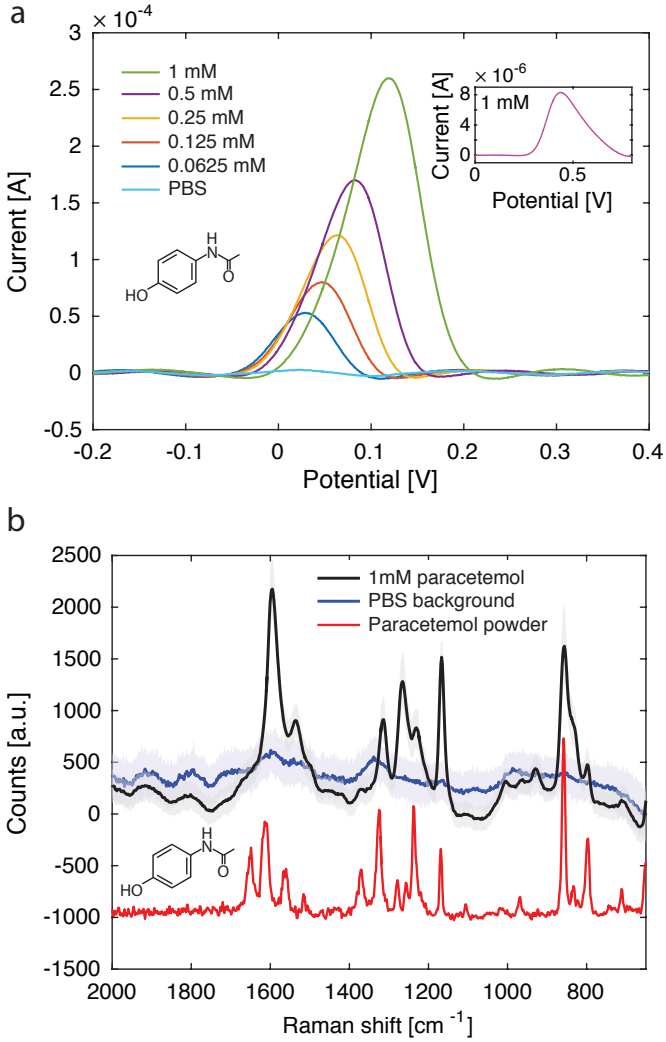

FIG. 4. (a) EC measurements of different concentrations of paracetemol, showing a peak that increased with increasing concentration. The background PBS shows no peak. The inset shows a 1 mM paracetemol measurement, using commercially available DropSens electrodes for comparison, showing a much lower signal. (b) SERS measurements of 1 mM paracetemol in 1 mM PBS solution, showing clear peaks that are correlated with Raman measurements of paracetemol powder. The background SERS signal for PBS is also shown.

The gold film was achieved using the e-beam evaporator. Nanostructures were characterized using a scanning electron microscope[38].

B. Raman characterization

Raman measurements were carried out using a Raman microscope[39] with a 780 nm laser wavelength at 5 mW power and a 0.025 s exposure time, and a 50 μm slit for the measurements shown in Figure 2b. For the mea-

surements shown in Figure 2a, no EM gain was used on the spectrometer CCD. Raman measurements shown in Figure 4b were carried out using 10 mW and a 0.1 s exposure time with EM gain. Future work should focus on optimization of the nanostructure morphology as well as the electrode design in order to increase the performance of EC and SERS.

C. Electrochemistry characterization

Electrochemistry characterization was carried out using an eight-channel potentiostat[40] connected simultaneously to the 8 electrode sets on the wafer. All electrochemical measurements were performed at room temperature. For electrode characterization cyclic voltammograms from −400 mV to 400 mV vs. gold pseudo-reference electrodes were recorded in 10 mM ferricyanide/ferrocyanide in PBS, pH7 as supporting electrolyte. Paracetamol detection was performed using square wave voltammetry (SWV) at potential range from −0.2 to 0.4 V with a step potential of 0.001 V, a square-wave frequency of 10 Hz and amplitude of 0.05 V. All the voltammograms presented were baseline-corrected to improve the visualization and identification of peaks over the baseline without introducing any artifact.

[1] Marco Musiani, Jun-Yang Liu, and Zhong-Qun Tian. Applications of Electrochemical Surface-Enhanced Raman Spectroscopy (EC-SERS). In *Developments in Electrochemistry*, volume 6, pages 137–162. John Wiley & Sons, Ltd, Chichester, UK, jun 2014.

[2] M. Fleischmann, P.J. Hendra, and A.J. McQuillan. Raman spectra of pyridine adsorbed at a silver electrode. *Chemical Physics Letters*, 26(2):163–166, may 1974.

[3] George C. Schatz, Matthew A. Young, and Richard P. Van Duyne. Electromagnetic mechanism of SERS. *Topics in Applied Physics*, 103:19–46, 2006.

[4] W B Cai, B Ren, X Q Li, C X She, F M Liu, X W Cai, and Z Q Tian. Investigation of surface-enhanced Raman scattering from platinum electrodes using a confocal Raman microscope: dependence of surface roughening pretreatment. *Surface Science*, 406(1-3):9–22, 1998.

[5] De-yin Wu, Xiu-min Liu, Sai Duan, Xin Xu, Bin Ren, Sheng-hisen Lin, Zhong-qun Tian, Interacting Copper, and Platinum Metals. Chemical Enhancement Effects in SERS Spectra : A Quantum Chemical Study of Pyridine Interacting with Copper , Silver , Gold and Platinum Metals Chemical Enhancement Effects in SERS Spectra : A Quantum Chemical Study of Pyridine. pages 4195–4204, 2008.

[6] Sungho Park, Pengxiang Yang, Piedad Corredor, and Michael J. Weaver. Transition metal-coated nanoparticle films: Vibrational characterization with surface-enhanced Raman scattering. *Journal of the American Chemical Society*, 124(11):2428–2429, 2002.

[7] Daniel H Murgida and Peter Hildebrandt. Disentangling interfacial redox processes of proteins by SERR spectroscopy. *Chemical Society reviews*, 37(5):937–945, 2008.

[8] N. Tognalli, A. Fainstein, C. Bonazzola, and E. Calvo. Resonant Raman spectroscopy of PAHOs self-assembled multilayers. *The Journal of Chemical Physics*, 120(4):1905, 2004.

[9] Emiliano Cortes, Pablo G Etchegoin, Eric C Le Ru, Alejandro Fainstein, Maria E Vela, and Roberto C Salvarezza. Electrochemical Modulation for Signal Discrimination in Surface Enhanced Raman Scattering (SERS). *Analytical Chemistry*, 82(16):6919–6925, aug 2010.

[10] Zhong-Qun Tian and Bin Ren. Adsorption and Reaction At Electrochemical Interfaces As Probed By Surface-Enhanced Raman Spectroscopy. *Annual Review of Physical Chemistry*, 55(1):197–229, 2004.

[11] Diego P. dos Santos, Gustavo F S Andrade, Marcia L A Temperini, and Alexandre G. Brolo. Electrochemical Control of the Time-Dependent Intensity Fluctuations in Surface-Enhanced Raman Scattering (SERS). *The Journal of Physical Chemistry C*, 113(41):17737–17744, oct 2009.

[12] Paul L. Stiles, Jon A. Dieringer, Nilam C. Shah, and Richard P. Van Duyne. Surface-Enhanced Raman Spectroscopy. *Annual Review of Analytical Chemistry*, 1(1):601–626, jul 2008.

[13] Katherine A Willets and R P Van Duyne. Localized surface plasmon resonance spectroscopy and sensing. *Annu. Rev. Phys. Chem.*, 58:267–297, 2007.

[14] Graeme McNay, David Eustace, W. Ewen Smith, Karen Faulds, and Duncan Graham. Surface-enhanced Raman scattering (SERS) and surface-enhanced resonance raman scattering (SERRS): A review of applications. *Applied Spectroscopy*, 65(8):825–837, 2011.

[15] Bhavya Sharma, Renee R. Frontiera, Anne-Isabelle Henry, Emilie Ringe, and Richard P. Van Duyne. SERS: Materials, applications, and the future. *Materials Today*, 15(1-2):16–25, 2012.

[16] Katharina Hering, Dana Cialla, Katrin Ackermann, Thomas Dörfer, Robert Möller, Henrik Schneidewind, Roland Mattheis, Wolfgang Fritzsche, Petra Rösch, and Jürgen Popp. SERS: A versatile tool in chemical and biochemical diagnostics. *Analytical and Bioanalytical Chemistry*, 390(1):113–124, 2008.

[17] David P. Fromm, Arvind Sundaramurthy, P. James Schuck, Gordon Kino, and W. E. Moerner. Gap-Dependent Optical Coupling of Single Bowtie Nanoantennas Resonant in the Visible. *Nano Letters*, 4(5):957–961, may 2004.

[18] Erin M. Hicks, Xiaoyu Zhang, Shengli Zou, Olga Lyandres, Kenneth G. Spears, George C. Schatz, and Richard P. Van Duyne. Plasmonic properties of film over nanowell surfaces fabricated by nanosphere lithography. *Journal of Physical Chemistry B*, 109(47):22351–22358, 2005.

[19] Sisi Liu, Zhimou Xu, Tangyou Sun, Wenning Zhao, Xinghui Wu, Zhichao Ma, Haifeng Xu, Jian He, and Cunhua Chen. Large-scale fabrication of polymer/Ag coreshell nanorod array as flexible SERS substrate by combining direct nanoimprint and electroless deposition. *Applied Physics A*, pages 1–6, 2013.

[20] S. H. Zaidi, D. S. Ruby, and J. M. Gee. Characterization of random reactive ion etched-textured silicon solar cells. *IEEE Transactions on Electron Devices*, 48(6):1200–1206, 2001.

[21] M. Gharghi and S. Sivoththaman. Formation of nanoscale columnar structures in silicon by a maskless reactive ion etching process. *Journal of Vacuum Science & Technology A: Vacuum, Surfaces, and Films*, 24(3):723, 2006.

[22] Eric Hein, Dennis Fox, and Henning Fouckhardt. Glass surface modification by lithography-free reactive ion etching in an Ar/CF4-plasma for controlled diffuse optical scattering. *Surface and Coatings Technology*, 205:S419–S424, 2011.

[23] D. a. Zeze, D. C. Cox, B. L. Weiss, and S. R. P. Silva. Lithography-free high aspect ratio submicron quartz columns by reactive ion etching. *Applied Physics Letters*, 84(8):1362, 2004.

[24] Michael Stenbaek Schmidt, Jörg Hübner, and Anja Boisen. Large area fabrication of leaning silicon nanopillars for surface enhanced Raman spectroscopy. *Advanced materials (Deerfield Beach, Fla.)*, 24(10):OP11–8, mar 2012.

[25] Kaiyu Wu, Tomas Rindzevicius, Michael Stenbæk Schmidt, Klaus Bo Mogensen, Aron Hakonen, and Anja Boisen. Wafer-Scale Leaning Silver Nanopillars for Molecular Detection at Ultra-Low Concentrations. *The Journal of Physical Chemistry C*, 119(4):2053–2062, 2015.

[26] Jintao Zhang and Chang Ming Li. Nanoporous metals: fabrication strategies and advanced electrochemical applications in catalysis, sensing and energy systems. *Chemical Society Reviews*, 41(21):7016, 2012.

[27] Aimin Yu, Zhijian Liang, Jinhan Cho, and Frank Caruso. Nanostructured Electrochemical Sensor Based on Dense Gold Nanoparticle Films. *Nano Letters*, 3(9):1203–1207, sep 2003.

[28] A. J. Saleh Ahammad, JaeJoon; Lee, and Md. Aminur Rahman. Electrochemical Sensors Based on Carbon Nanotubes. *Sensors*, 9(4):2289–2319, mar 2009.

[29] Umasankar Yogeswaran and Shen-Ming Chen. A Review on the Electrochemical Sensors and Biosensors Composed of Nanowires as Sensing Material. *Sensors*, 8(1):290–313, jan 2008.

[30] Nicolae Leopold and Bernhard Lendl. A New Method for Fast Preparation of Highly Surface-Enhanced Raman Scattering (SERS) Active Silver Colloids at Room Temperature by Reduction of Silver Nitrate with Hydroxylamine Hydrochloride. *The Journal of Physical Chemistry B*, 107(24):5723–5727, 2003.

[31] Leyla Soleymani, Zhichao Fang, Xuping Sun, Hong Yang, Bradford J. Taft, Edward H. Sargent, and Shana O. Kelley. Nanostructuring of Patterned Microelectrodes To Enhance the Sensitivity of Electrochemical Nucleic Acids Detection. *Angewandte Chemie International Edition*, 48(45):8457–8460, oct 2009.

[32] Chunmee Shin, Woonsup Shin, and Hun-Gi Hong. Electrochemical fabrication and electrocatalytic characteristics studies of gold nanopillar array electrode (AuNPE) for development of a novel electrochemical sensor. *Electrochimica Acta*, 53(2):720–728, dec 2007.

[33] Venkataramani Anandan, Yeswanth L. Rao, and Guigen Zhang. Nanopillar array structures for enhancing biosensing performance. *International Journal of Nanomedicine*, 1(1):73–80, jan 2006.

[34] DropSens, DRP-110.

[35] Innergie Technologies, Inc.

[36] Alcatel SCM 600 E-beam and sputtering deposition system.

[37] Advanced Oxide Etcher: STS MESC Multiplex ICP.

[38] Zeiss Supra VP 40 SEM.

[39] DXRxi Raman Imaging microscope, Thermo Scientific.

[40] Model 1000C Multi Potentiostat, CH Instruments Inc.

Chapter 12

P2: Polymer Injection SERS substrates

High Throughput Gold Coated Polymer Injected Nanopillars for Surface Enhanced Raman Spectroscopy

Anil Haraksingh Thilsted, Marco Matteuci, Marlitt Viehrig,
Darmin Çatak, Michael Stenbæk Schmidt, and Anja Boisen*
Department of Micro- and Nanotechnology
The Technical University of Denmark
2800 Kgs Lyngby, Denmark
(Dated: November 11, 2016)

Metal coated nanostructured surfaces have shown promise as substrates for surface enhanced Raman spectroscopy (SERS) and therefore allow molecular detection of trace chemicals. A dense cluster of high aspect ratio nanopillars was achieved over a large area using high throughput polymer injection moulding. The utilized mold nanopillar structure was fabricated using lithography-free reactive ion etching (RIE) to create nanopillars in silicon over wafer-scale areas. These nanopillars were replicated in a cyclic olefin copolymer (COC). Gold evaporation on the polymeric nanopillars resulted in closely spaced gold caps in which plasmonic hot spots gave rise to a large SERS signal, with a relative standard deviation of 14.6% for the Raman signal measured on a 2×10 mm area. Polymer injection of nanopillars was suitable for mass production of reproducible SERS substrates and compatible with injection moulded fluidic channels for *in situ* integration of SERS measurements in fluidic applications.

I. INTRODUCTION

Surface enhanced Raman spectroscopy (SERS) has become a powerful analysis technique to identify molecules at low concentrations, using a spectral fingerpint. SERS utilizes the optical properties of metal nanostructures in which the electromagnetic field is greatly enhanced by plasmon excitation trough a laser [1]. If molecules bind to the nanostructured metal surface at the site of this enhanced electromagnetic field, the Raman signal is greatly enhanced, often many orders of magnitude [2]. This dramatic increase in signal allows for detection of very low concentrations of analyte. Miniaturization and recently decreasing prices of laser systems and spectrometers have made this analysis method increasingly accessible. For these reasons, SERS has seen extensive use in the areas of chemical and biochemical sensing including biomedical diagnostics and environmental analysis[3, 4].

Recent research has focused on producing substrates with plasmonic structures that maximise Raman enhancement factors, reproducibility and ease of fabrication[5]. Developments in micro- and nanofabrication techniques have resulted in increasingly sophisticated high performance SERS substrates manufactured using standard top-down lithographic fabrication methods, such as electron beam [6, 7] and nanosphere lithography[8]. These fabrication methods are neither straightforward nor cost-effective for batch production of substrates with plasmonic enhancement over large areas needed for large-scale implementation of SERS as an analysis tool. Nanoimprinting has sought to address these shortcomings by creating a nanostructured master that can be replicated repeatedly at low cost [9].

* Email: anja.boisen@nanotech.dtu.dk

Previous work has shown that maskless reactive ion etching (RIE) of silicon wafers produced a dense cluster of nanopillars which, after a subsequent gold evaporation, resulted in isolated gold caps suitable for SERS [10, 11]. These substrates demonstrated that nanopillars achieved via a lithography-free method yielded highly sensitive and reproducible large-area plasmonic surfaces in a scalable and cost-effective fashion.

Advancements in injection moulding has shown that nanostructures can be replicated using high throughput methods. In injection moulding typically thermoplastic polymer is used, that is pre-heated above the glass transition temperature and subsequently injected into a nanostructured mould cavity. For demoulding, the temperature is lowered below the glass transition temperature. The process cycle time ranges typically below 5 min per replication, with unsupervised operation. For these reasons, it outperforms nanoimprint lithography in throughput and cost-effectiveness and therefore, has widespread industry adoption such as CD/DVD mass production [12]. Nanoinjection moulding has been used for antireflective[13] and superhydrophobic surfaces [14] and has shown great promise in fabrication of micro- and nanofluidic devices for handling of biological samples [15]. For example, injection moulded nanofluidic networks bonded to injection moulded interconnects for macrofluidic lines were used for handling single DNA molecules [16]. Additionally, by carefully tuning the injection moulding parameters, challenging high aspect ratio nanostructures can be achieved [17]. At nanoscales, < 100 nm nanopillars with an aspect ratio of > 2.5 was achieved by Matschuk et al. [18].

In this paper, we report a process to produce highly sensitive and reproducible SERS active substrates via high throughput and low cost injection moulding. A maskless etch was used to achieve a large area of high aspect ratio silicon nanopillars. The nanopillar shape

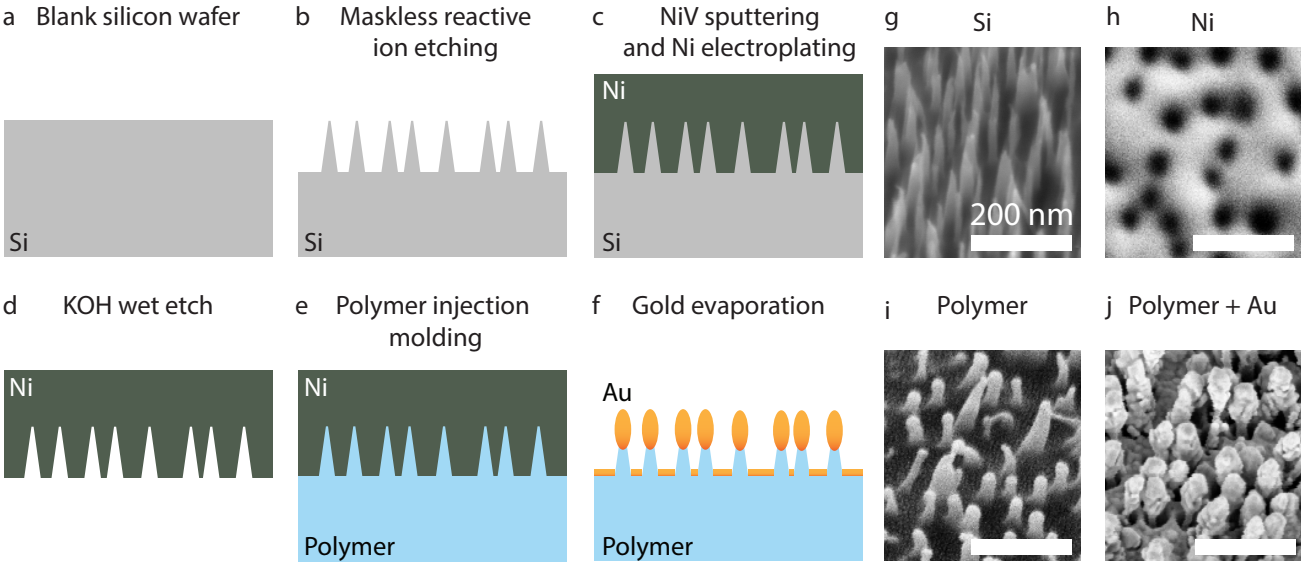

FIG. 1. Illustration of the fabrication process of polymer injected nanopillars for SERS. (a) A blank silicon wafer was used for (b) a maskless reactive ion etching that formed a dense cluster of nanopillars. (c) NiV sputtering and electroplating resulted in a master of the silicon nanopillars. (d) A KOH etch removed the silicon wafer, leaving the Ni mould behind. (e) The nanopillars were replicated in polymer using injection moulding. (d) A gold evaporation resulted in a gold layer with isolated nanocaps at the tips of the nanopillars. (g) SEM image of the silicon nanopillars and (h) SEM image of the holes in the Ni mould. (i) Polymer nanopillars after injection moulding. (j) Gold tipped nanopillars after 190 nm of gold evaporation. All SEM images are taken at 30° tilt except for (h). All scale bars are 200 nm.

was inverted in a nickel shim as a master mould for polymer injection to achieve nanostructures with a height of approximately 175 nm, width of 55 nm and an aspect ratio of 3.25. Evaporation of gold resulted in isolated metal nanocaps at the tips of the nanopillars that supported localized surface plasmon resonance. The polymer substrate allowed for bonding to a fluidic channel, thereby demonstrating a novel fully injection moulded SERS fluidic chip, suitable for low cost mass production. This straightforward integration of high throughput SERS substrates in injection moulded polymer devices opens up possibilities of utilizing a large range of microfluidic operations. These operations can facilitate SERS detection of analytes with small sample volumes, extraction of analytes from complex fluids, sequential functionalization as well as on-chip immunoassays.

II. RESULTS AND DISCUSSION

A. Fabrication

The fabrication procedure for injection moulded polymer nanopillars, replicated from a previously characterized silicon nanopillar substrate [10] is illustrated in Figure 1. A microscope slide mould was fabricated for ease of handling and mounting onto microscope stages.

Maskless RIE was carried out on a blank silicon wafer to fabricate silicon nanopillars used for the mould design. The flow of oxygen in the RIE was increased in comparison to the etching parameters used to produce nanopillars in previous work [10]. This was done to prevent overhanging of nanopillar sidewalls, resulting instead in sidewalls that sloped inwards towards the center of each nanopillar to facilitate demoulding of polymer structures, as shown in Figure 1g. An inverted nickel mould was formed from the silicon nanopillars by first sputtering 100 nm NiV, followed by Ni electroplating. The silicon wafer was removed by a potassium hydroxide (KOH) wet etch, leaving the nickel mould, shown in Figure 1h.

Replicas of the nanopillar mould in cyclic olefin copolymer (COC) were achieved, using the injection parameters listed in Table I. The polymer injection rate V_{inject} was decreased during injection. For each injection moulding cycle, a 75 × 25 mm area was nanostructured. SEM images of the polymer nanopillars are shown in Figure 1i.

T_{mould}	$155°C$
T_{melt}	$250°C$
T_{demould}	$105°C$
V_{inject}	$15 \rightarrow 4.5$ cc/s
T_{cycle}	240 s
P_{inject}	1150 bar
P_{hold}	450 kN

TABLE I. Injection moulding parameters

Subsequently, isolated gold caps at the tips of the nanopillars were achieved by a 190 nm e-beam gold evap-

oration, as shown in Figure 1j. This resulted in localized surface plasmon resonance supporting structures with high density suitable for SERS. Hundreds of microscope slide sized nanopillar areas can be produced overnight, with an unsupervised injection moulding process and be ready for gold coating once they are needed for SERS measurements. Homogeneous and large-area structuring is shown in SEM images in Figure 2a.

B. SERS characterization

A 2 × 10 mm area of the nanostructured microscope slides was evaluated for SERS performance. Trans-1,2-bis(4-pyridyl)ethylene (BPE) was used as a benchmark analyte due to its well-known spectral fingerprint. Raman measurements showed a strong signal intensity for 5 drops of 1 μL BPE deposited across the entire area at a concentration of 100 μM, as shown in Figure 2b. The background Raman signal was also measured, and while peaks from the COC were observed, they were sufficiently low to allow for distinctive measurement of low concentration analytes. Backside Raman signal strength was 82.5% lower than the measurements taken from the front. The Raman signal intensity taken from the front and standard deviation were similar to the original gold tipped silicon nanopillars [10]. Hence, the achieved injection moulded nanostructures replicated not only the morphology but also the SERS signal intensity of the original silicon nanopillars.

A concentration series using 5 drops of 1 μL BPE from 0.1 μM to 10 mM was carried out to evaluate the dosage response of the Raman signal and to determine the limit of detection. The baseline corrected height for the 1198 cm^{-1} peak is depicted as a function of concentration in Figure 3a. The Raman spectrum measured from the lowest concentration is illustrated in the inset. Characteristic BPE peaks were still visible at 0.1 μM despite the previously reported background signal originating om COC. Hence, detection of trace analyte concentrations is possible with injection moulded nanopillars. The intra-sample relative standard deviation of the Raman signal was 14.6% for 10 mM. The inter-sample relative standard deviation was 11.1% for the same concentration. Intensity maps of the Raman signal at 1018 cm^{-1} for the lowest and highest concentration of BPE are shown in Figure 3b.

C. Injection moulded fluidic SERS chip

A fully injected moulded fluidic SERS chip was achieved by injection moulding of three separate components, as illustrated in Figure 4a. It consisted of a gold coated nanopillar substrate, a fluidic channel substrate and Luer fittings as macrofluidic interconnects Ultrasonic welding during chip assembly ensured a tight seal between the components. The fluidic design for the

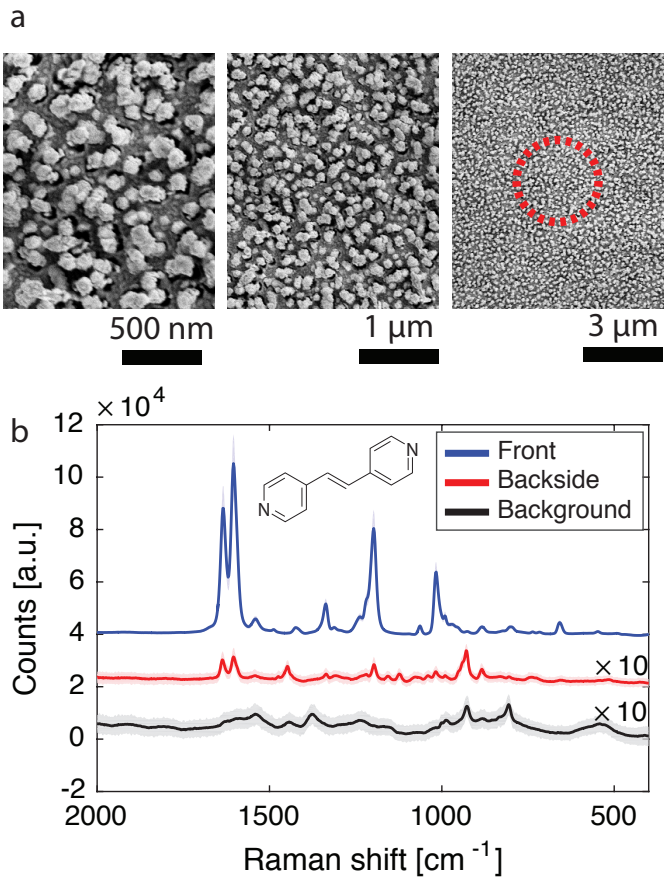

FIG. 2. (a) Top-down SEM images showing large areas of densely clustered Au-capped polymer nanopillars. (b) Raman spectrum of 5 μL BPE in ethanol at a concentration of 100 μM deposited on the Au-capped polymer nanopillars, showing a strong Raman signal. Backside measurements show a signal decrease of 82.5% compared to the frontside measurement. Background measurements, after exposure to water, showed a relatively low signal despite the polymer substrate. However, peaks originating from COC can be clearly identified. The Raman spectra have been shifted and the backside and background measurements have been multiplied by a factor of 10 for clarity. Shaded error bars are 90% confidence interval.

test structure is a H-filter, a structure typically used to extract small molecule analytes from solutions containing larger molecules [19]. *In situ.* SERS measurements were carried out by injection of pure water in the upper inlet and injection of 1 mM BPE in ethanol in the lower inlet. Both streams were run for 45 minutes. Demonstration of fluid handling is depicted using blue ink dissolved in ethanol, as shown in the photograph in Figure 4b. Measurements of BPE attached to the gold-capped polymer nanopillars were carried out *in situ* after flushing the channel with ethanol followed by water for 20 minutes. The Raman measurements for the intensity at the 1198 cm^{-1} peak are shown in Figure 4c. The dark blue areas indicate the presence of trapped air bubbles. SERS

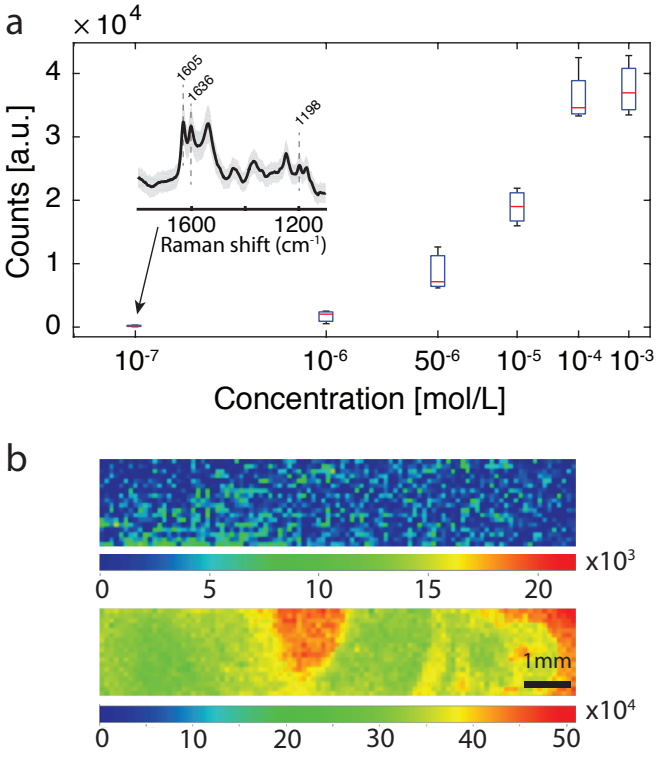

FIG. 3. (a) Raman signal plotted as a function of concentration of BPE from 0.1 μM to 10 mM. (b) Raman intensity maps over a 2×10 mm area, showing the Raman signal at the 1018 cm^{-1} peak for the lowest and highest concentrations.

measurements in a fluidic chip were thus demonstrated as a proof-of-concept.

III. CONCLUSION

Polymer injection moulding was used to replicate large areas of nanopillars and, with a subsequent metal evaporation, functioned as a highly sensitive SERS substrate with a inter-sample relative standard deviation of 11.1%. The polymer substrate allowed for a straightforward SERS integration with other injection moulded devices such as components with fluidic channels and Luer macroscale interconnects. This fabrication process can be considered as high throughput and low cost as it utilized only polymer injection and gold evaporation to achieve a SERS-active fluidic device. This platform is suitable for a wide range of biochemical analysis applications by utilizing established microfluidic operations combined with Raman spectroscopy.

IV. ACKNOWLEDGEMENT

This work was funded by the NAPLAS project, The Danish Council for Independent Research as well as the European Research Council under the European Union's Seventh Framework Programme (FP7/2007-2013) / ERC grant agreement n^o 320535.

V. EXPERIMENTAL METHODS

A. Fabrication

The silicon nanopillars were produced using 4 inch single side polished silicon wafers with 500 μm thickness that were placed in a RIE tool [20]. Polymer replicas were achieved on an industrial injection moulder [21] using TOPAS 5013L-10 COC[22].The gold film was achieved using an e-beam evaporator[23]. Nanostructures were characterized using a scanning electron microscope[24].

The substrate containing the fluidic channels was injected moulded in TOPAS 5013L-10 COC, using an aluminum shim that was milled. Likewise, the Luer fittings were also injection moulded. Ultrasonic welding for bonding the fluidic channels to the nanostructured substrate was carried out with a 350 N trigger force, 90 J energy delivered, a transducer amplitude of 50% and a 2 s holding time.

B. Raman characterization

Raman measurements were carried out using a microscope [25] with a 780 nm laser wavelength at 5 mW power and a 0.025 s exposure time for the measurements shown in Figure 1. Measurements taken for the concentration series were averaged over five measurements using an exposure time of 0.05 s. The signal was amplified using the gain function on the EMCCD.

C. Fluid channel experiments

Fluidic experiments were carried out by injecting pure water and a 1 mM BPE in ethanol solution at 100 μ L min^{-1} simultaneously into the chip, using a syringe pump [26] connected to the Luer fittings via hoses. Prior to this, pure ethanol was injected for 10 minutes to flush the chip, followed by injection of the BPE solution. After running both inlets simultaneously for 45 minutes, the BPE solution was stopped and only pure water filled the fluid channel, rinsing the substrates for 10 more minutes.

[1] Katrin Kneipp, Harald Kneipp, Irving Itzkan, Ramachandra R Dasari, and Michael S Feld. Surface-enhanced Raman scattering and biophysics. *Journal of*

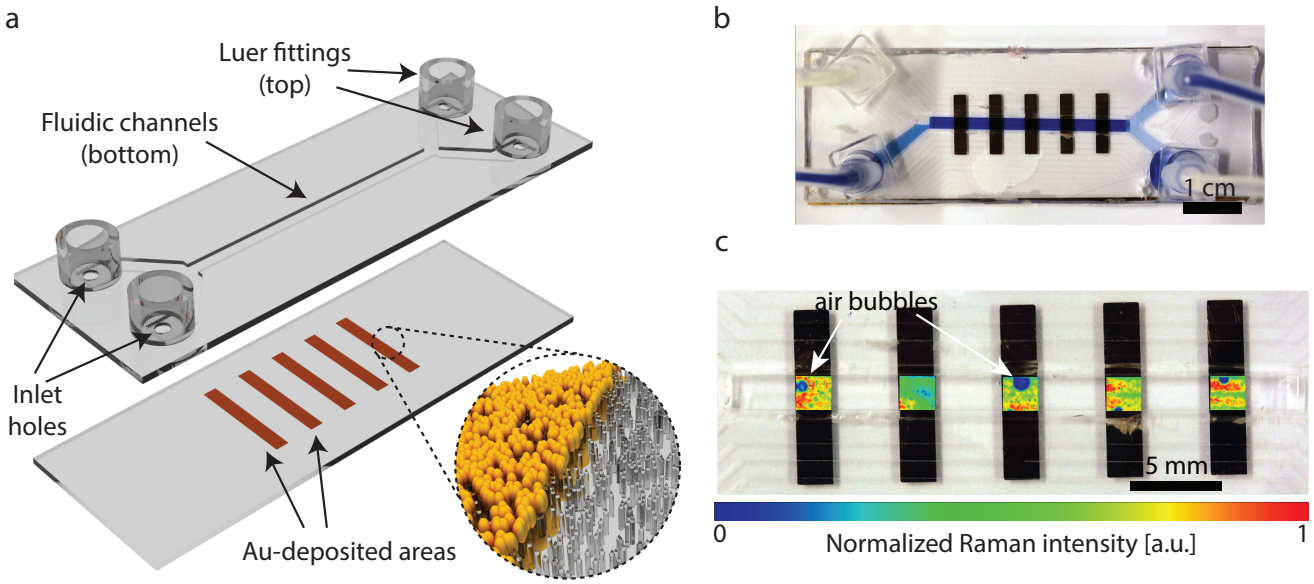

FIG. 4. (a) The components of the polymer injected fluidic SERS chip. The lid has Luer fittings ultrasonically welded to a mould that contained fluidic channels. The lower component features the gold-capped nanopillars. Gold was deposited in some areas only, using a shadowmask, to distinguish between measurement regions. (b) A photograph of fluidic channels with integrated SERS-active areas, with fluid handling demonstrated using blue ink and water. (c) Maps of the Raman measurements across each gold bar for the intensity of the 1198 cm^{-1} peak while the channel was filled with water after BPE exposure. The low Raman signals, shown as blue circles, represent trapped air bubbles in the channel. The intensity of the Raman signal was normalized for each bar in order to mitigate performance differences.

Physics: Condensed Matter, 14(18):R597–R624, 2002.

[2] George C. Schatz, Matthew A. Young, and Richard P. Van Duyne. Electromagnetic mechanism of SERS. *Topics in Applied Physics*, 103:19–46, 2006.

[3] Graeme McNay, David Eustace, W. Ewen Smith, Karen Faulds, and Duncan Graham. Surface-enhanced Raman scattering (SERS) and surface-enhanced resonance raman scattering (SERRS): A review of applications. *Applied Spectroscopy*, 65(8):825–837, 2011.

[4] Bhavya Sharma, Renee R. Frontiera, Anne-Isabelle Henry, Emilie Ringe, and Richard P. Van Duyne. SERS: Materials, applications, and the future. *Materials Today*, 15(1-2):16–25, 2012.

[5] Paul L. Stiles, Jon A. Dieringer, Nilam C. Shah, and Richard P. Van Duyne. Surface-Enhanced Raman Spectroscopy. *Annual Review of Analytical Chemistry*, 1(1):601–626, jul 2008.

[6] Nahla A. Hatab, Chun Hway Hsueh, Abigail L. Gaddis, Scott T. Retterer, Jia Han Li, Gyula Eres, Zhenyu Zhang, and Baohua Gu. Free-standing optical gold bowtie nanoantenna with variable gap size for enhanced Raman spectroscopy. *Nano Letters*, 10(12):4952–4955, 2010.

[7] David P. Fromm, Arvind Sundaramurthy, P. James Schuck, Gordon Kino, and W. E. Moerner. Gap-Dependent Optical Coupling of Single Bowtie Nanoantennas Resonant in the Visible. *Nano Letters*, 4(5):957–961, may 2004.

[8] Lisa A. Dick, Adam D. McFarland, Christy L. Haynes, and Richard P. Van Duyne. Metal film over nanosphere (MFON) electrodes for surface-enhanced Raman spectroscopy (SERS): Improvements in surface nanostructure stability and suppression of irreversible loss. *Journal of Physical Chemistry B*, 106(4):853–860, 2002.

[9] Wei Wu, Min Hu, Fung Suong Ou, Zhiyong Li, and R Stanley Williams. Cones fabricated by 3D nanoimprint lithography for highly sensitive surface enhanced Raman spectroscopy. *Nanotechnology*, 21(25):255502/1–255502/6, 4suppl., 2010.

[10] Michael Stenbaek Schmidt, Jörg Hübner, and Anja Boisen. Large area fabrication of leaning silicon nanopillars for surface enhanced Raman spectroscopy. *Advanced materials (Deerfield Beach, Fla.)*, 24(10):OP11–8, mar 2012.

[11] Kaiyu Wu, Tomas Rindzevicius, Michael Stenbæk Schmidt, Klaus Bo Mogensen, Aron Hakonen, and Anja Boisen. Wafer-Scale Leaning Silver Nanopillars for Molecular Detection at Ultra-Low Concentrations. *The Journal of Physical Chemistry C*, 119(4):2053–2062, 2015.

[12] Nan Zhang, Cormac J. Byrne, David J. Browne, and Michael D. Gilchrist. Towards nano-injection molding. *Materials Today*, 15(5):216–221, 2012.

[13] Alexander B. Christiansen, Jeppe S. Clausen, N. Asger Mortensen, and Anders Kristensen. Injection moulding antireflective nanostructures. *Microelectronic Engineering*, 121:47–50, 2014.

[14] Seung-Mo Lee and Tai Hun Kwon. Mass-producible replication of highly hydrophobic surfaces from plant leaves. *Nanotechnology*, 17(13):3189–3196, 2006.

[15] Kasper Kistrup, Carl Esben Poulsen, Peter Friis Østergaard, Kenneth Brian Haugshøj, Rafael Taboryski, An-

ders Wolff, and Mikkel Fougt Hansen. Fabrication and modelling of injection moulded all-polymer capillary microvalves for passive microfluidic control. *Journal of Micromechanics and Microengineering*, 24(12):125007, 2014.

[16] P Utko, F Persson, A Kristensen, and N B Larsen. Injection molded nanofluidic chips: fabrication method and functional tests using single-molecule DNA experiments. *Lab Chip*, 11(2):303–308, 2011.

[17] Shuntaro Hattori, Keisuke Nagato, Tetsuya Hamaguchi, and Masayuki Nakao. Rapid injection molding of high-aspect-ratio nanostructures. *Microelectronic Engineering*, 87(5-8):1546–1549, 2010.

[18] Maria Matschuk and Niels B Larsen. Injection molding of high aspect ratio sub-100 nm nanostructures. *Journal of Micromechanics and Microengineering*, 23(2):025003, feb 2013.

[19] Jennifer L. Osborn, Barry Lutz, Elain Fu, Peter Kauffman, Dean Y. Stevens, and Paul Yager. Microfluidics without pumps: reinventing the T-sensor and H-filter in paper networks. *Lab on a Chip*, 10(20):2659, 2010.

[20] Advanced Silicon Etcher (STS MESC Multiplex ICP).

[21] Engel Victory 80/45 Tech with an ERC 13/1-F robot, Austria.

[22] TOPAS Advanced Polymers Germany.

[23] Alcatel SCM 600 E-beam and sputtering deposition system.

[24] Zeiss Supra VP 40 SEM.

[25] Thermo Scientific DXRxi, Thermo Scientific.

[26] PH 2000 Programmable, Harvard Apparatus.

Chapter 13

P3: Flexible and Transparent SERS substrates

Large-area, Lithography-free Fabrication of Transparent and Flexible Substrates for Surface-enhanced Raman Spectroscopy

Anil Haraksingh Thilsted, Tomas Rindzevicius, Kaiyu Wu,
Giuseppe Saccone, Michael Stenbæk Schmidt, and Anja Boisen*
Department of Micro- and Nanotechnology
The Technical University of Denmark
2800 Kgs Lyngby, Denmark
(Dated: November 9, 2016)

Techniques that allow integration of SERS substrates into microfluidic devices are becoming increasingly relevant. Development of SERS applications often requires *in situ* sample preparation and liquid manipulation, e.g. for performing intracellular SERS studies. We present a simple and cheap approach for fabricating transparent and flexible SERS surfaces on a 4 inch polymethylmethacrylate (PMMA) foil using a simple, maskless fabrication process. The technique is based on (i) fabricating gold or silver-capped nanopillar (NP) structures on a 4 inch silicon wafer using a maskless lithography process, and then (ii) transfer of Ag or Au metal caps from NPs onto a PMMA foil using a simple nanoimprint process. The fabricated plasmonic nanostructures can be characterized as Ag or Au nanoolive structures that are partially embedded into a PMMA foil. These nanoolive particles support localized surface plasmon reasonances (LSPRs) that are located in the visible spectral region. The measured optical properties agree well with the theoretical simulations based on a 3D finite element method. Both theory and experimental data indicate that Ag nanoolive structures support two pronounced LSPR modes: a standard dipolar or particle mode and a cavity resonance mode. In the case of Au nanoolive structures only one prominent, the particle LSPR mode is observed. The performance of the Au structures were tested and it was shown that Au nanoolives can be used for both LSPR-based chemo-sensing and SERS-based molecular detection. The estimated SERS enhancement factor of the Au nanoolive structures is $\sim 8.0 \times 10^6$.

I. INTRODUCTION

Over the last two decades, surface-enhanced Raman scattering (SERS) spectroscopy has been established as a key analytical tool [1, 2] that enables detection of target molecules to the single molecule level [3, 4]. SERS is a surface-induced effect that tremendously enhances Raman scattering signal thereby, allowing the detection of low concentrations of analytes, see e.g. an excellent review of early SERS works by Moskovits [5]. It is generally agreed that there are two distinct contributions to the surface-enhancement effect: the so-called chemical and electromagnetic (EM) enhancement mechanisms [6]. The EM enhancement is the dominant part caused by localized surface plasmon resonances (LSPRs) that confine the incident field at the metal surface and generate the EM hot spots that are essential for SERS [7]. This phenomenon has already demonstrated its usefulness in a number of applications within biomedical diagnostics [8], environmental sensing [9], food safety [10], forensic science [11] and drug enforcement [12]. Furthermore, development of hand-held SERS-based sensors [13] is highly important e.g. for on-site detection of explosives and nerve gases [14, 15]. Miniaturized Raman spectrometers are progressively becoming better, smaller and cheaper [16], and can be integrated with high quality SERS substrates [17] and microfluidic sampling solutions [18].

Microfluidic technologies are suitable for controlled and accurate manipulation of liquids in small volumes [19, 20], which is highly relevant for SERS applications. Due to more favourable heat dissipation in a microfluidic channel, reproducibility of SERS signals can be improved [18]. By combining SERS and microfluidics into a single unit, it is possible to perform sample preparation, liquid manipulation, separation and in situ detection on one platform which is crucial e.g. for intracellular SERS studies [21]. Since most microfluidic devices are fabricated using simple molding techniques [22] and inexpensive materials such as polydimethylsiloxane (PDMS) or polymethylmethacrylate (PMMA), integration of SERS substrates into the system should also be cheap, simple and compatible with moulding fabrication processes.

Development of high performance SERS substrates is closely correlated to recent advances in top-down and bottom-up nanofabrication techniques [23, 24]. Most SERS substrate fabrication techniques, however, are not commercially feasible due to the high cost and complexity. Maskless lithography, on the other hand, is of particular interest for SERS because the process yields high quality SERS substrates at extremely low cost [25]. In comparison to standard lithography techniques, maskless reactive ion etching (RIE) process can be used to produce high aspect ratio ($\sim$1:10 and dense ($\sim$ 20 pillars /μm^2) nanopillar (NP) structures from a blank silicon (Si) wafer in a one-step process [26, 27]. A large variety of nanostructure morphologies can be achieved by carefully balancing the RIE process parameters [28–30]. SERS substrates are essentially produced using a simple, lithography-free, two-step process and display extremely

* Email: anja.boisen@nanotech.dtu.dk

high EM-field enhancement factors over a large ($> \mathrm{cm}^2$) surface area [25, 31].

Integration of SERS-active NP structures with polymeric surfaces offers distinct advantages. Firstly, transparency of the SERS-active surface in the Vis-NIR region is important for obtaining SERS signals through the back of the substrate to avoid measurement through opaque liquids or complex biological media. Secondly, possibility to perform SERS in transmission configurations opens up new signal acquisition pathways [32]. Third, polymer materials can be easily moulded into different morphologies. For example, SERS active structures can be imprinted onto a flexible contact lens for non-invasive detection of glucose levels in human tears [33]. The imprint materials can also be biocompatible and their phase transition makes them suitable for bonding to make a water tight seal in different types of microfluidic devices [17, 19]. Additionally, elastomeric polymers have been shown in previous work to be particularly useful as the underlying material for a SERS substrate as strain control have allowed for tuning of the gap distance between metal nanostructures for controlling SERS signal intensities [34, 35].

We present a fabrication technique for obtaining flexible, wafer-scale SERS substrates using a maskless, three-step process which is fully compatible with standard microfluidics molding processes and materials. The metal nanocaps were removed from the Au and Ag NP structures and transferred onto a polymer foil using a simple nanoimprint process. By optimizing the imprint process parameters, nearly all nanocaps from a 4 inch wafer can be transferred into a polymer foil which then results in relatively uniform SERS signal intensities across large surface areas (> 0.5 cm^2). Experimental extinction spectra revealed confined LSPR modes located close to $\lambda_{(\mathrm{Au,max})} \approx 550$ nm and $\lambda_{(\mathrm{Ag,max})} \approx 350, 450$ nm for gold and silver nanoolive structures, respectively. To understand the results, we employed Finite Element Modelling (FEM) simulations which agree well with the experimental data. We find that these noble metal nanoolive structures display interesting optical properties and can be utilized for both SERS and LSPR-based molecular detection.

II. EXPERIMENTAL

A. SERS Measurements

All SERS spectra were recorded using a microscope[36] equipped with a 780 nm laser. A slit size in front of the spectrograph was set to 25 μm. The SERS signal collection time was set to 1 s and averaged over three consecutive measurements. Raman spectra were collected using a laser power of 1 mW ($\sim$ 14 kW/cm^2) and a 10X ($NA = 0.45$) objective lens ($\sim$ 3 μm in diameter laser spot). The performance of fabricated SERS substrates was evaluated using 1 mM of trans-l,2-bis(4-pyridyl)ethylene (BPE) dissolved in ethanol (Sigma Aldrich). 1 μL droplets of BPE in ethanol were deposited onto SERS substrates and left to dry. SERS signal was evaluated using a measurement area of 5×5 μm^2 at the centre of the dried droplet area.

Process 1	**Figure 1k**
Pressure	6 bar
Time	5 min
Temperature	125 °C
Demoulding Temperature	100 °C
Process 2	**Figure 1j**
Pressure	6 bar
Time	5 min
Temperature	140 °C
Demoulding Temperature	100 °C

TABLE I. Nanoimprinting parameters

B. UV-Vis-NIR measurements

Extinction measurements were carried out using a Shimadzu UV-1800 UV-Vis Spectrophotometer. All samples ($\sim 1x1$ cm^2) were cut from the middle of the 4 inch PMMA foil using a CO2 laser and were fitted inside a cuvette using double adhesive tape, and then aligned perpendicular to the incident light path for acquiring extinction spectra. In order to estimate the LSPR peak position sensitivity to refractive index changes, the spectra were recorded in both air and water surrounding media.

C. Fabrication processes

Fabrication of the gold-coated silicon nanopillar structures (stamp) was carried out by following the procedure described by Schmidt et al. [25]. First, vertically standing Si nanopillar (SiNP) structures were produced via maskless Si reactive ion etching (RIE) process, Figure 1a-b. The Si RIE process was tuned to yield SiNPs with an average radius of 20 ± 5 nm, ~ 500 nm in height and density of $\rho \approx 18 \pm 2$ pillars/μm^2. Second, the fabricated SiNP structures were covered by a 200 nm thick Au metal film using e-beam evaporation, Figure 1c,g. The resulting nanoscale platform is Au-capped silicon nanopillar (Au NP) structure where Au caps can be approximated as an ellipsoid with long and short axes being $a \approx 100$ and $b \approx 60$ nm, respectively, see the Scanning Electron Microscope image in Figure 1g.

Gold metal caps were then transferred over to a PMMA foil using a desktop nanoimprinting tool[37], see the nanoimprinting parameters in Table 1. An assembled stack (from the bottom) was the following: (i) a ceramic wafer which can be heated to a given temperature, (ii) a 4 inch AuNP wafer acting as a stamp (Figure 1c), (iii) the PMMA foil [38], and (iv) a blank 4 inch Si wafer on the top to ensure that the PMMA foil is kept

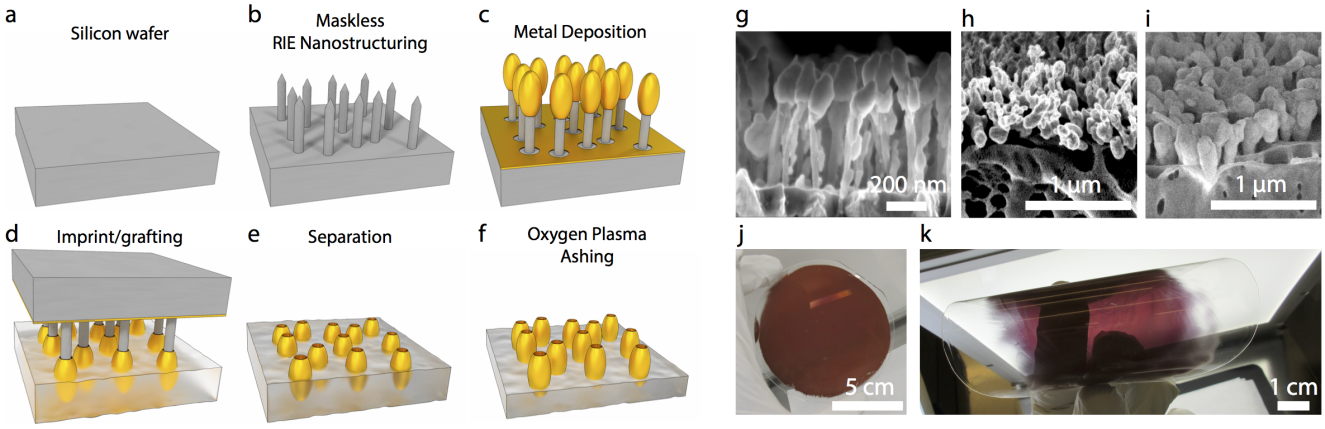

FIG. 1. Schematic of the fabrication process starting (a) with a blank Si wafer that is (b) processed using maskless RIE to achieve a dense array of Si NPs. (c) A metal deposition results in isolated metal caps at the tops of the Si NPs which are (d) grafted onto a PMMA foil using heat and pressure. (e) After separation, the foil and metal particles can be treated with (f) O2-plasma ashing to improve SERS performance. (g) SEM image of silicon nanopillars with gold caps. (h) SEM images of gold and (i) silver caps embedded on the surface of PMMA. (j) Photograph showing a PMMA with embedded gold particles over a wafer-sized area. (k) A photograph demonstrating the transparency and flexibility of a SERS-active PMMA foil.

planar throughout the nanoimprint process. Demoulding was carried out by first removing the PMMA-AuNP wafers and allowing it to cooldown to 100°C, and then inserting a razor blade between the polymer layer and the AuNP stamp. Finally, stripping of the outer layer of PMMA (Figure 1f) was carried out using a plasma asher [39]. The process parameters were the following: 6 min, 70 sccm/min O_2, 70 sccm/min N_2, 80°C temperature, 0.72 mBar and at a coil power of 200 W.

III. RESULTS AND DISCUSSION

A. Au nanocap pattern transfer

The Au and Ag-capped Si NP structures were prepared following a procedure described in ref. [25], see schematic representation in Figure 1(a-c,g) and experimental section. Grafting the metal caps without tearing off the Si NPs was achieved by carefully balancing the nanoimprinting parameters, Figure 1(d-f,h-k). The glass transition point of the polymer must be taken into careful consideration as well as the demolding temperature. Nanoolive pattern transfer into a PMMA foil can be achieved using two different nanoimprint processes, see Table 1. The process 1 can be used to transfer $70-80\%$ of metal nanoolive structures, and the procedure excludes the O2-plasma ashing step shown in Figure 1f. The aim of the process 1 is to partially immerse nanoolives into the PMMA foil during the imprint process. Due to variations in the initial Au NP heights, some nanoolives are not transferred onto the PMMA foil, see corresponding image in Figure 1k. The image shows slight discoloration at the edges of the imprint which indicates that fewer nanoolives were transferred onto the PMMA foil.

The aim of the nanoimprint process 2 is to obtain a full pattern transfer. It was found that by increasing grafting pressure, temperature and time, full 4 inch wafer-scale lift-off of metal caps could be achieved, see the result using the process 2 in Figure 1(j). In this case, the nanoolive structures are fully embedded into the PMMA foil during the pattern transfer process. Even though this ensures a nearly complete pattern transfer an additional O2-plasma ashing step is required, Figure 1f.

Optical properties of the metal caps were verified using electromagnetic calculations based on the 3D finite element method (COMSOL Multiphysics). Metal caps with a void (nanoolive) were modelled in a vacuum with a background planar electric field in order to calculate the extinction spectra and the electric field enhancement distribution around single Ag and Au nanoolives for different incident wavelengths, see Figure 2a-c. The model was setup with a nonuniform adaptive mesh and perfectly matched layers as described in previous work [31]. We find that the agreement between the simulated and experimental extinction spectra is very good, i.e. the LSPR peak positions are within $10-15$ nm, see Figure 2a,b. The nature of the LSPR resonances was evaluated by simulating electric field distribution maps around single, isolated Ag and Au nanoolives at the LSPR peak positions.

In the case of Ag nanoolives, both recorded spectra and calculated extinction cross-sections reveal two LSP resonance peaks at $\lambda_\alpha \approx 360$ and $\lambda_\beta \approx 414$ nm, see Figure 2a. Calculations show that these LSPR modes correspond to the particle mode (α) where the E-field is enhanced around the outside of the metal cap, and the cavity resonance mode (β) where the electric field is mainly localized inside the nanocavity. Note, the nanocavity was formed after the removal of Si NPs via the nanoimprint process,

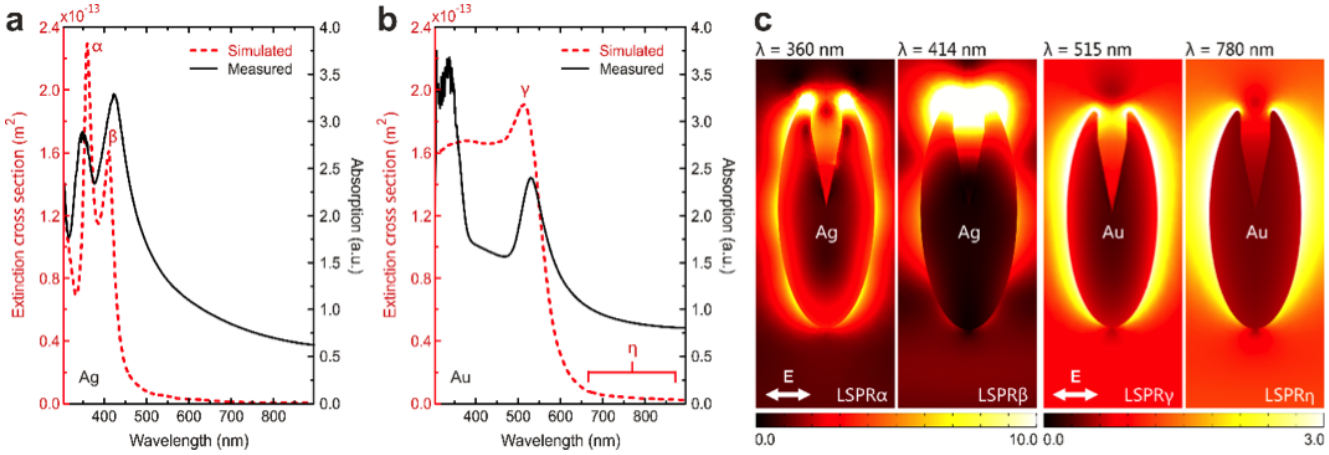

FIG. 2. Theoretical and experimental (UV-Vis-NIR) extinction cross-section spectra of Ag and Au nanoolives, (a) and (b) respectively. Theoretical simulations for single, isolated nanoolives were performed using FEM. Results display two distinct LSPR peaks at $\lambda_\alpha 360$ and $\lambda_\beta \approx 414$ nm for Ag nanooilves, and a single LSPR mode at around $\lambda_\gamma \approx 515$ nm for the Au nanooilive. (c) Electric field distributions around the gold or silver nanoolives showing the enhancement of the electric field at LSPR peak positions. In the case of Au nanoolive, the electric field distribution is also shown for $\lambda_\eta \approx 780$ nm, i.e. the laser excitation wavelength used in SERS experiments.

see the experimental section. For Au nanoolives, a single LSPR mode (γ) corresponding to a particle resonance mode was observed at $\lambda_\gamma \approx 515$ nm, see Figure 2b. We find no evidence of the cavity resonance mode, and even at longer wavelengths ($\lambda_\eta \approx 780$ nm) the resonance nature is unchanged, see E-field maps for an isolated Au nanoolive in Figure 2c. The maximum field intensity around an Au nanoolive is approximately 3 times lower in comparison to a single Ag nanoolive. In summary, both Ag and Au nanoolive plasmonic structures display (i) narrow LSPR lineshapes that can be used to monitor molecular binding events, and (ii) sufficiently high E-field intensities close to the metal surface which is suitable for SERS-based molecular detection.

B. SERS measurements

In this section, we focus on analysing SERS performance of Au nanoolive structures and omit Ag nanoolives for simplicity. Since the nanoolive substrates are aimed for integrated SERS-microfluidic devices, it is important to measure the SERS response from both the front and the backside of fabricated Au nanoolive substrates, see schematic illustration in the inset of Figure 3a. In addition, we compare the performance of Au nanoolive SERS substrates fabricated using nanoimprint processes 1 and 2, see Table 1.

First, we analyse Au nanoolive-PMMA structures produced via process 1. To evaluate SERS performance, trans-1,2-bis (4-pyridyl) ethylene (BPE) at a concentration of 100 μM was used as a target molecule. SERS response from Au nanoolives embedded in PMMA foil was investigated by recording BPE SERS signals from 6 different areas (A-F), see schematic representation in Figure 3b. 1 μL droplets of BPE were placed at each of the 6 measurement areas and left for drying. The measurement areas were within a 2 inch radius from the centre of the Au nanoolive-PMMA foil. In order to characterize the variation of SERS intensities, each measurement area (A-F) shown in Figure 3b was further divided into 25 measurement points. The distance between these points was set to $d = 20$ μm. An example of all 25 recorded BPE SERS spectra from the area (A) is show in Figure 3c. Further, SERS signals from BPE molecules were recorded from both the front and the backside of the Au nanoolive-PMMA foil, see results in Figure 3a. The results show that the backside measurements result in 28% loss in the SERS signal intensity compared to the front side measurements. We find that the relative standard deviation between the averages of the Raman signal at positions (A-F) is 14%, see Figure 3d. Results show a satisfactory homogeneity of the signal across a 2 inch surface area. We also investigated SERS background signals for possible signs of surface contamination. 1 μL droplets of milliQ water were deposited and left for drying. The obtained SERS spectrum indicates minimal background signal, see Figure 3a.

In the second step, we analyse SERS performance of the Au nanoolive structures fabricated using process 2, see Table 1. Prior to SERS measurements, the substrates were exposed to O_2-plasma for $t = 6$ min. The aim of the process is to minimize the nanoolive surface area that is covered by PMMA, see schematic picture in Figure 4b. Results show that oxygen plasma ashing of the samples leads to a dramatic increase in the SERS intensities as an outer layer of PMMA was stripped away, see Figure 4a. The effect was further tested by imprinting the Au nanoolives deeper into the PMMA layer by increasing the imprint temperature to 140°C, thereby making

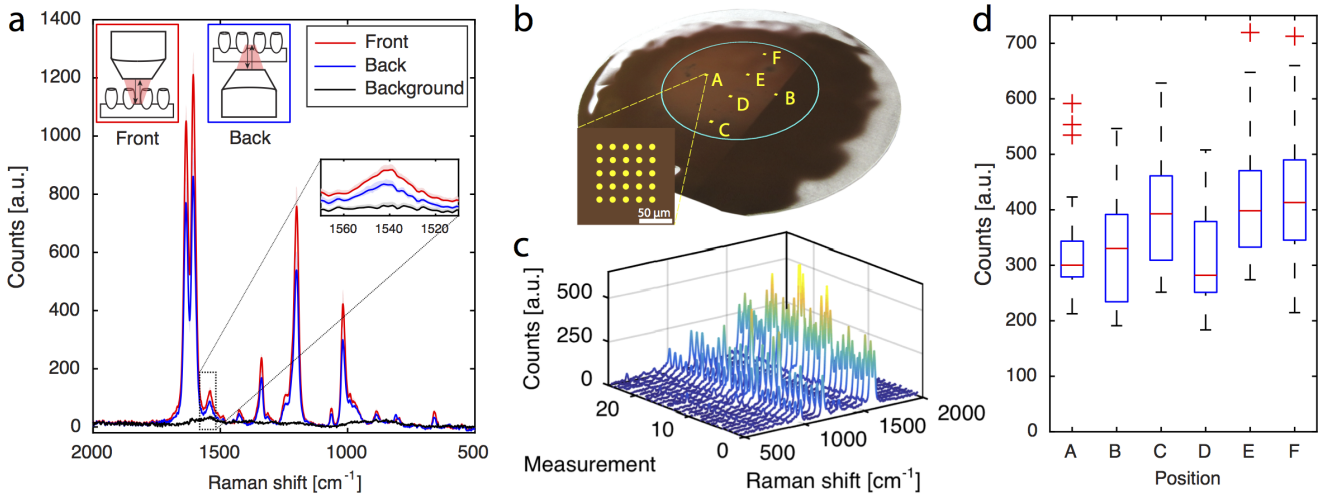

FIG. 3. (a) SERS spectra from 100 μM BPE on gold nanoolives embedded on the surface of PMMA foil measured using a 785 nm laser excitation wavelength (1 mW laser power). The shaded region surrounding the line denote the standard deviation. The SERS spectra were collected from the front of the sample and from the back (through the foil), see schematic illustration in the inset. The SERS performance of Au nanoolives was evaluated at 6 different points (A-F), see schematic illustration in (b). Each point consists of a grid of 5×5 points spread 20 μm apart. The SERS signal variation across an array of 25 measurement points is shown in (c). (d) A boxplot of the SERS signal intensity from the different measurement locations. The boxes show the interquartile range while the errorbars extend to data limits not considered outliers.

the PMMA less viscous, and thereby also allowing for a larger grafting area, as it is shown in Figure 1j. However, the latter diminishes SERS performance, Figure 4a. The extinction spectra in Figure 4b illustrate that the LSPR peak position of Au nanoolives blue-shifts from 537 nm to 517 nm in air cladding when the substrate was exposed to O_2-plasma for $t = 6$ min, indicating removal of PMMA. Additionally, when the peaks were submerged in water, the O2-plasma ashed substrates red-shifted 13 nm, corresponding to an estimated sensitivity of 38 nm RIU^{-1}, while the untreated substrates experienced no measurable shift in the LSPR peak position. This change indicates that the PMMA material was removed and the Au metal caps were now exposed to the surrounding medium of air. The SERS signal intensity shows a dramatic 12-fold increase after exposure to O_2-plasma, see Figure 4a. Additionally, the relative standard deviation of the peak at 1634 cm^{-1} decreased from 42% to 28%, indicating that the homogeneity of the SERS signal intensity was also significantly improved. Finally, we estimate the SERS enhancement factor (EF) of the Au nanoolive substrate fabricated via process 2 using the following formula:

$$EF = \frac{(I_{\mathrm{SERS}}/N_{\mathrm{SERS}})}{(I_{\mathrm{RS}}/N_{\mathrm{RS}})} \qquad (1)$$

where I_{SERS} and I_{RS} were the SERS and the Raman intensity, respectively. N_{SERS} and N_{RS} were the numbers of BPE molecules probed in the SERS and the Raman measurements. Results show that the EF of the Au nanoolive SERS substrate is close to 8.0×10^6, see the experimental and calculation details in the supporting information.

IV. CONCLUSION

A simple method for fabricating transparent and flexible SERS surfaces on a 4 inch PMMA foil using a three-step, maskless fabrication process is presented. The process is compatible with high volume manufacturing process flows and can be extended to 6 and 8 inch wafer sizes. The fabrication process consists of (1) fabrication of gold or silver-capped nanopillar (NP) structures on a 4 inch Si wafer using a simple maskless lithography process, and (2) transferring Au or Ag metal caps (nanoolives) from Au or Ag NP structures onto a polymethylmethacrylate (PMMA) foil using a nanoimprint process. Importantly, the fabrication procedure involves simple moulding and maskless Si RIE techniques, and inexpensive materials such as PMMA. The SERS active substrates are compatible with standard microfluidic fabrication processes and materials, and can readily be integrated into SERS-microfluidic platform.

The Au and Ag nanoolive structures embedded into a PMMA foil display interesting optical properties, i.e. a narrow LSPR line shapes located in the visible spectral region ($\lambda_{(\mathrm{Au,Ag})} \approx 360 - 515$ nm). To understand the results, optical properties of isolated, single Ag and Au nanoolive structures were calculated using the 3D finite element method, and theoretical simulations agree very well with the experimental data. Estimated LSPR sensitivity to refractive index changes for the Au nanoolive substrate is ~ 38 nm RIU^{-1}.

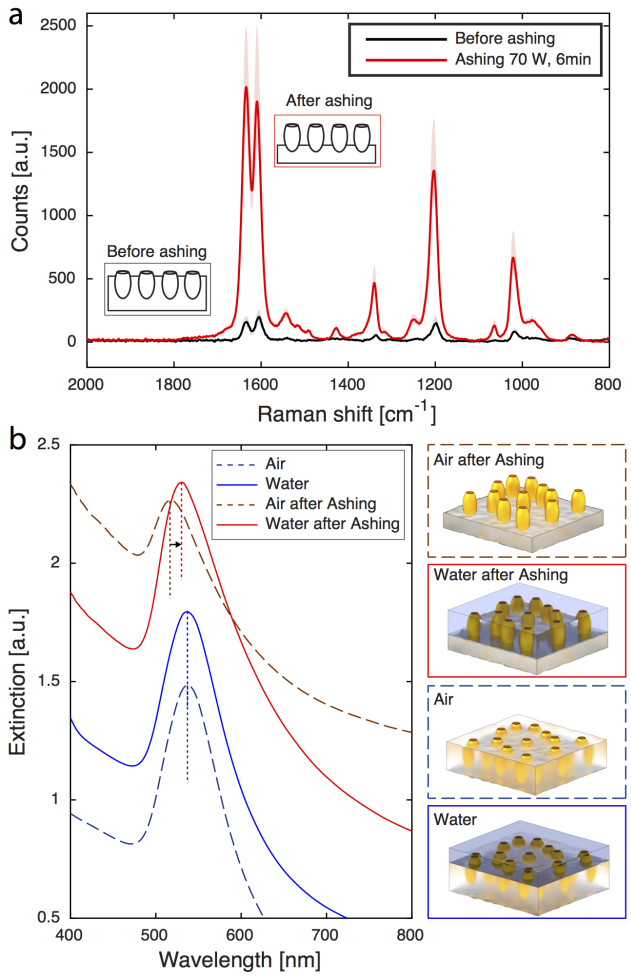

FIG. 4. (a) SERS signal from BPE before and after oxygen plasma ashing. The SERS signal increased approximately a factor 10 after a 6 minute ashing. (b) Transmission measurements revealing extinction LSPR peaks. The LSPR peak blue-shifts as a result of plasma ashing removing PMMA on the gold caps. Additionally, the LSPR peak for the plasma treated caps red-shift 13 nm when the substrate is immersed in water, showing that the metal caps are more exposed.

SERS performance of Au nanoolive-PMMA substrates was analysed in more detail. The SERS signals were collected at different positions across a 2 inch area, and revealed a standard deviation in the SERS signal intensity of 14%. By optimizing the aforementioned step (2) in the fabrication procedure, nearly all Au nanoolives can be transferred onto a PMMA foil. This is achieved by (i) embedding Au NP structures deep into a PMMA foil, and (ii) utilizing O2-plasma ashing process to strip PMMA encapsulating Au nanoolives. The optimized approach yields improvements in both recorded SERS signal intensities and the homogeneity of the signal across a 2 inch surface area. Estimated SERS enhancement factor for the Au nanoolive substrate is 8.0×10^6.

V. ACKNOWLEDGEMENT

This work was funded by the NAPLAS project, The Danish Council for Independent Research as well the European Research Council under the European Union's Seventh Framework Programme (FP7/2007-2013) / ERC grant agreement n° 320535.

[1] Dana Cialla, Anne März, René Böhme, Frank Theil, Karina Weber, Michael Schmitt, and Jürgen Popp. Surface-enhanced Raman spectroscopy (SERS): Progress and trends, 2012.

[2] Bhavya Sharma, Renee R. Frontiera, Anne-Isabelle Henry, Emilie Ringe, and Richard P. Van Duyne. SERS: Materials, applications, and the future. *Materials Today*, 15(1-2):16–25, 2012.

[3] Katrin Kneipp, Yang Wang, Harald Kneipp, Lev T Perelman, Irving Itzkan, Ramachandra R. Dasari, and Michael S. Feld. Single Molecule Detection Using Surface-Enhanced Raman Scattering (SERS). *Physical Review Letters*, 78(9):1667–1670, mar 1997.

[4] Shuming Nie. Probing Single Molecules and Single Nanoparticles by Surface-Enhanced Raman Scattering. *Science*, 275(5303):1102–1106, feb 1997.

[5] Martin Moskovits. Surface-enhanced spectroscopy. *Reviews of Modern Physics*, 57(3):783–826, 1985.

[6] Luca Guerrini and Duncan Graham. Molecularly-mediated assemblies of plasmonic nanoparticles for Surface-Enhanced Raman Spectroscopy applications. *Chem. Soc. Rev.*, 41(21):7085–7107, 2012.

[7] Hongxing Xu, Javier Aizpurua, Mikael Käll, and Peter Apell. Electromagnetic contributions to single-molecule sensitivity in surface-enhanced Raman scattering. *Physical Review E - Statistical Physics, Plasmas, Fluids, and Related Interdisciplinary Topics*, 62(3 B):4318–4324,

2000.

[8] Philip D Howes, Subinoy Rana, and Molly M Stevens. Plasmonic nanomaterials for biodiagnostics. *Chemical Society reviews*, 43(11):3835–53, 2014.

[9] Rebecca A. Halvorson and Peter J. Vikesland. Surface-enhanced Raman spectroscopy (SERS) for environmental analyses. *Environmental Science and Technology*, 44(20):7749–7755, 2010.

[10] Ana Paula Craig, Adriana S Franca, and Joseph Irudayaraj. Surface-enhanced Raman spectroscopy applied to food safety. *Annual review of food science and technology*, 4:369–80, 2013.

[11] Cyril Muehlethaler, Marco Leona, and John R. Lombardi. Review of Surface Enhanced Raman Scattering Applications in Forensic Science. *Analytical Chemistry*, 88(1):152–169, 2016.

[12] Frank Inscore, Chetan Shende, Atanu Sengupta, Hermes Huang, and Stuart Farquharson. Detection of drugs of abuse in saliva by surface-enhanced raman spectroscopy (SERS). *Applied Spectroscopy*, 65(9):1004–1008, 2011.

[13] Jinkai Zheng, Shintaro Pang, Theodore P. Labuza, and Lili He. Evaluation of surface-enhanced Raman scattering detection using a handheld and a bench-top Raman spectrometer: a comparative study. *Talanta*, 129:79–85, 2014.

[14] Aron Hakonen, Per Ola Andersson, Michael Stenbæk Schmidt, Tomas Rindzevicius, and Mikael Käll. Explosive and chemical threat detection by surface-enhanced Raman scattering: A review. *Analytica Chimica Acta*, 893:1–13, 2015.

[15] A Hakonen, T Rindzevicius, M S Schmidt, P O Andersson, L Juhlin, M Svedendahl, A Boisen, and M Käll. Detection of nerve gases using surface-enhanced Raman scattering substrates with high droplet adhesion. *Nanoscale*, 8(3):1305–1308, 2016.

[16] SERSTech.

[17] Bhavya Sharma, M. Fernanda Cardinal, Samuel L. Kleinman, Nathan G. Greeneltch, Renee R. Frontiera, Martin G. Blaber, George C. Schatz, and Richard P. Van Duyne. High-performance SERS substrates: Advances and challenges. *MRS Bulletin*, 38(08):615–624, 2013.

[18] Chao Wang and Chenxu Yu. Analytical characterization using surface-enhanced Raman scattering (SERS) and microfluidic sampling. *Nanotechnology*, 26(9):092001, 2015.

[19] Harold Craighead. Future lab-on-a-chip technologies for interrogating individual molecules. *Nature*, 442(7101):387–393, jul 2006.

[20] George M Whitesides. The origins and the future of microfluidics. *Nature*, 442(7101):368–373, jul 2006.

[21] J Taylor, A Huefner, Li Li, J Wingfield, and S Mahajan. Nanoparticles and intracellular applications of urface-enhanced Raman Spectroscopy. *Analyst*, 141:5037–5055, 2016.

[22] Zhaoying Zhou, Zhonglin Wang, and Liwei Lin. *Microsystems and Nanotechnology*, volume 9783642182. Springer Berlin Heidelberg, Berlin, Heidelberg, 2012.

[23] Canet Acikgoz, Mark A. Hempenius, Jurriaan Huskens, and G. Julius Vancso. Polymers in conventional and alternative lithography for the fabrication of nanostructures. *European Polymer Journal*, 47(11):2033–2052, 2011.

[24] Abhijit Biswas, Ilker S. Bayer, Alexandru S. Biris, Tao Wang, Enkeleda Dervishi, and Franz Faupel. Advances in top-down and bottom-up surface nanofabrication: Techniques, applications & future prospects. *Advances in Colloid and Interface Science*, 170(1-2):2–27, 2012.

[25] Michael Stenbaek Schmidt, Jörg Hübner, and Anja Boisen. Large area fabrication of leaning silicon nanopillars for surface enhanced Raman spectroscopy. *Advanced materials (Deerfield Beach, Fla.)*, 24(10):OP11–8, mar 2012.

[26] D. H. Macdonald, A. Cuevas, M. J. Kerr, C. Samundsett, D. Ruby, S. Winderbaum, and A. Leo. Texturing industrial multicrystalline silicon solar cells. *Solar Energy*, 76(1-3):277–283, 2004.

[27] H Jansen, M Deboer, R Legtenberg, and M Elwenspoek. The Black Silicon Method - A Universal Method For Determining the Parameter Setting of A Fluorine-based Reactive Ion Etcher In Deep Silicon Trench Etching With Profile Control. *Journal of Micromechanics and Microengineering*, 5(2):115–120, 1995.

[28] S. H. Zaidi, D. S. Ruby, and J. M. Gee. Characterization of random reactive ion etched-textured silicon solar cells. *IEEE Transactions on Electron Devices*, 48(6):1200–1206, 2001.

[29] M. Gharghi and S. Sivoththaman. Formation of nanoscale columnar structures in silicon by a maskless reactive ion etching process. *Journal of Vacuum Science & Technology A: Vacuum, Surfaces, and Films*, 24(3):723, 2006.

[30] Anil Haraksingh Thilsted, Jesper Yue Pan, Kaiyu Wu, Kinga Zór, Tomas Rindzevicius, Michael Stenbaek Schmidt, and Anja Boisen. Lithography-Free Fabrication of Silica Nanocylinders with Suspended Gold Nanorings for LSPR-Based Sensing. *Small*, pages 1–8, 2016.

[31] Kaiyu Wu, Tomas Rindzevicius, Michael Stenbæk Schmidt, Klaus Bo Mogensen, Sanshui Xiao, and Anja Boisen. Plasmon resonances of Ag capped Si nanopillars fabricated using mask-less lithography. *Optics Express*, 23(10):12965, 2015.

[32] Alexandre G Brolo, Erin Arctander, Reuven Gordon, Brian Leathem, and Karen L Kavanagh. Nanohole-Enhanced Raman Scattering. *Nano Letters*, 4(10):2015–2018, oct 2004.

[33] Jae Won Jeong, Md Masud Parvez Arnob, Kwang Min Baek, Seung Yong Lee, Wei Chuan Shih, and Yeon Sik Jung. 3D Cross-Point Plasmonic Nanoarchitectures Containing Dense and Regular Hot Spots for Surface-Enhanced Raman Spectroscopy Analysis. *Advanced Materials*, pages 8695–8704, 2016.

[34] Sisi Liu, Zhimou Xu, Tangyou Sun, Wenning Zhao, Xinghui Wu, Zhichao Ma, Haifeng Xu, Jian He, and Cunhua Chen. Large-scale fabrication of polymer/Ag coreshell nanorod array as flexible SERS substrate by combining direct nanoimprint and electroless deposition. *Applied Physics A*, pages 1–6, 2013.

[35] Hyelim Kang, Chul-Joon Heo, Hwan Chul Jeon, Su Yeon Lee, and Seung-Man Yang. Durable plasmonic cap arrays on flexible substrate with real-time optical tunability for high-fidelity SERS devices. *ACS applied materials & interfaces*, 5(11):4569–74, 2013.

[36] Thermo-Scientific Raman DXR, Thermo-Scientific.

[37] Compact Nano Imprinter, NIL Technology, Denmark.

[38] ME303005, polymethylmethacrylate, sheet thickness is 0.25 mm, Goodfellow.

[39] Model 300 Plasma Processor, PVA TePla America.

Chapter 14

P4: LSPR Sensing with Nanocylinders

Lithography-Free Fabrication of Silica Nanocylinders with Suspended Gold Nanorings for LSPR-Based Sensing

Anil Haraksingh Thilsted, Jesper Yue Pan, Kaiyu Wu, Kinga Zór, Tomas Rindzevicius, Michael Stenbæk Schmidt, and Anja Boisen*

***T**unable plasmonic platforms are important for a variety of applications such as photovoltaics, LED's, optoelectronics, medical research, and biosensors. In particular, development of label-free plasmonic biosensors is one of the key research areas that utilizes plasmonic nanostructures for detection of biologically relevant molecules at low concentrations. The authors have developed a cost-effective, fast, and lithography-free method to fabricate transparent fused silica nanocylinders. The technique allows tuning of nanocylinder height, diameter, and density and can be scaled to large surface areas, such as 8 in. wafers. The authors demonstrate that gold coated nanocylinders support localized surface plasmon resonances (LSPR) from visible to near infrared wavelengths. The plasmonic platform can be characterized as suspended gold nanorings and exhibits a sensitivity of 658 nm RIU^{-1} with a figure-of-merit of 10, comparable to other state-of-the-art LSPR sensing platforms that utilize more complex nanofabrication pathways. It was observed that the LSPR peak positions can be controlled by varying the geometry of the nanocylinders. The authors illustrate surface functionalization, biosensing, and surface regeneration properties of the platform using thiols and detection of bovine serum albumin (BSA). The observed LSPR shifts for 11-mercaptoundecanoic acid and BSA was 12 and 26 nm, respectively.*

1. Introduction

Noble metal nanostructures display interesting optical properties that are particularly relevant for biosensing applications.[1] The nanoparticle optical response to an incident electromagnetic field is known as the localized surface plasmon resonance (LSPR) and is due to collective resonant oscillations of the conduction electrons. LSPRs can be excited by light, which leads to a strong enhancement of the local field and exhibits prominent light absorption and scattering.[2,3] The nanoparticle optical response is usually dominated by dipolar modes and the LSPR peak position depends strongly on nanostructure geometry and refractive index (RI) of the surrounding medium.[4] Typically, refractive index and molecular sensing using LSPRs are carried out using chemically synthesized solutions of silver or gold colloids. Measurements of the LSPR response, as a function of the RI change, have either been carried out on single or an ensemble of particles, with varying degrees of performance.[5] Advances in nanofabrication techniques have allowed for more precise control of nanostructure morphology, significantly improving optical properties and resulting in advances in sensing applications, commonly by means of measuring a shift in the LSPR peak position.[6] Recently, a new class of extremely sensitive biosensing platforms based on 2D porous gold nanorod arrays or hyperbolic

A. H. Thilsted, J. Y. Pan, Dr. K. Wu, Dr. K. Zór, Dr. T. Rindzevicius, Dr. M. S. Schmidt, Prof. A. Boisen
Department of Micro- and Nanotechnology
The Technical University of Denmark
2800 Kongens Lyngby, Denmark
E-mail: ahath@nanotech.dtu.dk

DOI: 10.1002/smll.201602299

small 2016,
DOI: 10.1002/smll.201602299

metamaterials that can reach sensitivities of 30 000 nm per refractive index unit (RIU) have been reported.[7,8] Even though both gold nanorod and hyperbolic metamaterials exhibit high sensitivities, the former is feasible only in the infrared spectral region while the latter involves complex fabrication procedures which can limit their use in routine point-of-care (POC) applications.[9] In fact, most plasmonic platform fabrication techniques often involve either top-down processes such as electron-beam lithography,[10,11] an expensive and time-consuming process that can only pattern small areas, or advanced bottom-up techniques such as block copolymer[12–14] or nanosphere lithography.[15,16]

Extensive work has been carried out both experimentally and theoretically to characterize and tune the optical properties of various nanoparticles[17,18] and nanocavity[19,20] based plasmonic structures. Specifically, metallic rings or tori have shown promise as highly tunable plasmonic structures[21,22] with a well-understood analytical and finite-difference time-domain model for the electric field distribution.[23,24] Gold nanorings exhibit significant field enhancement useful for highly sensitive LSPR based detection.[25–27] Additionally, it has been shown that the sensitivity of plasmonic structures can be increased significantly by simply raising the metallic structures above the substrate. For structures at a near proximity to the substrate, a large portion of the field will be in the substrate where it is insensitive to RI changes. The effect of suspending the structures above the substrate was explored by Dmitriev et al.[28] as well as Otte et al.[29] who showed significant performance increase. It is therefore important to combine the sensitivity and large tunability range of plasmonic metal nanorings with the sensitivity of metal structures suspended above the substrate. The structures are preferably achieved by a straightforward and fast fabrication method.

In contrast to nanosphere and e-beam lithography, maskless reactive ion etching (RIE) forms nanostructures in a single and fast fabrication step. When combined with a subsequent metallization step, the process has been utilized for producing wafer-scale silver and gold coated silicon nanopillar arrays for surface-enhanced Raman scattering applications.[30,31] While maskless nanostructuring in silicon is well understood, the lack of optical transparency, limited chemical resistance, and insufficient biocompatibility leave much to be desired for sensing applications.[32] It is therefore desirable to extend the method for fabricating plasmonic structures to optically transparent materials. A method for achieving nanostructures in fused silica using lithography-free RIE was initially proposed by Zeze et al.[33] and further developed for a variety of other nanostructures by Lilienthal et al.[32] and Hein et al.[34] Prior to this work, optimization of the nanocylinder geometry along with precise control of the height, diameter, and density of the nanocylinders has not been reported. In particular, we propose that lithography-free RIE of fused silica could be used to realize suspended gold nanoring configurations.

In order to address the drawbacks of complicated and expensive nanofabrication steps that are generally employed to produce plasmonic biosensing platforms, we have developed a fast, cost-effective, and simple fabrication method that yields wafer-scale fused silica nanocylinder structures. Importantly, we demonstrate control of the geometry of fused silica nanocylinders achieved by only adjusting RIE process parameters. The deposited gold layer results in isolated metal rings at the tops of the nanocylinders serving as plasmon resonance structures suspended above the substrate. We show that the optical properties of suspended gold nanorings can be controlled by tuning the dimensions and density of the nanocylinders through the RIE process parameters. Furthermore, we evaluate the LSPR sensing characteristics of the platform by measuring the RI sensitivity, figure-of-merit (FoM), and recording molecular binding events. The fabrication technique presents the key advantage of being a high-throughput and tunable method of obtaining LSPR substrates for conventional use. Since the proposed configuration can be achieved on wafer-scale, the practical realization of a sensor is achievable for a range of applications and is suitable for POC devices.

2. Results and Discussion

2.1. Nanocylinder Fabrication

Nanocylinders were fabricated on the surface of fused silica wafers via a one-step self-masking RIE process. Sulfur hexafluoride (SF_6) and dioxygen (O_2) gas were injected into a vacuum chamber, and ionized to form a plasma using a radio frequency oscillating electric field. The ions of the plasma were accelerated in an additional electric field to impact the surface of the substrate and etch material away. A predeposited aluminum layer on the fused silica resulted in sputtered residues that functioned as nanoscale masks, evidence of which is shown using energy-dispersive X-ray spectroscopy. Aluminum was chosen as it was previously documented for use for the formation of fused silica nanostructures via RIE.[33] These nanoscale masks induce local differences in etching selectivity, thus forming the nanostructures. However, the formation of nanocylinders due to these nanoscale masks is not fully understood.[33] An illustration of the predeposited aluminum pattern and SEM images of the resulting nanocylinders is illustrated in **Figure 1**.

The flow rate of gases, the coil power used to generate the plasma, the platen power used to accelerate the ions, the pressure in the plasma chamber, and the temperature of the substrate must all be carefully balanced in order to form the desired structures. Additionally, details such as the configuration of the RIE tool, the wafer cooling method, and size of the substrate and chamber conditions before etching may have significant effects on the geometry of the nanostructures. The etching process is strongly dependent on the initial chamber conditions and therefore, a 3 min O_2 chamber cleaning was carried out before each etch. As the creation of the nanocylinders requires sputtering off the aluminum pattern, the morphology was dependent on the distance to the mask. Large variations in the density of the nanocylinders were observed if the fused silica wafer did not have sufficient coverage of aluminum. In order to ensure homogeneity across the wafer, an aluminum pattern was designed to ensure a maximum distance of 2.75 mm to the aluminum layer from

small 2016,
DOI: 10.1002/smll.201602299

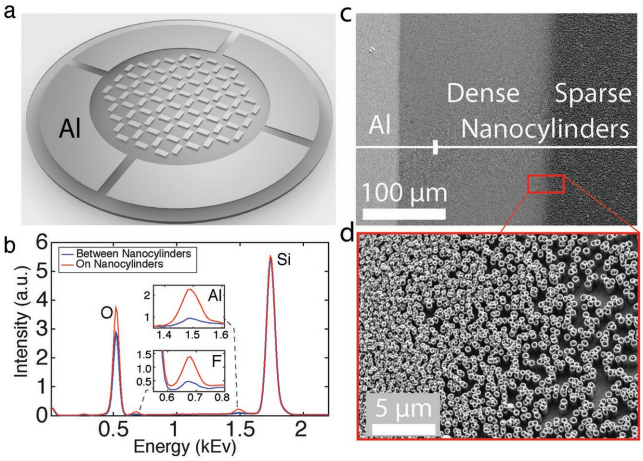

Figure 1. a) The aluminum pattern used on the 4 in. silica wafer, with the outer ring ensuring electrostatic clamping in the etch chamber and the inner rectangle array to ensure homogeneous nanocylinder density. b) Energy-dispersive X-ray spectroscopy measurements show the presence of aluminum and fluorine, and heightened signal on the sites of the nanocylinders. c,d) Scanning electron microscope (SEM) images showing how aluminum sputtering causes nanocylinders to form. The nanocylinders are dense near the aluminum areas, but from 200 µm and out, they become less dense and with a homogeneous distribution.

the glass regions. Nanocylinders were found to be much denser within 200 µm from the aluminum layer, but thereafter became sparser and had a homogeneous density that does not change with distance. Additionally, as the etching process is dependent on the specific tool used, some modification of the etching parameters is required if transferred to other instruments. An etch process was developed that served as the starting point for etch parameter variation, listed in **Table 1**.

This etch process resulted in nanocylinders with a height of 1410 ± 36 nm, a diameter of 300 ± 23 nm, and a density of 1.10 ± 0.6 µm^{-2}. The nanocylinder geometry was measured across the entire wafer and a distributed aluminum mask was used as an effective way to produce homogeneous results across a large area.

Table 1. Standard nanocylinder etching process.

SF_6 flow	150 sccm
O_2 flow	30 sccm
Pressure	40 mTorr
Platen power	120 W
Coil power	800 W
Chuck temperature	20 °C
Etch time	6 min

It is possible to tune the height and diameter of the nanocylinders by varying the etching parameters. The dimensions and densities of the nanocylinder as a function of platen power and etch time are plotted in **Figure 2**. Increasing platen power from 100 to 300 W resulted in nanocylinders with a diameter increasing from 0.20 to 0.89 µm with only a decrease in height from 1.41 to 1.04 µm. The decrease in height was most likely due to the walls of the nanocylinders being etched down with a more physical etching process. For nanocylinders above ≈800 nm in diameter, structures were observed to form inside the hollow cores—possibly nanocylinders within nanocylinders, as shown in Supporting Information for larger nanocylinder diameters. The density was observed to decrease from 1.19 to 0.97 µm^{-2}, as platen power increased from 100 to 300 W.

Increasing the etching time from 4 to 14 min resulted in an increase in height from 0.96 to 3.36 µm with almost no change in diameter. However, for nanocylinders with a height greater than ≈2.5 µm, tearing and buckling were observed, especially at the base of the nanocylinders—possibly due to thinning of sidewalls and subsequent mechanical failure. As with increasing platen power, the density decreased from 2.00 µm^{-2} and stabilized at ≈1.5 µm^{-2} for etch times above 8 min. The cause for the changes in density are not fully understood, but were clearly observed to be affected by the platen power and etch times. However, by combining certain platen powers and etch times,

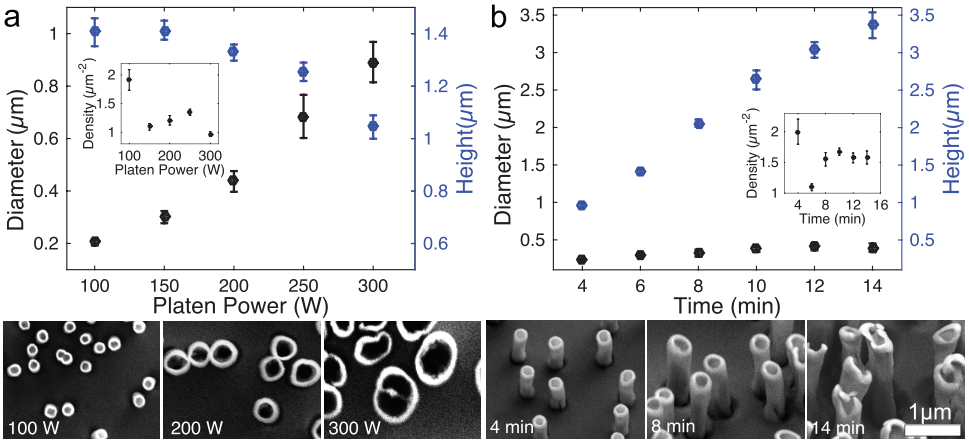

Figure 2. Control of the morphology of the nanocylinders by varying the platen power and time of the etching process. a) Increasing the platen power increases the diameter of the nanocylinders and a slight decrease in the height is observed. The density decreases as the available space decreases with wider nanocylinders. The etching time was fixed to 6 min. b) Increasing the etching time results in taller nanocylinders, with almost no change in the nanocylinder diameter. The density decreases initially with increasing etching time but stabilizes at ≈1.6 µm^{-2}. The platen power was fixed at 120 W. Errorbars show the standard deviation resulting from 10 measurements of dimensions, taken at different locations across the entire wafer using SEM imaging.

DOI: 10.1002/smll.201602299

www.MaterialsViews.com

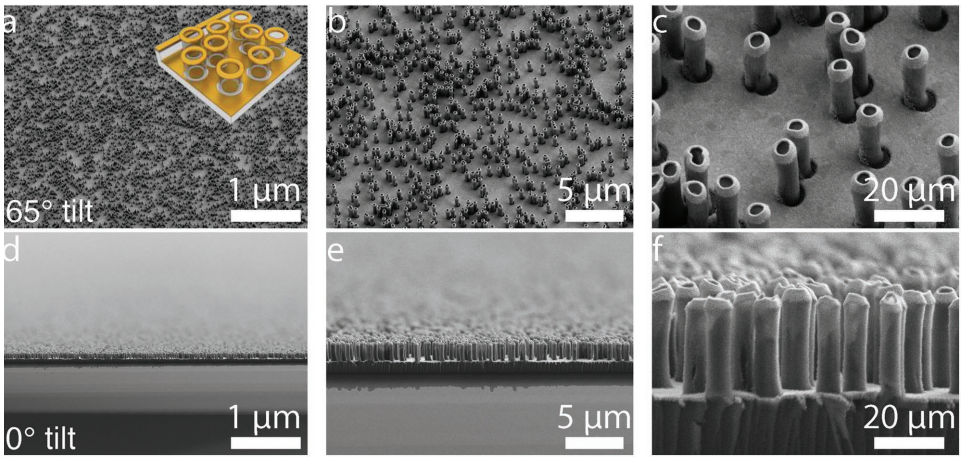

Figure 3. SEM images showing nanocylinders with suspended gold rings and with a continuous gold film between them. The insert in (a) shows a sketch of the silica nanocylinders after gold deposition with suspended gold rings and a gold film between the nanocylinders. The SEM images are shown for (a–c) at 65° tilt and at (d–f) 0° tilt at different magnifications, showing a homogeneous density, height, and diameter of the suspended gold rings.

a desired diameter and height for the nanocylinders can be achieved despite the stochastic nature of the RIE process.

E-beam deposition resulted in metallic rings along the rim of the nanocylinders and a continuous thin film between the nanocylinders, shown in **Figure 3**. At the base of the nanocylinders, cavities in the gold film arose due to the masking effect of the nanocylinders during gold deposition. The cavity size was estimated to be slightly larger than the diameter of the nanocylinders. The gold rings' outer diameters were the same as the diameter of the nanocylinders, whereas the thicknesses of the gold ring walls were 90.7 nm.

2.2. Optical Properties

A qualitative understanding of the resonance modes were investigated using 3D FEM simulations using mean geometric values of fabricated nanocylinders: 300 nm diameter,

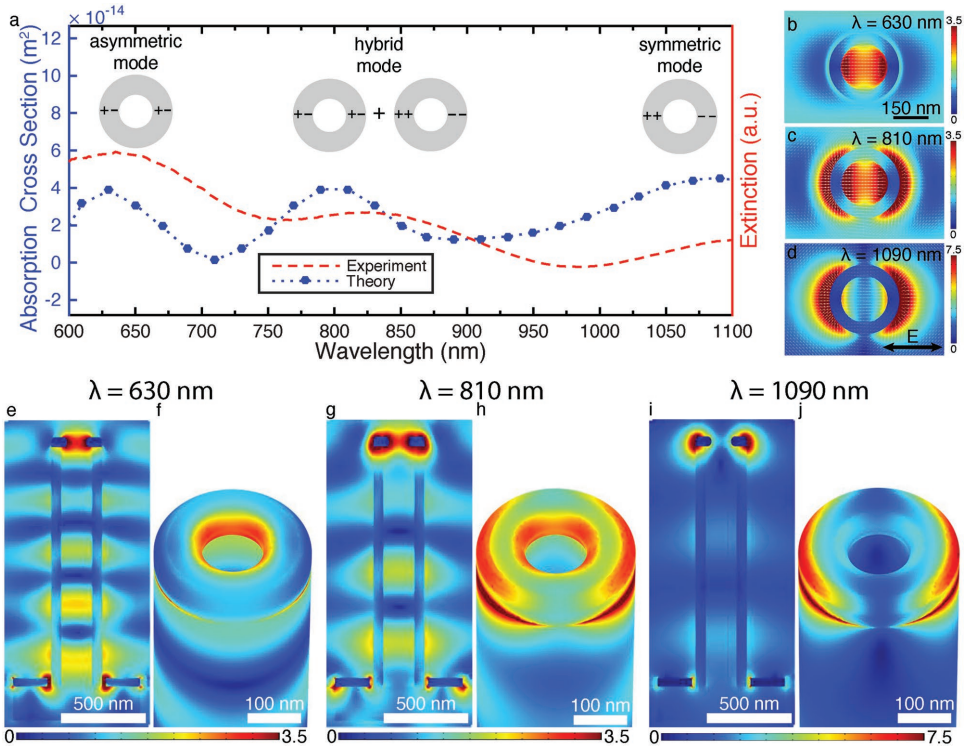

Figure 4. a) A comparison of absorption cross section calculated from a simulation with measurements of the extinction spectrum, showing three distinct peaks between 600 and 1100 nm corresponding to three resonance modes. b) Top-down view of the electric field distribution of the asymmetric mode, c) the hybrid mode, and the d) symmetric mode. e) The cross-sectional view and f) tilted view of the electric field at the surface of the gold nanoring for the asymmetric mode at $\lambda = 630$ nm, for the g,h) hybrid mode at $\lambda = 810$ nm and the i,j) symmetric mode at $\lambda = 1090$ nm. The scale bars show the electric field enhancement.

small 2016,
DOI: 10.1002/smll.201602299

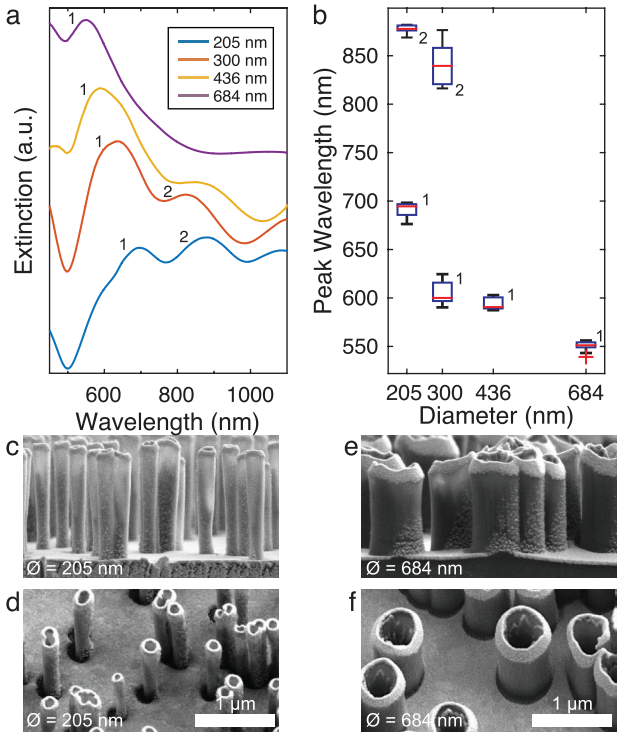

Figure 5. a) Representative extinction spectra of nanocylinders with varying diameters. Three LSPR peaks between 500 and 1100 nm were observed as well as the gold intraband transition antipeak at 500 nm. b) Increasing nanocylinder diameters resulted in a blue-shift of the asymmetric mode from 691 to 550 nm. The hybrid mode first blue-shifts from 877 to 793 nm, but red-shifts again for nanocylinders with a larger diameter of 436 nm. Boxplots are based on 10 measurements at different wafer locations. Errorbars extend to data limits that are not considered outliers. c,d) SEM micrographs of gold capped nanocylinders of small diameters and e,f) larger diameters.

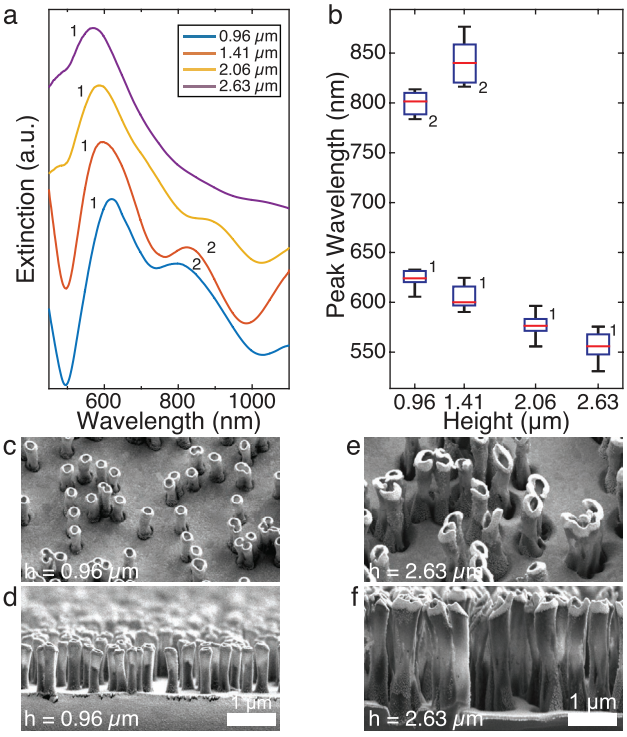

Figure 6. a) Representative extinction spectra of nanocylinders with varying heights. Three LSPR peaks between 500 and 1100 nm were observed. b) Increasing the nanocylinder height resulted in a linear blue-shift of the asymmetric mode from wavelength 624 to 556 nm. The hybrid mode was observed to red-shift as well as become weaker for taller nanocylinders. Boxplots are based on 10 measurements at different locations across a wafer. c,d) SEM micrographs of shorter nanocylinders and e,f) taller nanocylinders with 50 nm gold caps.

1413 nm height and a gold layer thickness of 50 nm. The distance between the gold nanorings and film is referred to in this work as the nanocylinder height. The electric field distribution at different wavelengths are observed and the predicted absorption cross-section was compared with measured extinction spectra, as shown in **Figure 4**. The model showed three clear modes observed between wavelengths of 600 and 1100 nm: the asymmetric mode at ≈630 nm in which there is a strong coupling between the inner and outer part of the gold torus wall; the symmetric mode at ≈1090 nm in which the particle exhibits a dipolar resonance; and a hybrid mode of the symmetric and antisymmetric mode at ≈810 nm. These resonance modes were likewise observed in the extinction spectra.

The model does not take into account the inter-nanocylinder electromagnetic coupling and stochastic spread in morphology and scattering. Despite this shortcoming, the model agrees qualitatively with experiments.

The ability to tune the morphology of nanocylinders in a predictable fashion allows for tuning of the LSPR peaks. Extinction spectra were measured for nanocylinders varying from 205 to 684 nm in diameter, with a 50 nm gold layer thickness. Note that the change in nanocylinder diameter accompanied a change in density and height as described above. The resulting extinction spectra for varying nanocylinder diameters are shown in **Figure 5**.

Extinction spectra show three distinct peaks between 500 and 1100 nm with the exception of the nanocylinders with a diameter of 684 nm. The peak positions of the LSPR modes were found to blue-shift from 691 to 550 nm for the asymmetric mode. The hybrid mode blue-shifts first from 877 to 793 nm but red-shifts for nanocylinders with a larger diameter of 436 nm. Although not directly calculated, as the LSPR peak extended beyond the measurement capabilities of the instrument, the measurements suggested a red-shift of the symmetric mode with increasing nanocylinder diameter.

The blue-shift of the asymmetric and hybrid LSPR peak modes was attributed to possibly retardation effects in intraparticle electromagnetic interaction, as described by Aizpurua et al.[21] Additionally, the inferred red shift of the third mode was attributed to the larger gold ring size for wider nanocylinders. The hybrid resonance mode weakens for nanocylinders with larger diameters, most likely due to more merging of the nanocylinders as the space between them decreases, which deforms the gold nanorings.

Varying the nanocylinder height is another way of tuning the LSPR peak position. Extinction spectra were measured for nanocylinders with heights between 0.96 and 2.63 μm. The extinction spectra are shown in **Figure 6**.

Three LSPR peaks were identified between wavelength 500 and 1100 nm. A linear blue-shift from 624 to 556 nm was observed for the asymmetric LSPR peak. In contrast to this,

small 2016,
DOI: 10.1002/smll.201602299

a red-shift from 800 to 841 nm was observed as the nanocylinder height increased from 0.96 to 1.41 μm. The hybrid peak became more red-shifted and weaker as the height increased further to 2.06 μm and disappeared completely for taller nanocylinders. The disappearance of the hybrid mode for taller nanocylinders is most likely due to merging of the nanocylinders and buckling of the sidewalls that deform the metal nanorings, thus weakening the LSPR resonance.

The ability to fabricate nanocylinders of a certain height and diameter allows for tuning the LSPR peaks for the asymmetric, hybrid, and symmetric modes in the visible to near infrared regions. In addition, varying the gold thickness allows for further LSPR peak tuning (see Supporting Information).

2.3. Refractive Index Sensing

Measurements of bulk RI sensitivity and FoM were carried out using sucrose solutions of varying concentrations. Representative extinction spectra and peak wavelength shifts for varying RI solutions are shown in **Figure 7**.

Peak shift showed a strong linear response to increased cladding refractive index. Nanocylinders with a height of 962, 1400, and 1413 nm showed a RI sensitivity of 474, 550, and 595 nm RIU^{-1}, respectively. The LSPR peak width at half prominences for the asymmetric mode for these nanocylinder heights was 118, 99, and 115 nm, respectively. Additionally, the peak width at half prominence was found to increase for higher RI, indicating peak broadening. The FoM is defined as the sensitivity divided by the peak width at half prominence and was calculated to be 4.01, 5.57, and 5.18, respectively. An increase in the nanocylinder height resulted in a sensitivity increase, and to a greater degree than varying the diameter. When increasing the height from 1400 to 1413 nm there was a negligible change in sensitivity despite the large increase in diameter from 204 to 300 nm. The nanocylinders with the greatest sensitivity, 685 nm RIU^{-1}, were nanocylinders with a height of 2060 nm and a diameter of 324 nm. Additionally, nanocylinders with this height exhibited a peak width at half prominence of 69.3 nm, resulting in a FoM of 9.87. The FoM is significantly better than for conventional metal colloids that have FoM of typically under 4[5] and are similar to some of the best FoM values obtained via more complex nanosphere lithography methods.[16] The symmetric mode at the longest wavelength may have even higher sensitivity as indicated by previous work with metal nanorings.[27]

Surface RI sensing was verified using two commonly used thiols: 11-mercaptoundecanoic acid (MUA) (10×10^{-3} M in ethanol) and cystamine hydrochloride (Cys) (10×10^{-3} M in water). The formation of a self-assembled monolayer of thiols resulted in shifts in the LSPR peak position. Structures modified with Cys were further incubated in bovine serum albumin (BSA) (1.5×10^{-6} M in a phosphate buffered saline (PBS) solution), chosen as a model protein. The binding of the protein to the positively charged thiol layer could be reversed by a 15 min incubation in *Tris* buffer (pH 9.9). Extinction spectra were measured in dry states. The extinction spectra and the calculated peak shifts for the Cys covalent binding to the gold surface as well as the electrostatic interaction between the BSA and the Cys are shown in Figure 7.

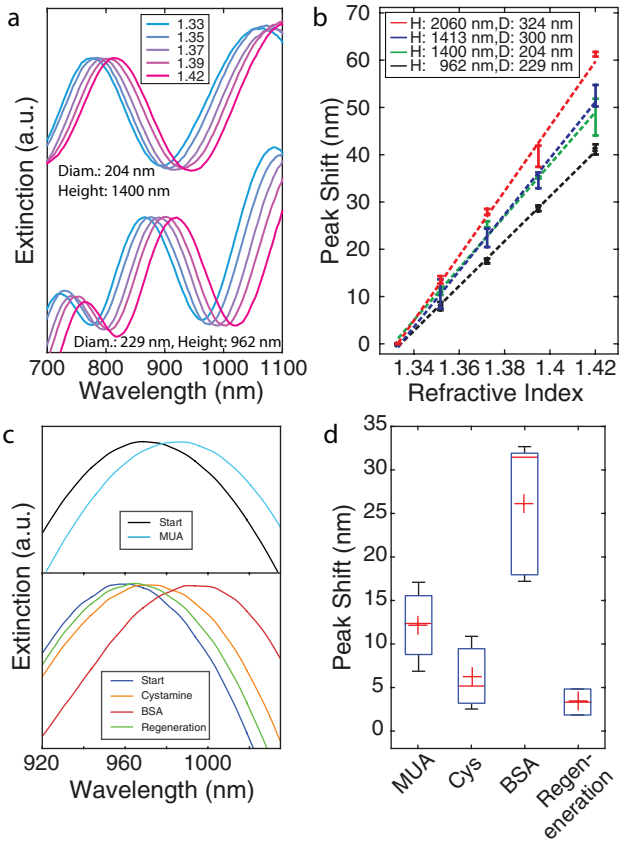

Figure 7. a) Representative extinction spectra of nanocylinders immersed in sucrose solutions with varying refractive indices. The red-shifting spectra are shown for nanocylinders with a diameter of 204 nm and nanocylinders with a height of 963 nm. b) A plot of the LSPR peak wavelength as a function of the refractive index. Dashed lines show a linear regression. Three measurements were taken for each nanocylinder geometry and refractive index. A linear increase of peak shift is evident and nanocylinders with a height of 2060 nm have the greatest sensitivity of 685 nm RIU^{-1}. c) Representative spectra showing a peak shift as a result of MUA and Cys binding to the gold surfaces, as well as BSA interaction with Cys, before and after regeneration. d) Peak shifts due to the Cys binding and BSA interaction with Cys before and after regeneration. Three measurements were carried out between at least two substrates. Crosses denote the mean value.

Extinction spectra showing a significant red-shift of 12.2 ± 4.4 nm for MUA binding to the surface and 6.18 ± 4.27 nm for Cys binding. BSA binding via electrostatic interaction to the Cys covered gold surfaces resulted in a peak shift of 26.3 ± 7.8 nm. Regeneration of the surface showed that it was possible to detect the removal of BSA using the peak shift, dropping the peak shift back to 3.3 ± 2.2 nm. These peaks shifts are on level with results obtained by comparable substrates fabricated using lithographic methods.[27,35]

3. Conclusion

In this paper, we report a fabrication method using RIE to achieve large area, high density nanocylinders that are easily tunable in both diameter and height. The fabrication process

small 2016,
DOI: 10.1002/smll.201602299

is straightforward, cost-effective, fast, and compatible with high volume manufacturing process flows. A gold coating achieved with e-beam deposition results in suspended gold nanorings, exhibiting plasmonic properties. Using optical transmission, several prominent LSPR extinction peaks were measured in the VIS-NIR range. The maximum RI sensitivity of 685 nm RIU^{-1} was found with gold nanocylinders with a height of 2060 nm, a diameter of 324 nm, and a density of 1.55 μm^{-2}. The LSPR peak width at half prominence was 69.3 nm, resulting in a FoM of 9.87. Surface binding events were characterized, showing a peak shift of 12.2 ± 4.4 nm for MUA, 6.18 ± 4.27 nm for Cys, and 26.25 ± 7.8 nm for BSA. These findings suggest that suspended gold rings on transparent fused silica nanocylinders fabricated using RIE is a strong candidate for a highly tunable, sensitive, low-cost sensor for bio/chemical detection using LSPR.

4. Experimental Section

Fabrication and Characterization: The nanocylinders were fabricated using 4 in. double side polished fused silica wafers with a 500 µm thickness.[36] The aluminum mask[37] was achieved using e-beam evaporation through an aluminum shadowmask. The wafers were then placed in a reactive ion etcher tool.[38] The gold film was deposited using the e-beam evaporator. Nanostructures were characterized using a scanning electron microscope.[39]

Simulation and Optical Characterization: Simulation of the plasmonic structures and prediction of the LSPR peak position was carried out using finite-element modeling in COMSOL[40] using the radio-frequency module. A simplified model was constructed consisting of a single nanocylinder with a gold ring placed at the top rim of the nanocylinder. The top of the substrate surrounding the nanocylinder was also covered using gold film. The boundaries of the model were enclosed in perfectly matched layers. RI of the gold layer was obtained from Johnson and Christry.[41] and the RI of fused silica was obtained from Malitson.[42] The electric field distribution was calculated after introducing a planar wave incident to the substrate surface with varying wavelength.

Optical characterization of the gold coated nanocylinders was carried out using a transmission spectrophotometer.[43] A 2×2 mm area of the wafer was selected and measurements were carried out from $\lambda = 400$ nm to $\lambda = 1100$ nm. LSPR peak positions were calculated using by first approximating a position using MatLab's find peaks function. Varying data window sizes were defined around this peak guess and each data crop was fitted to a binomial (see Supporting Information). The maximum position of the binomial fit determined the peak position.

Bulk RI Sensing: Bulk RI sensing was characterized using sucrose solutions[44] at varying concentrations. The LSPR substrates were placed in a cuvette and a light blocker was used so that all light passed through the solution as well as the substrate (see Supporting Information). Sucrose solutions were prepared from 0 to 50°Bx, corresponding to a RI shift from 1.333 to 1.4201.[45]

Surface Sensing: Cys, 11-MUA, BSA, PBS, TrizmaÂbase, sodium hydroxide, were purchased from Sigma-Aldrich Corporation (St. Louis, MO, USA). 99% ethanol and absolute ethanol were from Kemetyl A/S (Køge, Denmark). In all cases, after the removal of the functionalization or incubation solution, the structures were rinsed three times with water and dried prior measurement. All aqueous solutions were prepared in ultrapure water, obtained from a Milli-Q water purification system.[46]

Supporting Information

Supporting Information is available from the Wiley Online Library or from the author.

Acknowledgements

Thanks to Rodrigo Pimental for his assistance with the experimental setup for RI sensing. This work was conducted by the NAPLAS project, funded by the Danish Council for Independent Research and the European Research Council under the European Union's Seventh Framework Programme (FP7/2007-2013)/ERC grant agreement no. 320535.

[1] K. A. Willets, R. P. Van Duyne. *Annu. Rev. Phys. Chem.* **2007**, *58*, 267.
[2] M. Faraday, *Philos. Trans. R. Soc. London* **1857**, *147*, 145.
[3] G. Mie, *Ann. Phys.* **1908**, *330*, 377.
[4] C. F. Bohren, D. R. Huffman. *Absorption and Scattering of Light by Small Particles*. Wiley-VCH, Weinheim, Germany **2008**.
[5] K. M. Mayer, J. H. Hafner, *Chem. Rev.* **2011**, *111*, 3828.
[6] J. N Anker, W. Paige Hall, O. Lyandres, N. C. Shah, J. Zhao, R. P. Van Duyne, *Nat. Mater.* **2008**, *7*, 442.
[7] A. V. Kabashin, P. Evans, S. Pastkovsky, W. Hendren, G. A. Wurtz, R. Atkinson, R. Pollard, V. A. Podolskiy, A. V. Zayats, *Nat. Mater.* **2009**, *8*, 867.
[8] K. V. Sreekanth, Y. Alapan, M. ElKabbash, E. Ilker, M. Hinczewski, U. A. Gurkan, A. D. Luca, G. Strangi, *Nat. Mater.* **2016**, *4*, 621.
[9] F. B. Myers, L. P. Lee, *Lab. Chip* **2008**, *8*, 2015.
[10] N. Verellen, P. V. Dorpe, C. Huang, K. Lodewijks, G. A. E. Vandenbosch, L. Lagae, V. V. Moshchalkov, *Nano Lett.* **2011**, *11*, 391.
[11] S. Kim, J. M. Jung, D. G. Choi, H. T. Jung, S. M. Yang, *Langmuir* **2006**, *22*, 7109.
[12] D. O. Shin, J.-R. Jeong, T. H. Han, C. M. Koo, H.-J. Park, Y. T. Lim, S. O. Kim, *J. Mater. Chem.* **2010**, *20*, 7241.
[13] J. H. Mun, S. K. Cha, H. Kim, H.-S. Moon, J. Y. Kim, H. M. Jin, Y. J. Choi, J. E. Baek, J. Shin, S. O. Kim, *Small* **2014**, *18*, 1.
[14] S. K. Cha, J. H. Mun, T. Chang, S. Y. Kim, J. Y. Kim, H. M. Jin, J. Y. Lee, J. Shin, K. H. Kim, S. O. Kim, *ACS Nano* **2015**, *9*, 5536.
[15] T. R. Jensen, M. D. Malinsky, C. L. Haynes, R. P. Van Duyne, *J. Phys. Chem. B* **2000**, *104*, 10549.
[16] E. M. Hicks, X. Zhang, S. Zou, O. Lyandres, K. G. Spears, G. C. Schatz, R. P. Van Duyne, *J. Phys. Chem. B* **2005**, *109*, 22351.
[17] A. J. Haes, S. Zou, G. C. Schatz, R. P. Van Duyne, *J. Phys.Chem. B* **2004**, *108*, 6961.
[18] E. Hutter, J. H. Fendler, *Adv. Mater.* **2004**, *16*, 1685.
[19] A. Lesuffleur, H. Im, N. C. Lindquist, S.-H. Oh, *Appl. Phys. Lett.* **2007**, *90*, 243110.
[20] M. P. Jonsson, A. B. Dahlin, P. Jönsson, F. Höök, *Biointerphases* **2008**, *3*, FD30.
[21] J. Aizpurua, P. Hanarp, D. S. Sutherland, M. Käll, G. W. Bryant, F. J. G. de Abajo, *Phys. Rev. Lett.* **2003**, *90*, 057401.

DOI: 10.1002/smll.201602299

[22] P. Nordlander, *ACS Nano* **2009**, *3*, 488.
[23] C. M. Dutta, T. A. Ali, D. W. Brandl, T.-H. Park, P. Nordlander, *J. Chem. Phys.* **2008**, *129*, 084706.
[24] F. Hao, P. Nordlander, M. T. Burnett, S. A. Maier, *Phys. Rev. B* **2007**, *76*, 245417.
[25] F. D. Angelis, M. Malerba, M. Patrini, E. Miele, G. Das, A. Toma, R. P. Zaccaria, E. D. Fabrizio, *Nano Lett.* **2013**, *13*, 3553.
[26] C. Huang, J. Ye, S. Wang, T. Stakenborg, L. Lagae, *Appl. Phys. Lett.* **2012**, *100*, 17.
[27] E. M. Larsson, J. Alegret, M. Käll, D. S. Sutherland, *Nano Lett.* **2007**, *7*, 1256.
[28] A. Dmitriev, C. Hägglund, S. Chen, H. Fredriksson, T. Pakizeh, M. Käll, D. S. Sutherland, *Nano Lett.* **2008**, *8*, 3893.
[29] M. A. Otte, M. C. Estévez, L. G. Carrascosa, A. B. González-Guerrero, L. M. Lechuga, B. Sepúlveda, *J. Phys. Chem. C* **2011**, *115*, 5344.
[30] M. S. Schmidt, J. Hübner, A. Boisen, *Adv. Mater.* **2012**, *24*, OP11.
[31] K. Wu, T. Rindzevicius, M. S. Schmidt, K. B. Mogensen, S. Xiao, A. Boisen, *Opt. Express* **2015**, *23*, 12965.
[32] K. Lilienthal, M. Stubenrauch, M. Fischer, A. Schober, *J. Micromech. Microeng.* **2010**, *20*, 025017.
[33] D. A. Zeze, D. C. Cox, B. L. Weiss, S. R. P. Silva, *Appl. Phys. Lett.* **2004**, *84*, 1362.
[34] E. Hein, D. Fox, H. Fouckhardt, *Surface Coatings Technol.* **2011**, *205*, S419.
[35] Y. Shen, J. Zhou, T. Liu, Y. Tao, R. Jiang, M. Liu, G. Xiao, J. Zhu, Z.-K. Zhou, X. Wang, C. Jin, J. Wang, *Nat. Commun.* **2013**, *4*, 2381.
[36] Innergie Technologies, Inc.
[37] Alcatel SCM 600 E-beam and sputtering deposition system.
[38] Advanced Oxide Etcher: STS MESC Multiplex ICP.
[39] Zeiss Supra VP 40 SEM.
[40] COMSOL Inc.
[41] P. B. Johnson, R. W. Christry, *Phys. Rev. B* **1972**, *6*, 4370.
[42] I. H. Malitson, *J. Opt. Soc. Am.* **1965**, *55*, 1205.
[43] Shimadzu, UV-1800 UV-Vis Spectrophotometer.
[44] Sigma Aldrich.
[45] BrixChart.
[46] Millipore Corporation, Billerica, MA, USA.

Received: July 12, 2016
Revised: August 29, 2016
Published online:

DOI: 10.1002/smll.201602299

Supplementary Information
Lithography-Free Fabrication of Silica Nanocylinders with Suspended Gold Nanorings for LSPR-Based Sensing

Anil Haraksingh Thilsted Jesper Yue Pan Kaiyu Wu
Kinga Zor Tomas Rindzevicius
Michael Stenbæk Schmidt
Anja Boisen

Department of Micro- and Nanotechnology
The Technical University of Denmark
2800 Kongens Lyngby, Denmark

Email: anja.boisen@nanotech.dtu.dk

June 28, 2016

1 LSPR Tuning with Metal Thickness

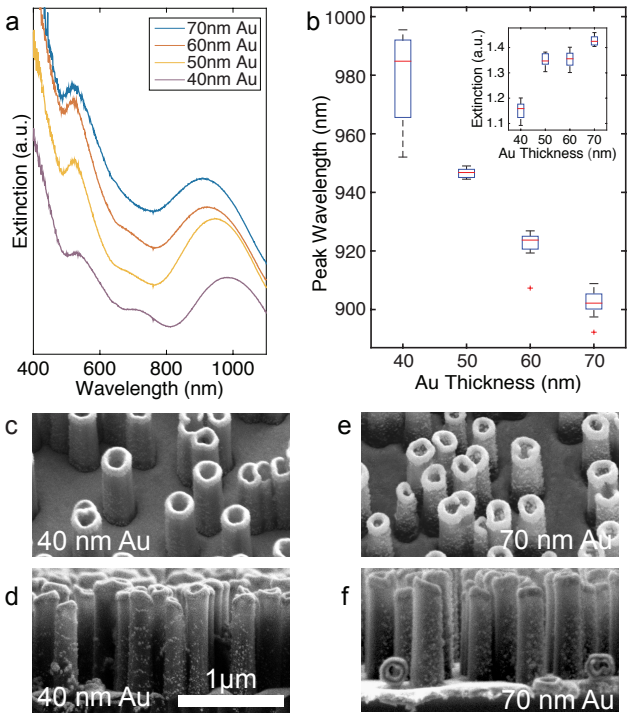

Figure 1: (a) Representative extinction spectra of nanocylinders coated with increasing thicknesses of gold. A peak between 900 nm and 1000 nm was observed. (b) The peak position decreased linearly, and the extinction increased with increasing gold thickness. (c-d) SEM micrographs of nanocylinders with 40 nm and (e-f) with 70 nm of gold.

Metal thickness was varied on nanocylinders with extinction spectra revealing a plasmonic absorption peak between $\lambda = 900$ nm and $\lambda = 1100$ nm as well as a second peak at around 500 nm. These nanocylinders had a density of 5.7 μm^{-2}, a height of 1 μm and a diameter of 300 nm. The absorption wavelength decreases linearly from 979 nm to 902 nm as the gold layer thickness increased from 40 nm to 70 nm. Due to a thicker metal layer, the extinction increased from 1.15 a.u. to 1.43 a.u.. While a metal thickness of 50 nm resulted in an absorbance peak with a mean peak at half prominence of $\Delta\lambda_{(50\text{ nm Au})} = 194$ nm, the peak prominence of 0.190 a.u. was significantly higher than for the other metal thicknesses which had a mean prominence of 0.11 nm. For this reason, a metal thickness of 50 nm was chosen for subsequent investigations.

2 Nanocylinder Diameter and Height Variation

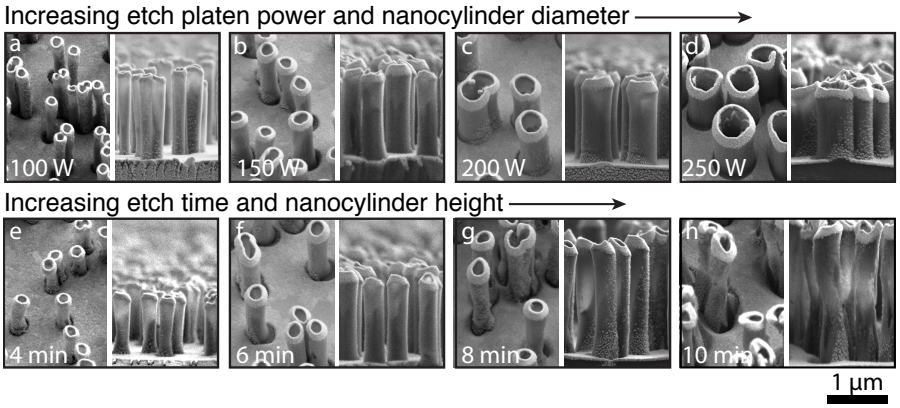

Figure 2: (a-d) SEM micrographs at 65° and 0° tilt, showing increasing nanocylinder diameters for increasing etch platen power and (e-h) increasing nanocylinder heights for increasing etching time.

Figure 2 shows SEM micrographs of nanocylinder with all the achieved heights and diameters with a 50 nm gold layer. The results show the ability to control the height and width at a sub-micron scale, allowing for tuning the LSPR peaks.

3 Buckling and Concentric Nanocylinders

It was observed that within nanocylinders with a large diameter, there were structures that resembled inner nanocylinders. These nanocylinders within nanocylinders resulted in concentric multi-ring structures. Deposition of metal resulted in plasmonic structures that could potentially show an increased tunability compared to single-ring structures due to their higher degrees of freedom compared to single-ring structures [1]. It was also observed that for longer etching times ($>$ 16 min), buckling of structures occured, potentially setting an upper limit for nanocylinder heights for certain etch parameters. Multi-ring structures and buckling nanocylinders are shown in Figure 3.

4 LSPR Peak Position Calculation

LSPR peak positions were calculated by first guessing a position using MatLab's `findpeaks` function. Data window sizes from 25 nm to 225 nm were defined around this peak and each data crop was fitted to a quadratic function. Each fit was evaluated for the adjusted r^2 value, and the best fit was chosen in order to determine peak position. Plots of the quadratic fit to raw data as well as

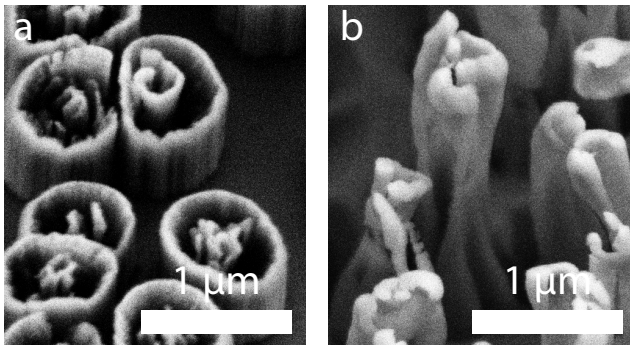

Figure 3: (a) Nanocylinder structures forming within nanocylinders with large diameters, potentially allowing for concentric multi-ring structures for increased plasmonic tunability. (b) Deterioration and buckling observed for tall nanocylinders etched for a longer time, potentially setting a maximum limit to nanocylinder height.

the relation between the window size, adjusted r^2 value, and calculated peak position are shown in Figure 4.

5 Aqueous Solution Experimental Setup

Immersion and incubation in solutions of the LSPR substrate were necessary in order to carry out bulk and surface RI sensing measurements. For these experiments, the substrate was diced into pieces that fitted into a standard 2.5 mL cuvette[1]. A 3D printed blocker with a small window was used to ensure that all measured light passed through the LSPR substrate. Baseline measurements were carried out using the cuvette and the blocker but no LSPR substrate. The experimental setup is sketched in Figure 5.

References

[1] Peter Nordlander. The Ring: A leitmotif in plasmonics. *ACS Nano*, 3(3):488–492, 2009.

[1] Aireka Cells

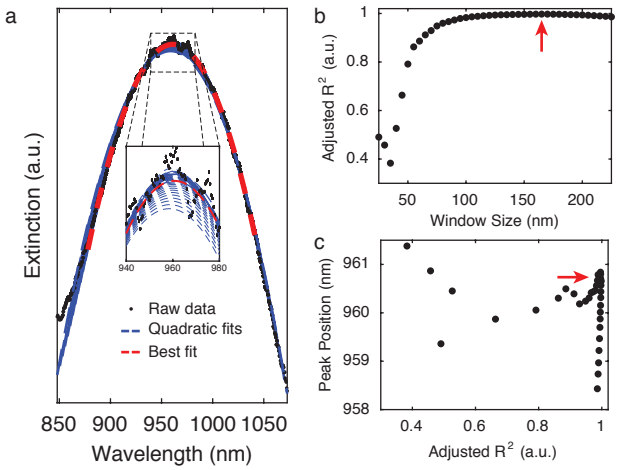

Figure 4: (a) Plot showing an example of raw data for an extinction measurement and the quadratic function used for fitting and finding the peak position around the position that MatLab determines. Different window sizes from 25 nm to 225 nm were used, and the fit with the best adjusted r^2 is plotted. (b) The window size vs the adjusted r^2 value showing an optimum (red arrow). (c) The calculated peak position versus the rsquared value, showing a clear trend towards the most correct value (red arrow).

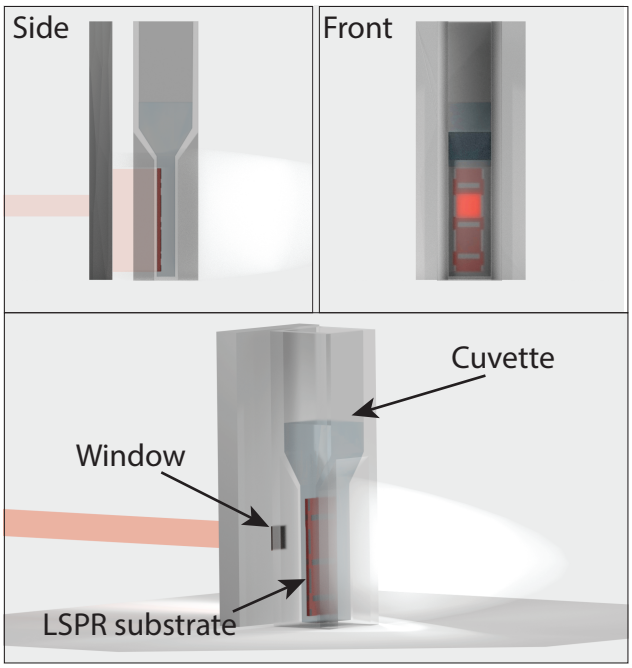

Figure 5: A sketch of the experimental setup used for LSPR measurements in aqueous solutions. A diced substrate is immersed and fastened to the inner wall of a cuvette. A light blocker with a window is used to ensure that all light passes through the LSPR substrate.

Appendix

Patent Application

A SUBSTRATE AND A METHOD OF USING IT

The present invention relates to a substrate suitable for identifying substances or quantifying parameters thereof, such as using SERS measurements or the like. Also, the invention relates to methods of using the substrate for identifying these and/or quantifying such parameters. The substrate is very versatile and may be used for both transmissive and non-transmissive set-ups.

Technologies of this type may be seen in US2012/0273662, US2013/330710, US2013/040862, US8339597, US84155640, US2014/015548, US2012/081703, WO13/130043, WO 2013/154770 A1, EP 2 884 265 A1, and US 2011/128526 A1.

A first aspect of the invention relates to a substrate comprising a base having a first surface part and a plurality of elongate elements extending away from the substrate and from the first surface part, wherein:

- the base and elongate elements are transparent at at least a first predetermined wavelength, the elongate elements having a height of 40 nm - 5 μm and a width of 5-1500 nm; the elongate elements being positioned with a distance/spacing of 1nm-8μm,

- the elongate elements have a tip of a first material, being an electrically conducting material and/or semiconductor material, the tip having a height of 20-1000 nm and in a direction at least substantially perpendicular to an axis of the pertaining elongate element, a width of 20-1000nm,

- a layer of a second material, being an electrically conducting material and/or semiconductor material, the layer being provided on the first surface part, the layer having an upper plane and a thickness of 5-1000nm, a bottom of the tips being 2-3000 nm above the upper plane;

- a gap or cavity existing between the layer and the elongate elements, the gap being 1-500nm wide.

In the present context, a substrate may be any type of element. The substrate may be made of any material or combination of materials. The substrate has, due to the elongate elements with metallized tip(s) and the layer, a surface which may be used for e.g. SERS measurements. This is described further below.

In the present context, the base preferably is a plane base, as this is the easiest base to provide the elongate elements on. However, the base may have any shape or thickness and may be made of any material. In e.g. SERS measurements, the base has virtually no influence, so the construction of the base is, in that respect, not important. The base, however, is transparent.

The first surface part is an outer surface part of the base. This surface may be plane (apart from the elongate elements extending therefrom), bent/curved or the like. If the base is slab-shaped, the first surface part may be one of the surfaces, such as one of the major surfaces, of the base.

In the present context, an elongate element is an element which has a longest dimension, along a longitudinal axis, extending away from the base. Preferably, all elongate elements extend away from the base in at least substantially the same direction. Preferably, this direction is perpendicular to the first surface part, at least at the position where the individual elongate element is attached to or engages the base. "Extending away from" will mean that there is a non-zero angle between a longitudinal axis of the individual elongate element and the first surface part at the position thereof from which the elongate element extends. This angle preferably exceeds 10°, such as exceeding 20°, such as exceeding 45°, such as exceeding 70°such as exceeding 80°. In many embodiments, the elongate elements are at least substantially perpendicular to the base. The elongate element has a thickness perpendicular to the longitudinal axis.

It is noted that the elongate elements may be provided on or attached to, such as fixed to or grown on, the base or may have been made by removing material from an initial substrate, so that the base and elongate elements are one monolithic element. Alternatively, the base and elongate elements may be of different materials and may be made in different processes, such as by firstly providing the base and subsequently providing the elongate elements on the base.

Preferably more than a single elongate element has a tip of the first material. Actually, preferably at least 10%, such as at least 30%, preferably at least 50%, such as at least 75%, preferably at least 90%, such as at least 99% of the elongate elements have a tip of the first material.

Any number of elongate elements may be used. In fact, usually the number of elongate elements is defined not by the number thereof but the density thereof on the first surface part.

In this context, a tip is a surface at least substantially covering a part of the elongate element, which part is the farthest from the base along the longitudinal axis. The tip needs not cover any part of the elongate element between the farthest part and the base. However, depending on the thickness and manner of deposition of the tip, 1% or more, such as 2% or more, such as 5%, 10%, 20%, 40% or more of the length of the elongate element, between the base and the farthest part, may be covered by the tip. The tip may be an even layer or an uneven layer on the elongate element.

Even though it is desired that the tip of an elongate element fully covers the farthest part, production imperfections may occur whereby a percentage of the farthest part is not covered.

It is noted that the tip of each elongate element preferably is separate from the tips of other elongate elements. Thus, each tip is able to move independently of others, at least before the below mentioned leaning.

The tips or at least a part thereof have, in a direction at least substantially perpendicular to an axis of the pertaining elongate element, a width of 20-1000nm, such as 30-500nm, preferably around 400nm and a height of 20-1000 nm, such as 100-800nm, such as around 400nm. Preferably, a layer thickness of the first material of the tip is 5nm or more, such as 10nm or more, preferably 25nm or more, such as 40nm or more. In one situation, the layer thickness is no more than 35%, such as no more than 30%, preferably no more than 25%, such as no more than 20% of a mean distance/spacing between elongate elements at the base. In this situation, the tips are separate and may move independently of each other.

In the present context, the base and/or elongate elements are transparent, when a layer of 100nm of the material forming the base/elongate element transmits at least 10% of radiation at the first wavelength. The first wavelength may in principle be a very narrow waveband and may be any wavelength of radiation. Preferably, however, the first wavelength is a waveband of a width of at least 50nm, such as within the UV-NIR regime (300-1500nm), within which the base/elongate elements are transmissive.

The tips are made of a first material being an electrically conducting material and/or semiconductor material. The layer is made of a second material also being an electrically conducting material and/or semiconductor material. The first and second materials may be identical or not. The first and second materials may have the same or different properties, such as different electrical conductivity, if desired. In this connection, an electrically conducting material preferably is a metal, such as Cu, Ag, Au, Pt, Pa or Al, but in principle, an electrically conducting material may be used, such as also TiNi. It is noted that the tips may be made of a single, solid material or a sandwich comprising a layer of the above conducting

material which may be covered with a passivating layer, such as a layer of Al2O3, TiO2, SiO2, glass or the like.

The layer is provided on the first surface part with a thickness of 5-1000nm, such as 100-500nm, preferably around 200nm. The layer has an upper plane, the upper plane being 2-3000 nm below a bottom of the tips.

Preferably, the gaps/cavities exist between the layer and the elongate elements. Preferably, the gaps are 1-500nm wide. An advantage of the presence of the gap/cavity is that radiation may travel from below the layer, between the elongate elements and the layer, to above the layer, such as to the tips or substances provided thereon. Thus, compared to a standard SERS substrate, a more versatile substrate is obtained which may be used for a wider variety of measurements and set-ups.

The layer preferably covers at least 50% of the parts of the first surface part excluding the elongate elements and the gaps/cavities (when provided between the layer and the elongate elements), as the layer then also facilitates additional types of measurements compared to standard SERS substrates. In particular, the cavities/gaps may make LSPR and transmissive SERS measurements possible even when the layer and tips are relatively thick and non transparent.

In one embodiment, the base and elongate elements are a monolithic element. In this manner, no interface, such as a difference or variation in refractive index, exists between the base and one or more elongate elements. Changes in refractive index may cause reflection of the radiation and may thus prevent transmission of radiation from the base to the elongate elements or vice versa.

In a preferred embodiment, the base and/or elongate elements is/are made of, or at least comprise(s) mainly, fused silica. Other relevant materials for the base and/or elongate elements are SiO2, Al2O3, TiO2, carbon, and polymers such as PMMA, SU-8, polycarbonate or the like.

In one embodiment, each of the base and elongate elements is/are made of a material transmitting, through a thickness of 0.5mm, at least 20% of radiation in a waveband, including the first wavelength, having a width of at least 100nm and being within the wavelength interval of 100nm-1.3μm. This transmission preferably is present for all wavelengths in the waveband. Preferably, the material(s) of the base and elongate elements transmit(s) more than 20% of incident radiation, such as in a 200nm wavelength range in the UV-NIR regime (300-1500nm) through a 0.5mm thick sample.

The first and/or second materials may be selected from the group consisting of: Ag, Au, Pt, TiNi, Pa, Al, Cu, a group III-V material and/or a semiconductor material.

Preferably, the elongate elements have a height, in a longitudinal direction thereof, of 40nm-5µm, such as 50-400nm, such as 75-300 nm. One, more or all elongate elements may have a height, along a longitudinal direction thereof, such as at least 40nm, preferably at least 50nm, such as at least 100nm, preferably at least 200 nm, such as at least 400, 500, 600, 700, 1000, 1200, 1400 or 1600 nm.

In one situation, an elongate element, or preferably more than 10, 20, 30, 40, 50, 60, 70, 80, 90 or 95% of the elongate elements, preferably has/have a height being at least 2 times a mean spacing between the elongate elements. The mean spacing may be determined from the density of elongate elements, such as by assuming that the elongate elements are positioned in a perfect pattern on the base, such as in straight columns and rows.

Preferably, a majority of the elongate elements, i.e. at least 50%, such as at least 60%, preferably at least 70%, such as at least 80%, preferably at least 90% or 95% of the elongate elements, have a height within 20%, such as within 10%, preferably within 5%, of a mean height of the majority of the elongate elements. In this manner, the tips will be within at least substantially the same height also when leaning (see below). If the tips are positioned in at least substantially the same plane, it will be easier to e.g. focus a laser beam thereon when performing a measurement. In addition, when the tips are in at least substantially the same height before leaning, the leaning tips will form hotspots as opposed to a tip leaning against a part of an elongate element with no metal surface.

Preferably, the elongate elements have a width, perpendicular to a longitudinal direction thereof, of 5-1500nm, such as 5-500nm, such as 5-50nm. This width may be a width of the elongate element not including the tip, which normally is wider. The width may be a mean width or largest width at any longitudinal position or e.g. at the centre/middle thereof, excluding the tip and/or the first material.

In that or another situation, an elongate element, or preferably more than 10, 20, 30, 40, 50, 60, 70, 80, 90 or 95% of the elongate elements, has/have a ratio between a height along the longitudinal axis thereof and the width thereof of at least 5, such as at least 6, at least 7, at least 8, at least 9, at least 10, at least 15 or at least 20.

In the below-mentioned leaning condition, it is desired that the elongate elements are able to firstly lean and secondly bend at a well defined position. Clearly, if one elongate element bends or primarily bends at the base and the other no more than 10% from the tip,

formation of groups of tips will differ. Leaning at e.g. the base or close to the base will give the elongate element a longer "range" to form a group with other tips.

In one embodiment, the elongate element, or preferably a majority of the elongate elements, such as at least 50%, 60%, 70%, 80%, 90% or at least 95% of the elongate elements, has/have a neck portion, the tip having a larger cross section, perpendicular to the longitudinal direction, than the neck portion which is positioned closer to the base than the tip, a mean width, also in the perpendicular direction, of the neck portion being no more than 80%, such as no more than 75%, such as no more than 70%, preferably no more than 65%, such as no more than 60%, 55% or 50%, of a mean width of the tip or the width of the elongate element.

Defining or providing a neck portion will aid in providing a well defined bending point or a point where an overall part of the bending takes place. Preferably, this neck portion is positioned far from the tip portion in order for the part of the elongate element between the neck portion and the tip to be as long as possible.

In that or another embodiment, at least one elongate element, but preferably each of at least 10%, 20%, 30%, 40%, 50%, 60%, 70%, 80%, 90% or at least 95% of the elongate elements, has/have a spring constant of no more than 250 N/m, such as no more than 100N/m, preferably no more than 50N/m, such as no more than 20N/m. An estimate of a 100nm diameter 600 nm tall Si pillar is about 12.3 N/m.

In that or another embodiment, at least one elongate element, but preferably each of at least 10%, 20%, 30%, 40%, 50%, 60%, 70%, 80%, 90% or at least 95% of the elongate elements, is/are bendable, so that providing a force to the tip thereof, the force being perpendicular to the longitudinal direction, of no more than 20 μN, will make the tip move at least 50% of a height of the elongate element along the longitudinal direction, in a direction perpendicular to the longitudinal direction.

The low force makes the formation of groups possible without the risk of breaking the elongate elements, if they are too stiff.

In a particularly interesting embodiment, a number of the elongate elements lean or bend. In this situation, a plurality of groups of elongate elements exist, the tips of the elongate elements of each group being positioned within a distance of 20nm or less, such as at least 15nm, such as at least 10nm, such as at least 5nm, from each other.

In this context, a group of elongate elements is a number of elements having a tip being within 20nm of a tip of another elongate element in the group.

It has been found that these groups of tips are especially efficient in e.g. SERS. Thus, it is desired to have as many groups or especially as many tips form part of a group as possible.

Thus, preferably, at least 25%, such as at least 35%, preferably at least 50%, such as at least 75%, of the elongate elements each form part of a group with at least 3 elongate elements.

It is clear, especially in the leaning situation, that the density of elongate elements, the sizes of the tips when covered by metal, the bendability of the elongate elements as well as where, along their lengths, the elongate elements bend, will determine the ability of forming of groups of tips.

In one embodiment, the elongate elements are positioned with distance/spacing of 30-300nm, such as 1-200nm.

The elongate elements may be positioned randomly on the base. An advantage of this may be that the production method may be cheap so that the product price may be low.

Alternatively, the elongate elements may be positioned periodically on the base. The advantage of this is that there may be a strong inter-coupling between modes on the tips and the layer at the surface of the substrate.

However, it is preferred that the elongate elements are positioned, on the substrate, with a density of no more than $4x10^9$ tips per cm^2, such as no more than $3x10^9$ tips per cm^2, such as no more than $2x10^9$ tips per cm^2, as a too high density may make individual metallization of the tips difficult.

Naturally, if the area of the substrate or base at which the elongate elements are positioned is less than $1cm^2$, the density may be determined for smaller areas. One manner of determining the density is to outline a surface from which the elongate elements extend, determine the area thereof and determine the number of elongate elements therein, such as the number of elongate elements which, within the area, contact, engage, are attached to, are fixed to or otherwise touch the base/substrate within the area. Below, a substrate is described which has elongate elements which bend. In this situation, the tips of elongate elements may extend outside of the area, but the elongate elements still extend from within the area.

In one embodiment, the distance between the layer and the bottom of one or more tip(s) is/are 100-2000nm, such as around 200nm. As mentioned above, the gaps allow radiation to pass from below the layer to the tips (or vice versa). On the other hand, the gaps should be sufficiently small to allow coupling between tip modes and layer modes. The gap(s)/cavity(ies) between the layer and one or more elongate element(s) is/are 1-500nm wide. As mentioned above, the gaps, combined with the transmissive base and elongate elements, allow radiation to pass through the base from one side of the layer to the other.

Preferably, the gap(s)/cavity(ies) between the layer and one or more elongate element(s) prevent(s) electrical connection between the layer and the tip(s) of the pertaining elongate element(s). Naturally, the function of the gaps/cavities may be altered or altogether destroyed by too much electrically conducting material provided on one or more elongate elements in positions other than at the tips and/or on the base in the cavities/gaps, if such cavities/gaps exist between the layer and the elongate elements. Thus, it is desired that any electrically conducting material positioned on the elongate elements, and not on or at the tips, and/or in gaps/cavities on the base, such as below the bottom of the tips, has a thickness of no more than 15% of a layer thickness of the layer of the tips. Preferably, any layer of such conductive material has a thickness of no more than 50nm.

Preferably, the layer has a thickness, such as a mean thickness, of 100-500nm, such as around 200nm. This thickness may support SPR modes in the layer. The distance between the upper plane of the layer and the bottom of the tips may be 100-2000nm, preferably around 200nm.

In yet another aspect of the invention, the elongate elements may have a height, in a longitudinal direction thereof, of 20-1000nm, such as 30-500nm. One, more or all elongate elements may have a height, along a longitudinal direction thereof, of at least 30nm. The elongate elements may be positioned with a density of $15.6*10^5$-$25*10^{12}$ elongate elements per cm^2 (corresponding to a spacing between centre lines of elongate elements by 20-8000nm). The usual density is approximately $1.0*10^9$ elongate elements per cm^2. The tips or at least a part thereof have, in a direction at least substantially perpendicular to an axis of the pertaining elongate element, a width of 5nm - 2µm. The layer may have a thickness, such as a mean thickness, of 5-1000nm, such as 50-500nm, such as 100-300nm.

In a particularly interesting embodiment, the elongate elements are tube-shaped elements. These elements have the further advantage that additional plasmonic resonances may be seen. With elements of this type, resonances may be seen both in the longitudinal direction and circumferentially

The elongate elements may be solid so as to have, in a cross section perpendicular to the longitudinal axis, no hollowness or cavities. On the other hand, the cross section may comprise a hollowness, so that the elongate elements, or some thereof, are tube shaped elements. These tube shaped elements are elements extending from the base but which have an outer wall and an inner cavity, which often is open at the other end of the tube shaped element than that at which it engages or touches the base. Preferably, the tube shaped element has the same cross section or at least substantially the same cross sectional shape along a length thereof. This cross section may be an outer shape being circular, square, triangular or any other, regular or irregular shape, and the hollowness or inner channel thereof may have any cross section, which preferably is the same shape as the outer shape of the tubular element so that the wall thickness of the tubular element is at least substantially the same around the cavity in the cross section. Production imperfections naturally may occur.

The tube shaped element will have a tip which is provided on an upper part of the tube shaped element. This upper part or edge may be more or less parallel (exist in a plane parallel) to a plane of the surface. The tip may be made of any of the above materials and preferably covers at least an upper edge of the tube shaped element. The material may additionally cover at least a part of an outer surface of the tube shaped element from the upper edge and toward the base and at least a part of an inner surface of the tube shaped element from the upper edge and toward a bottom of the cavity thereof.

A thickness of the layer of the tip may vary along the tube shaped element and may reduce in size from the upper edge and toward the base. The thickness of the layer on the outer walls may be 0-500nm, such as 10-100nm, preferably around 20nm. Preferably, the thickness of the metal layer on the upper surface/edge of the walls is 10-200nm, preferably around 100nm.

The cavity/gap exists between the layer and the tip material. As the tip material does not extend to the base or layer, the gap/cavity extends along a portion of the longitudinal direction of the tube shaped element. When the cavity is provided on the surface, i.e. between the tube shaped element and the layer, the overall cavity diameter or length may be 20-2000nm, such as 100-1000nm, preferably around 600nm.

Preferably, the tube shaped element has a height, along the longitudinal axis from a plane, for example, of the base, to the upper edge, 10-4000nm, such as 100-2000nm, such as 300-1000nm, preferably around 500nm. The outer circumference of the tube shaped element, such as in a plane perpendicular to the longitudinal axis, may be 60-9000nm, such as 250-4000nm, such as 1000-2000nm. If the tube shaped element has a circular cross section, the

diameter of the tube shaped element 140 may be 10-1500nm, such as 200nm. The circumference of the cavity or the inner circumference of the wall, in the cross section, of the tube shaped element may be 30-9000nm, such as 300-3000nm, such as 200-2000nm. If the cavity is circular in cross section, the inner diameter of the of the tube shaped element 140 may be 5-1500nm, such as 100-1000nm, such as 150-500nm, preferably around 170nm.

A formation or portion of a material suitable for use on the tips may be provided on the bottom of the cavity, where a gap may be provided between this formation/portion and the inner walls of the tube shaped element. This gap may be 0-400nm, such as 2-100nm, such as 3-50nm, such as 4-10nm, preferably around 5nm. Alternatively, the formation/portion may extend to the walls where a gap may exist between the material of the formation/portion and the material of the tip, so that any tip material provided on the inner wall of the tube shaped element does not extend to the formation/portion.

A spacing between neighbouring tube shaped elements may be 10-5000nm, such as 100-2000nm, such as 200-1000nm, preferably around 400nm.

Another aspect of the invention relates to a method of identifying a substance, the method comprising the steps of:

- providing a substrate according to the first aspect of the invention,

- providing the substance on the tips and layer of the substrate,

- launching first radiation comprising radiation of a second predetermined wavelength toward the substance,

- detecting second radiation output from the substance at a third predetermined wavelength, the second and/or third wavelength being identical to the first wavelength,

- identifying the substance from the detected second radiation.

In this context, the substance may be any type of substance, such as explosives, chemicals, hormones. Any type of molecule can in principle be identified and, if desired, quantified.

The providing of the substance on the tips and layer may be performed by bringing the substance on a liquid or gas form, such as by adding the substance to, such as dissolving the substance in a liquid.

In a particular embodiment, the substance is applied to the substrate in liquid form and allowed to dry. Due to the small dimensions of the cavities/gaps, liquid may still be present here when other parts of the substrate are dry, so that the measurement and thus the identification may be made while the substance is on liquid form without liquid interfering with the other parts of the substrate and to the radiation at other positions than in the cavities/gaps. In fact, situations may exist where the substance in the liquid is up-concentrated in the gaps/cavities due to e.g. evaporation of parts of the liquid at other parts of the substrate.

When the step of providing the substance on the tips and layer comprises delivering a liquid to the substrate, an evaporation of the liquid from the substrate may bring about the above- and below-mentioned leaning of the elongate elements.

The second radiation is output from the substrate. This "outputting" will depend on the relationship between the wavelength of the second radiation and the properties of the substance. This may be radiation relating to a vibration of the molecule, scattered radiation, transmitted radiation or the like. Different types of set-ups are now possible. Radiation (white light, a selected wavelength, focused on a small area, flood lighting the whole substrate or a larger area) may be provided from the tip side (or the opposite side of the layer and base) of the substrate to interact with the substrate in the vicinity of the tips/layer/cavities. The resulting radiation (scattered, reflected, unabsorbed) may be collected from the same side of the base or from an opposite side of the base.

For example, in SERS measurements, a laser is focused on to a portion of the substrate and the substance is identified from the resulting scattering spectrum. This spectrum may be determined from radiation directed back toward the direction of arrival of the laser beam or may be received from an opposite side of the substrate.

In SPR, the radiation (could be laser radiation or a broader spectrum) is directed into the base from different angles, and the resulting radiation may be received also from the base and determined as a function of angle of receipt in relation to a plane of the base. The radiation may also be received from the opposite side of the base.

In a preferred embodiment, the second radiation is formed by the first radiation being scattered by the substance.

The detection of the second radiation may be a standard detection of the wavelength, such as a spectrum, of the second radiation and/or an intensity thereof.

The identity of the substance may be determined from known spectra, also known as fingerprints, of known substances. Often, substrates of this type are used for identifying a substance the contents of which are not known.

Quantification of a substance from a spectrum thereof is a well-known procedure.

A major advantage of the present substrate is that it may be used for different types of measurements. In fact, the same substrate may be used in a sequence of different set-ups so that it is ascertained that the measurements are performed on the same substance. Providing a substance on a series of different substrates always entails the risk that one substrate is contaminated or provided with another or a slightly different substance or concentration thereof than another, so comparison may not be possible.

It is preferred to adapt the substrate to the substance to be identified. Different substances have different vibration modes and thus will excite different resonances in the substrate. Thus, the dimensions of the substrate may be chosen so as to enhance the resonances brought about by a particular substrate, or the dimensions may generally be selected for supporting resonances in a particular frequency interval. A suitable substrate may then be selected when looking for a particular substance, the frequencies of which are known.

The dimensions having an effect on the supported or enhanced resonances are the distances between the tips and the layer, the tip dimensions, the tube diameter, the tube height, the gap/cavity dimensions but also the layer thickness and the materials selected for the tips and layer.

Naturally, the dimensions and materials may also be tuned to the laser wavelength used in some types of measurements.

In one embodiment, the first and/or the second radiation travels, during the launching step, through at least one gap/cavity. In this manner, a transmission type measurement may be performed where the first radiation is fed to one side of the layer (either from the side with the elongate elements or from the opposite side through the base) and the second radiation is received from the other side of the layer.

Thus, in one situation, during the launching step, at least part of the first radiation is launched toward the substance through the base.

In addition or alternatively, during the detecting step, at least part of the second radiation travels through the base (and additionally or optionally the elongate elements) before detection thereof.

The set-ups using the above tube-shaped elements may be the same as the ones usually used for solid, elongate elements with tips.

In the following, preferred embodiments of the invention will be described with reference to the drawing, wherein:

- figure 1 illustrates, in a cross section and from the side, a substrate according to a first embodiment of the invention,

- figure 2 illustrates a first measuring set-up using a substrate according to the invention,

- figure 3 illustrates a second measuring set-up using a substrate according to the invention, and

- figure 4 illustrates, in a cross section and from the side, different embodiments of tube-shaped elongate elements.

In figure 1, a part of a substrate 10 is illustrated having a base 12 and a number of rods or elongate elements 14 extending from a surface 121 of the base and each having a metal tip 16. On the surface 121, a metal layer 18 is provided and it is seen that a cavity 20 is provided between the rods 14 and the layer 18, the cavity 20 having a minimum distance or width d of 1-500nm. Alternatively, the layer 18 may extend all the way to the rod 14, where a cavity 20' is then present between the layer 18 and the tip 16.

The base 12 and rods 14 are transparent to at least a predetermined first wavelength but usually are made of e.g. glass or fused silica and thus are transparent within a wavelength interval.

This substrate 10 is well suited for many types of analysis, such as analysis based on SERS, and where the substance to be analysed is provided on the substrate and thus on and between the metal tips 16 and the metal layer 18.

Naturally, the substrate may be manufactured in a number of manners and the dimensions thereof may be optimized to different purposes.

The rods 14 may be made of a transparent core having a height (λ) of 40nm to 5μm and a diameter or width (κ) of 5-1500nm, such as from about 5nm to about 500nm, such as from 5-50nm. The tip 16 may be formed by a coating with a thickness of 0.1-1000 nm, such as 5-500nm, usually including a SERS-active material, which may be conductive or a semiconductor, such as, for example, gold, silver, copper, platinum, NiTi, palladium, aluminium, or any other material, such as III-V material or other semiconductors, that will enhance the Raman scattering of photons by analyte molecules positioned adjacent thereto. It may be advantageous that the tips 16 and/or layer 18 have a rough surface.

The tips may have a height (β) of 20-1000nm, such as 100-800nm, such as around 400nm and a width (ψ) of 20-1000nm, such as 30-500nm, preferably around 40nm.

The film may have a thickness (η) of 5-1000nm, such as 100-500nm, preferably around 200nm, and a distance (Σ) between the upper plane of the film and the bottom of the tips may be 2-3000nm, such as 100-2000nm, preferably around 200nm.

Each rod 14 of the plurality of rods 14 may be separated from adjacent rods 14 by a distance/spacing (ρ) of between about 1 nm and about 8μm, such as between about 30 and about 300 nm or about 1-200 nm. This distance may be a distance between surfaces of the rods, a core there of, the tips thereof or from centres of the rods.

It may be desired that the distance separating each rod from adjacent rods is selected to correspond to the size of a particular analyte molecule to be analyzed with the SERS-active structure. In general, the predetermined distance may be selected to correspond to the size of a particular analyte molecule to be analyzed with the, then, SERS-active structure, such that the molecule is capable of draping between two adjacent rods, part of the molecule being adsorbed on a first rod and another part of the molecule being adsorbed on a second, adjacent rod. Such a configuration has been shown to significantly enhance the Raman signal emitted by the analyte molecule.

A particularly interesting embodiment is one, as is also described in WO2011/047690, wherein the substrate comprises clusters of rods leaning toward each other with a distance between tips of on the order of 0-10nm. As mentioned above, these clusters or close inter-tip distances lead to increased sensitivity.

The substrate may be made of any transparent material. Transparent is regarded as being able to transmit more than 20% light in a 200nm wavelength range, preferably in the UV-NIR regime (300-1500nm), through a 0.5mm thick sample of the material. Examples of suitable materials for the substrate is glass, polymers, fused silica, Al_2O_3, SiO_2, TiO_2, carbon and polymers, such as polycarbonate, PMMA, SU-8 and the like.

The rods may be made of the same material as the substrate or may be made of a different material. Especially when the rods and substrate are made of the same material, an interface may be avoided between the base of the rods and the substrate. This interface may generate a difference in refractive index and may thus affect the propagation of the light/radiation within the substrate and rods.

The cavities preferably provide an electrical insulation between the layer and the tips. The cavities preferably have significantly less metal/semiconductor than the layer and/or tips, so that no significant electrical connection exists between the surrounding conducting film and the tips.

The cavity may have a width (Ω) of e.g. 10-1800nm, preferably 80nm. This width may be selected on the basis of the electrical conduction between the tips and layer. The lower a conduction obtained, the smaller can the cavity be selected.

In figure 4, different embodiments of an alternative type of substrate are illustrated wherein, on the base 12, a number of tube shaped elements 140 are illustrated (in a cross section with the inner surfaces illustrated in hatched lines).

In figure 4a, the tube shaped elements 140 are illustrated on the base 12 with the layer 18 provided on the surface 121 and between the elements 140. Preferably, the tube shaped elements 140 have a circular cross section. The tube shaped elements 140 are provided with a coating or tip 160 of a conductive material. This material covers the outer side of the walls of the tube shaped element 140 as well as the top thereof and the inner surfaces, where the layer thickness, as can be seen, is lower. At the bottom of the tube shaped element 140, formations 180 are provided also of a conductive material. A way of producing the tube shaped elements 140 is described below. The providing of the layer 18, the tips/coatings 160 and the formations 180 may take place during the same metallization process.

The materials suitable for the tube shaped elements 140 and the layer 18, tips/coatings 160 and formations 180 are as those described above.

Preferably, the height, λ, is 10-4000nm, such as 100-2000nm, such as 300-1000nm, preferably around 500nm. The outer diameter, K, of the tube shaped element 140 may be 10-1500nm, such as 200nm. The inner diameter, α, of the of the tube shaped element 140 may be 5-1500nm, such as 100-1000nm, such as 150-500nm, preferably around 170nm.

The thickness, η, of the layer may be 2-1000nm, such as 100-500nm, preferably around 200nm.

When the cavities 20 are provided on the surface 121, the overall cavity diameter or length, Ω, may be 20-2000nm, such as 100-1000nm, preferably around 600nm.

Alternatively, the layer 18 may extend to the tube shaped element 140, where the coating 160 of the outer walls is then provided so that it starts at a position above the upper surface of the layer 18 so that a cavity is provided between the layer and the coating 160.

The thickness, Σ_1, of the layer thickness on the outer walls of the elements 140 may be 0-500nm, such as 10-100nm, preferably around 20nm, and the gap ω, between the inner wall and the formation 180 may be 0-400nm, such as 2-100nm, such as 3-50nm, such as 4-10nm, preferably around 5nm. Preferably, the thickness of the metal layer on the upper surfaces of the walls is 10-200nm, preferably around 100nm.

The spacing between neighbouring tube shaped elements 140 may be 10-5000nm, such as 100-2000nm, such as 200-1000nm, preferably around 400nm.

As described above, the dimensions and materials of the elements 140 may be tuned to a particular measurement setup and a particular analyte.

In figure 4b, another embodiment is seen where the tube shaped element 141 has no coating on the wall sides. A tip coating 161 is provided, and the layer 18 is provided on the surface 121 of the base 12. Also, no formations are seen in the tube shaped elements.

Again, the cavities 20 are illustrated but may be dispensed with, as a cavity or distance is provided between the layer 18 and the coating/donut 161.

Due to the different geometries obtained with the different metallization manners, different plasmonic modes may be excited. It is expected, for example, that a mode will be seen in the donut 161 provided on the tubes.

In figure 4c, an embodiment is seen resembling that of figure 4a, but where the formations 180 are not seen.

In figure 4d, a fourth embodiment is seen where, in the tubes 142, the formations are not seen but a metal layer extends over the inner side walls and across the bottom of the tube.

Again, in figures 14c/d the cavities 20 are illustrated but may be dispensed with, if the outer layer on the outer walls is brought to end at a position above the upper layer surface.

The substrates of figures 1 and 4 may be used in a number of sensor or testing set-ups, such as a standard SERS set-up where radiation is fed (from above) to the rods 14 or tubes 140 and where scattered radiation is detected also from a position above the SERS substrate. The transparency of the substrate 10 now provides a number of alternative set-ups of which a selection is illustrated in figures 2 and 3.

In figure 2, the base 12 is wedge-shaped in order to facilitate launching a beam there into and the emission of radiation there from. Other manners of facilitating entering and exiting of radiation into/from an element are known. In this set-up, the radiation received interacts with the substance to be analysed and is affected by the dimensions of the substrate 10 and the resulting radiation directed into the base 12 may be collected and detected.

In this manner, also substance positioned at or in the cavities 20 may take part in the determination or measurement in addition to that provided at or between the tips 16.

In figure 3, a transmission set-up is described where, as is often seen, radiation is fed to the substrate from above but where the resulting radiation, such as based on SERS, is determined from below the substrate 10.

A number of different measurement types may be used using the above described set-ups.

LSPR

Using metal nanoarchitectures that are smaller than the wavelength of incident light, a surface plasmon resonance condition is satisfied. This plasmon mode is known as a localized surface plasmon resonance (LSPR). The LSPR enhances local and scattered fields around the particle, exhibiting a distinct color. The LSPR is sensitive to the index of refraction of the surrounding medium, and a change in this causes a change in the color of the particle. Due

to the sensitivity of small changes in refractive index, LSPR sensors are suitable for detection of trace molecules, especially biological molecules.

SPR

Surface plasmon resonance (SPR) utilizes the resonance condition in which incident light excites surface plasmons, usually in metal thin films. SPR is used for detection of trace molecules and especially biochemical experiments due to the sensitivity of the resonance condition to the refractive index of the cladding of the metal film. SPR devices typically use a Kretschmann configuration which requires a prism and a transparent substrate in order to excite an exposed thin film of metal.

LSPR-SPR

If a metal thin film and metal nanoarchitectures (such as the elongate elements) are in close proximity, a coupling can occur between the surface plasmon in the metal thin film and the LSPR modes of the metal nanoarchitectures. This coupling can enhance sensing both via LSPR as well as SPR, as incident light has to simultaneously couple to the resonance of the metal film as well as the nanoarchitectures.

A large number of alternatives to the above substrates may be derived.

The substrate and rods may be fabricated using a maskless reactive ion etch (RIE) process in which a chemically reactive, volatile plasma is generated and accelerated to etch the surface of an element of the desired material, such as fused silica. The chaotic and self-masking nature of the etching process produces an initial non-uniformity on the surface. This non-uniformity is amplified during the process, leading to the creation of stochastically positioned nanostructures extending from a lower lying surface of the element. Thus, the base and the elongate elements are formed.

To obtain the rods of figure 1, the following process parameters may be used:

- Etching time: 7 min
- SF6 flow rate: 170 sccm
- O2 flow rate: 17 sccm

- Platen power: 75 W
- Coil Power: 600 W
- Pressure: 60 mTorr
- Chuck Temperature: 20 °C

To obtain the tube-shaped elements of figure 4, the same process may be used with, e.g. the following process parameters:

- Etching time: 7 min
- SF6 flow rate: 105 sccm
- O2 flow rate: 25 sccm
- Platen power: 110 W
- Coil Power: 600 W
- Pressure: 40 mTorr
- Temperature: 20 °C

Subsequently, a conductive layer, forming the layer and tips/coatings, may be deposited via e-beam physical vapour deposition

The substrate and rods/tubes alternatively may be produced via other methods including Electron beam lithography, Deep UV lithography, Self-assembly nanobead lithography and/or Interference lithography.

The deposition of the layer/tips may alternatively be obtained by electroplating or sputter deposition.

An adhesion modifying layer may optionally be provided between the transparent substrate/rods and the conducting layer. This anti-adhesion layer may be thin and transparent and used in order to maintain the shape of the nanostructures and the

transparency of the device. This layer can be made of a material which changes the manner in which the conducting layer covers the substrate/rods and/or a material which changes the morphology of the tip and/or the cavity. An example of such an adhesion layer is a monolayer of perfluorodecyltrichlorosilane (FDTS) deposited via molecular vapor deposition or a thin film of silicon deposited via plasma enhanced chemical vapor deposition. However this thin adhesion layer can consist of any material deposited via any means.

CLAIMS

1. A substrate comprising a base having a first surface part and a plurality of elongate elements extending away from the substrate and from the first surface part, wherein:

- the base and elongate elements are transparent at at least a first predetermined wavelength, the elongate elements having a height of 40 nm - 5 μm and a width of 5-1500 nm; the elongate elements being positioned with a distance/spacing of 1nm-8μm,

- the elongate elements have a tip of a first material, being an electrically conducting material and/or semiconductor material, the tip having a height of 20-1000 nm and in a direction at least substantially perpendicular to an axis of the pertaining elongate element, a width of 20-1000nm,

- a layer of a second material, being an electrically conducting material and/or semiconductor material, the layer being provided on the first surface part, the layer having an upper plane and a thickness of 5-1000nm, a bottom of the tips being 2-3000 nm above the upper plane;

- a gap or cavity existing between the layer and the elongate elements, the gap being 1-500nm wide.

2. A substrate according to claim 1, wherein the tips, below the bottom thereof, have a layer thickness of the second material of no more than 50 nm.

3. A substrate according to claim 1, where the base and elongate elements are a monolithic element.

4. A substrate according to any of the preceding claims, wherein the base and/or elongate elements is/are made of fused silica.

5. A substrate according to any of the preceding claims, wherein each of the base and elongate elements is/are made of a material transmitting, through a thickness of 0.5mm, at least 20% of radiation in a waveband having a width of at least 100nm and being within 100nm and 1.3μm.

6. A substrate according to any of the preceding claims, where the first and/or second materials is/are selected from the group consisting of: Ag, Au, Pt, Pa, Al, Cu, a group III-V material and/or a semiconductor material.

7. A substrate according to any of the preceding claims, wherein the elongate elements have a width, perpendicular to a longitudinal direction thereof, of 5-500 nm.

8. A substrate according to any of the preceding claims, wherein the elongate elements are positioned with a distance/spacing of 30-300nm.

9. A substrate according to any of the preceding claims, where the gap(s)/cavity(ies) between the layer and one or more elongate element(s) prevent(s) electrical connection between the layer and the tip(s) of the pertaining elongate element(s).

10. A substrate according to any of the preceding claims, wherein the elongate elements are tube-shaped elements.

11. A method of identifying a substance, the method comprising the steps of:

- providing a substrate according to any of the preceding claims,

- providing the substance on the tips and layer of the substrate,

- launching first radiation comprising radiation of a second predetermined wavelength toward the substance,

- detecting second radiation output from the substance at a third predetermined wavelength, the second and/or third wavelength being identical to the first wavelength,

- identifying the substance from the detected second radiation.

12. A method according to claim 11 wherein the first and/or the second radiation travels, during the launching step, through at least one gap/cavity.

13. A method according to claim 11 or 12 wherein, during the launching step, at least part of the first radiation is launched toward the substance through the base.

14. A method according to any of claims 11-13 wherein, during the detecting step, at least part of the second radiation travels through the base before detection.

ABSTRACT

A substrate for a plurality of different measurement set-ups such as SERS, SPR and LSPR which substrate has a base and a plurality of elongate elements with metallic tips. A metallic layer is present on the base surface between the elongate elements and gaps or cavities exist between the layer and the elongate elements. When the elongate elements and the base are transparent, transmission measurement set-ups are also possible.

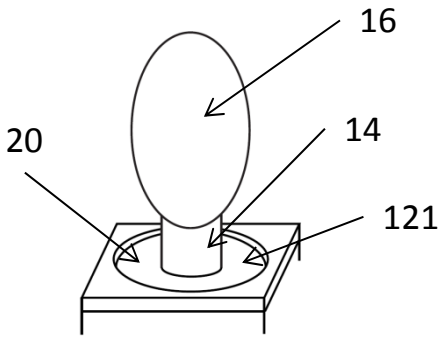

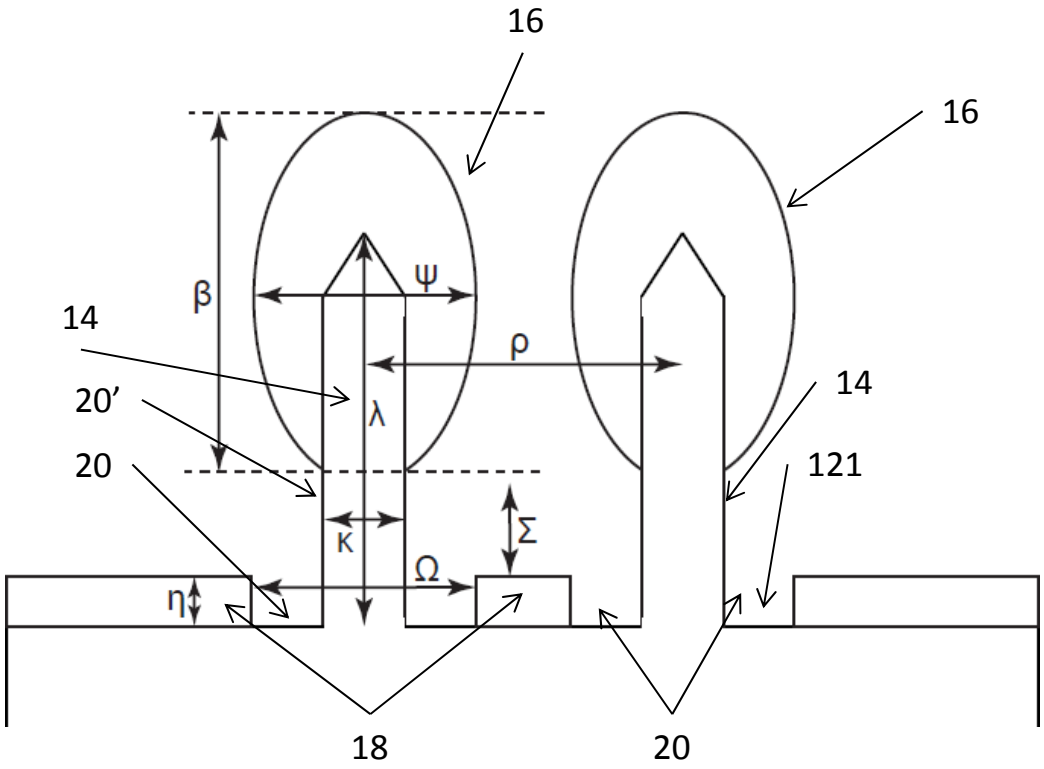

Figure 1

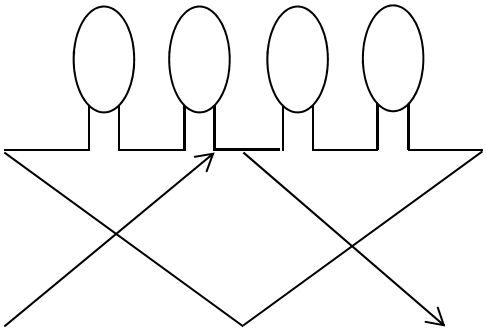

Figure 2

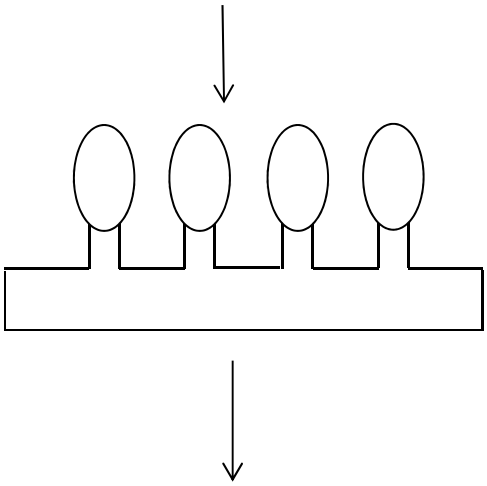

Figure 3

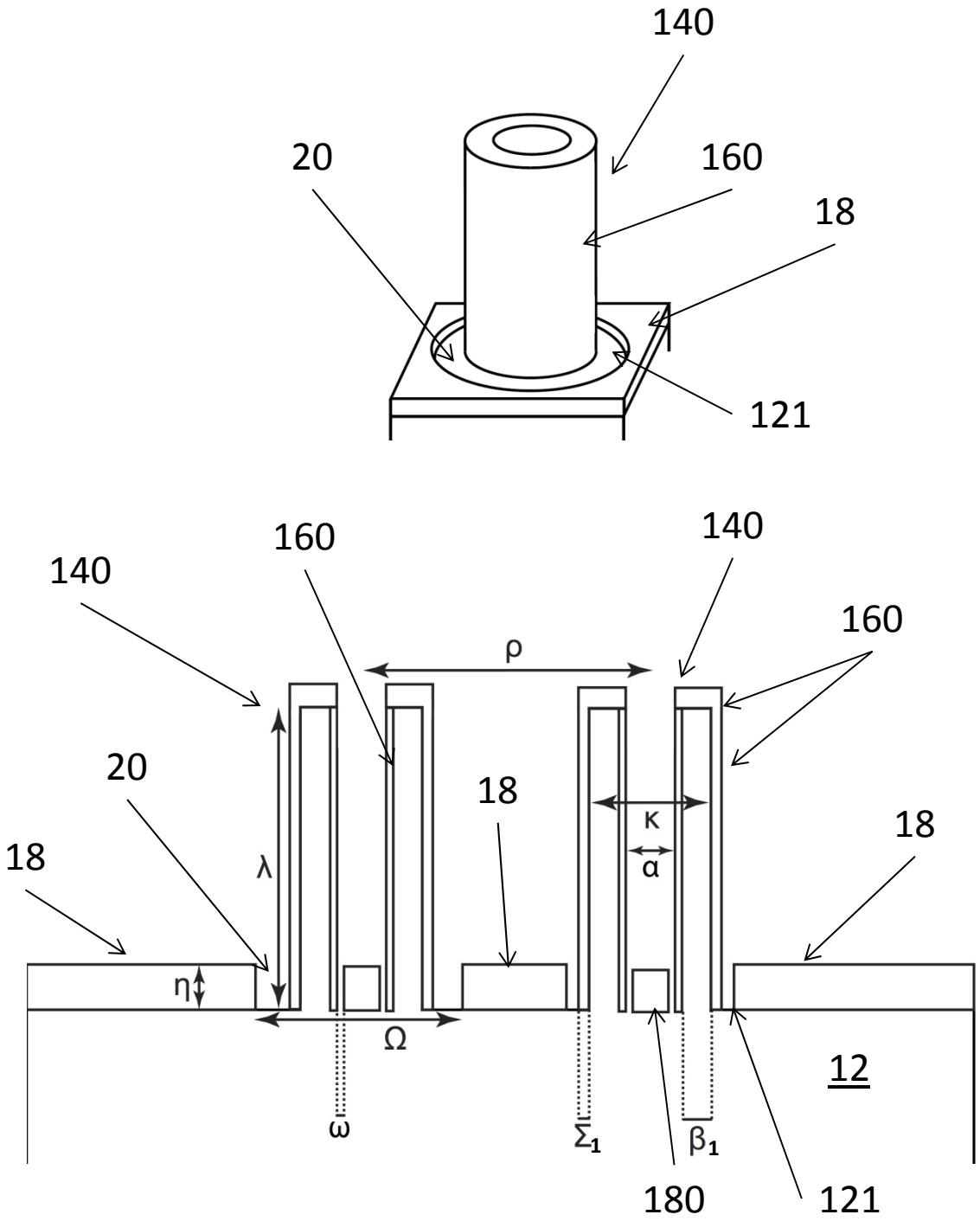
140
20
160
18
121
160
140
140
160
ρ
20
18
κ
18
18
λ
α
η
Ω
12
ω
Σ1
β1
180
121

Figure 4a

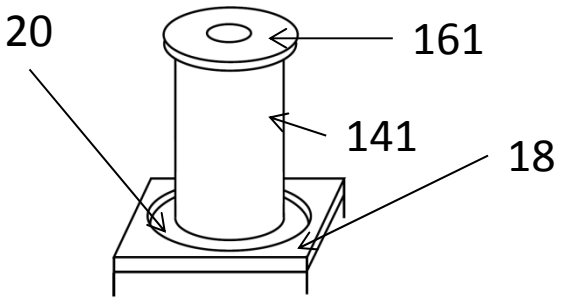

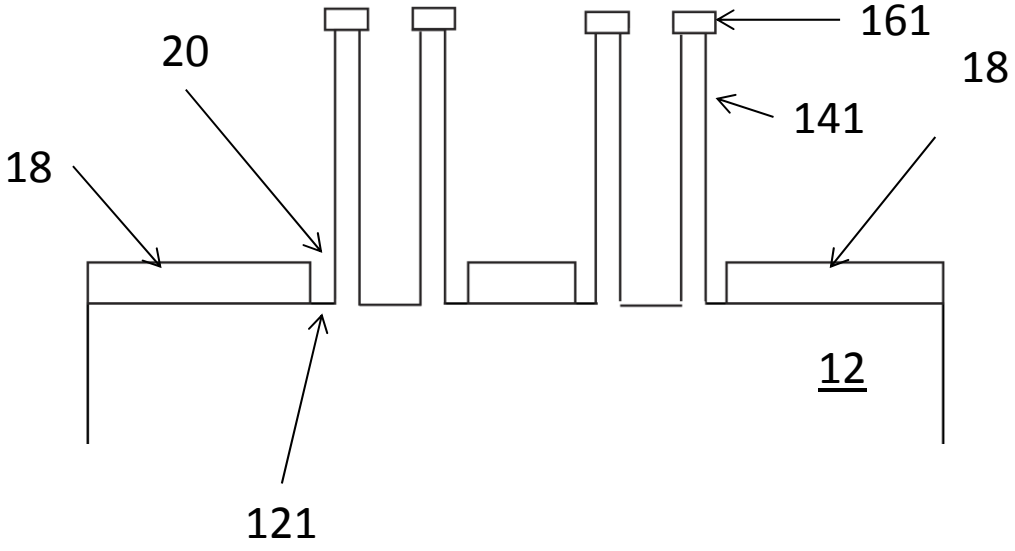

Figure 4b

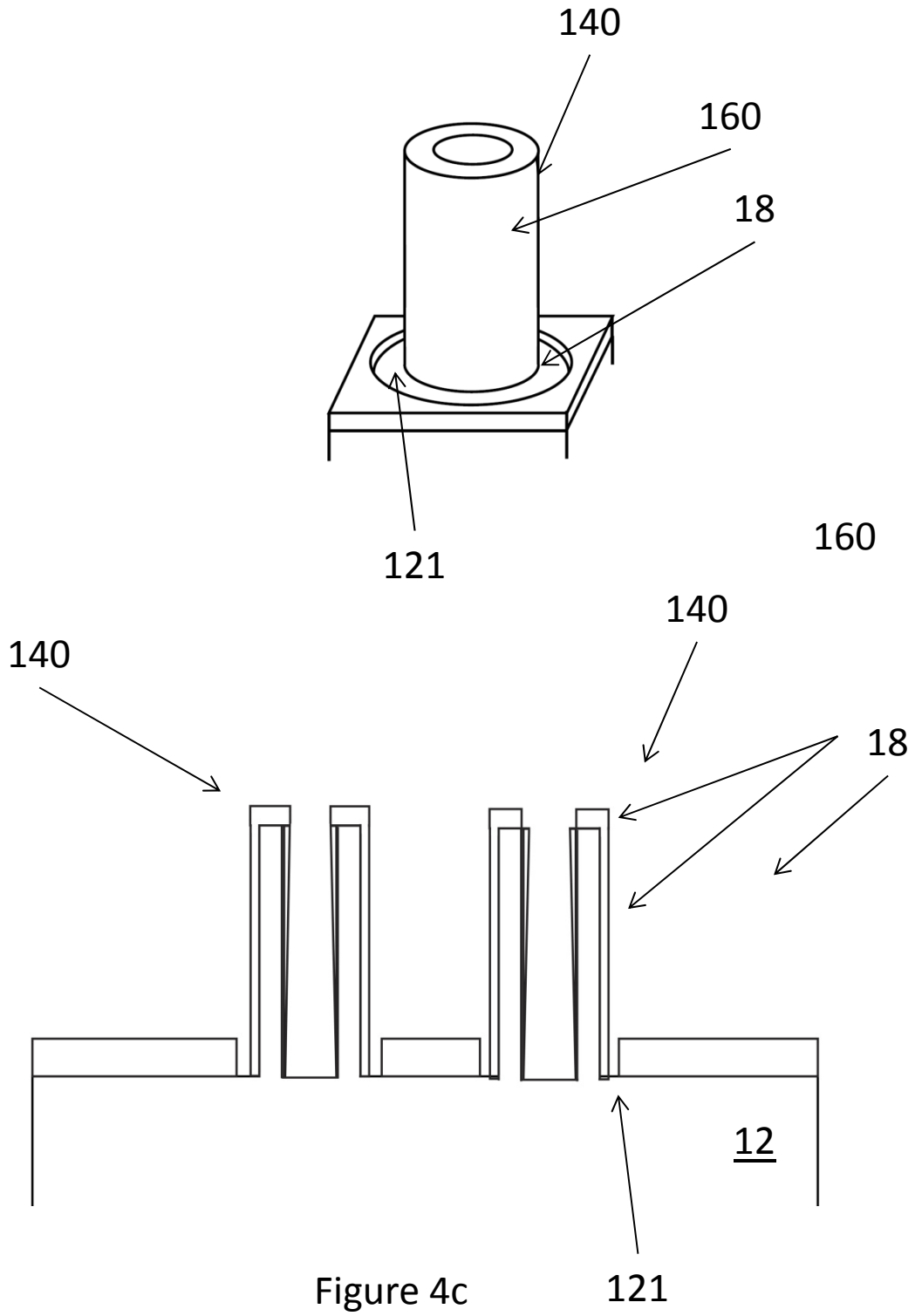

Figure 4c

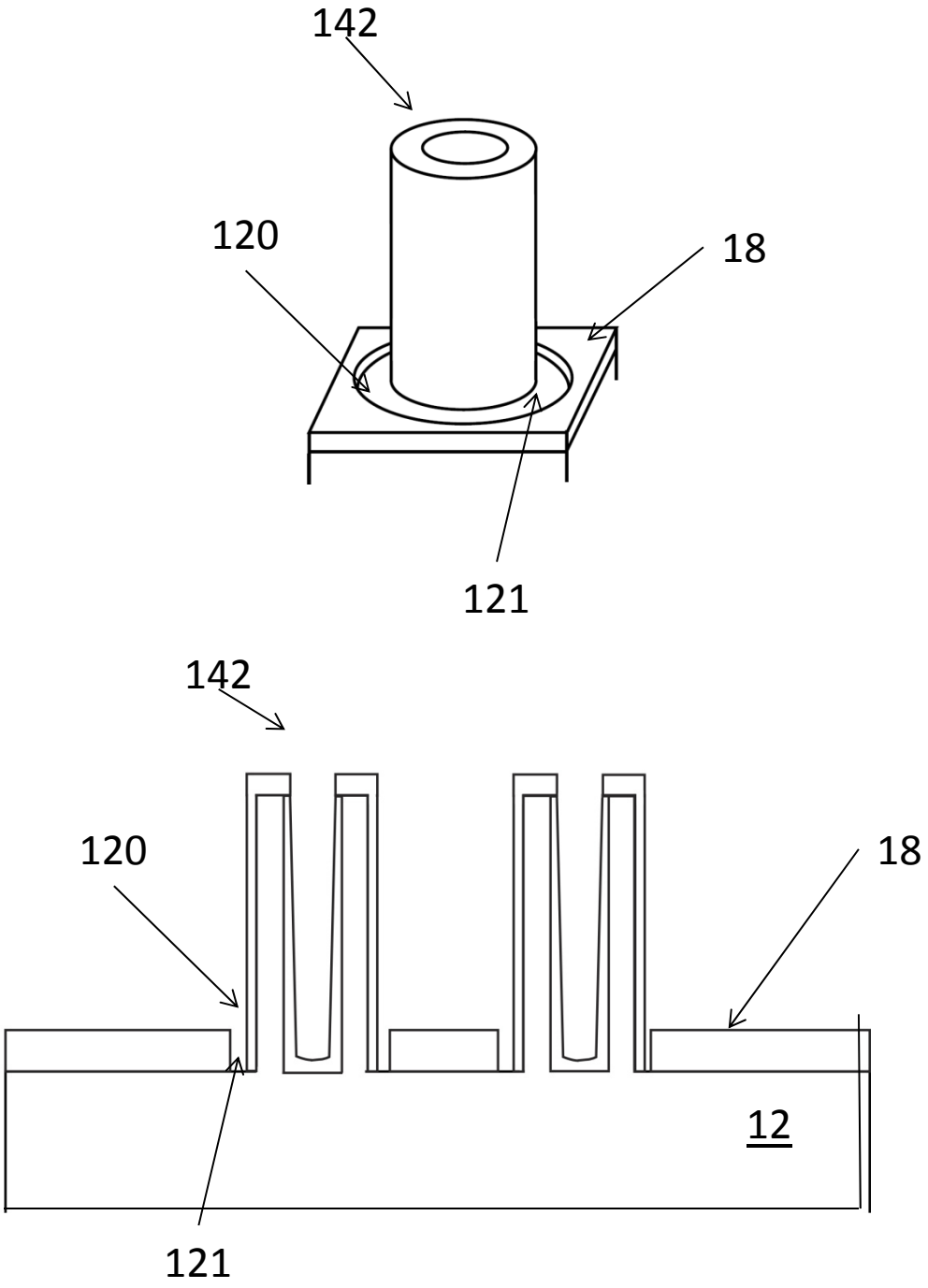

Figure 4d

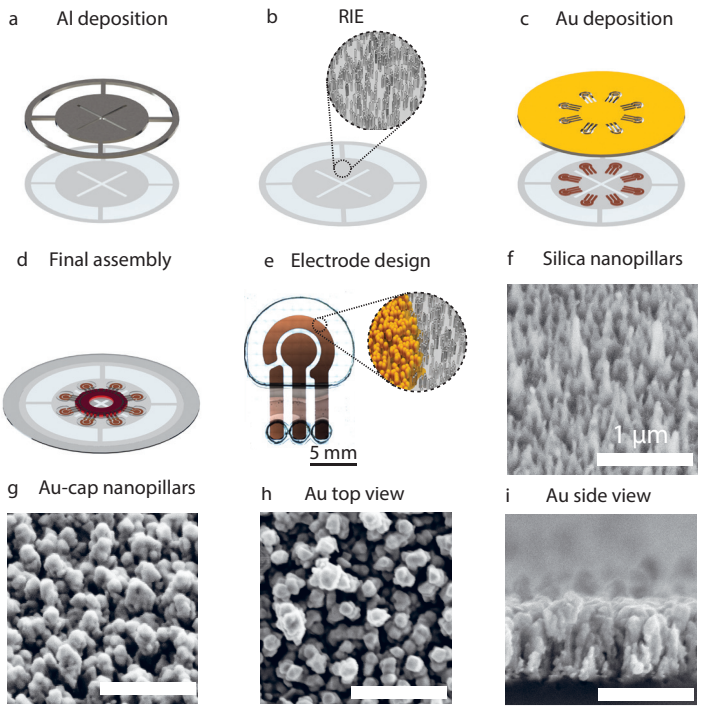

Published by:
DTU Nanotech
Department of Micro- and Nanotechnology
Technical University of Denmark
Ørsteds Plads, building 345C
DK-2800 Kgs. Lyngby